2008

Applications of effective field theories within and beyond the Standard Model

Oleg Antipin
Iowa State University

Applications of effective field theories within and beyond the Standard Model

by

Oleg Antipin

A dissertation submitted to the graduate faculty

in partial fulfillment of the requirements for the degree of

DOCTOR OF PHILOSOPHY

Major: High Energy Physics

Program of Study Committee:
German Valencia, Major Professor
Soeren Prell
Kerry Whisnant
James Vary
Domenico D'Alessandro

Iowa State University

Ames, Iowa

2008

TABLE OF CONTENTS

LIST OF TABLES iv

LIST OF FIGURES v

ACKNOWLEDGMENT ix

CHAPTER 1. Introduction 1

1.1 Standard Model 1

1.2 Effective field theories 3

1.2.1 Examples of effective field theories 4

CHAPTER 2. Theoretical tools 7

2.1 Chiral perturbation theory 7

2.2 Heavy quark effective theory 9

2.2.1 Heavy Quark Symmetries 11

2.3 Randall-Sundrum model 12

CHAPTER 3. Decay $\Omega^- \to \Xi^-\pi^+\pi^-$ in heavy-baryon chiral perturbation theory 16

3.1 Introduction 16

3.2 Leading-order calculation 17

3.3 Calculation to next-to-leading order 21

3.4 Conclusions 24

CHAPTER 4. B-physics 29

4.1 Radiative B decays 30

4.1.1 Introduction 30

4.1.2 $\mathbf{b \to X_c \gamma}$ and $\mathbf{b \to X_c \gamma\gamma}$ . . . 30
4.1.3 Exclusive Modes and HQET . . . 33
4.1.4 $\mathbf{B \to D^\star \gamma}$ . . . 41
4.1.5 $\mathbf{B \to D \gamma\gamma}$ and HQET . . . 46
4.1.6 Summary and Conclusions . . . 56
4.2 The role of $\mathbf{D^{**}}$ in $\mathbf{B \to D_S K \pi}$ decay . . . 57
4.2.1 Introduction . . . 57
4.2.2 Formalism . . . 59
4.2.3 $\mathbf{B^- \to D_s^+ K^- \pi^-}$ and the $\mathbf{D^{\star\star}}$ resonances . . . 62
4.2.4 Discussion . . . 67
4.2.5 $\mathbf{B^- \to D^0_{0,2} \pi^- \to D^{0*} \gamma \pi^-}$ . . . 71
4.2.6 Conclusions . . . 72
CHAPTER 5. Search for gravitons in RS model . . . 74
5.1 Introduction . . . 74
5.2 Model . . . 77
5.2.1 Low energy constraints on model parameters . . . 77
5.2.2 Couplings of KK gravitons . . . 78
5.3 Production and decay of KK gravitons . . . 79
5.4 Battling SM background . . . 80
5.4.1 Pure leptonic mode: $e^\pm \mu^\mp$ final state . . . 80
5.4.2 Semileptonic mode . . . 81
5.5 Acceptance cuts and results . . . 81
5.5.1 Pure leptonic mode: $e^\pm \mu^\mp$ final state . . . 82
5.5.2 Semileptonic decay . . . 84
5.6 Discussion . . . 89
5.7 Conclusion . . . 91
BIBLIOGRAPHY . . . 92

LIST OF TABLES

Table 4.1 Partial branching ratios for spin amplitudes. 69

Table 5.1 Couplings of the nth level KK graviton to the SM fields. t_R assumed to be localized on the TeV brane. Parameter m_1^G is the mass of n=1 graviton and $x_1^G = 3.83$ is the first root of the first order Bessel function. $N_c = 3$ is number of QCD colors. 79

Table 5.2 Purely leptonic mode cross-sections [in fb] and S/B ratios after basic and dilepton mass cuts in Eq.5.5 and Eq.5.6 were imposed. Poisson statistics CL is appropriate description if the number of background events < 10. 84

Table 5.3 Semileptonic mode signal cross-sections [in fb] and S/B ratios along with W + 1 jet and WW SM backgrounds. Signal 1 and the corresponding W + 1 jet background results were obtained after cuts in Eqs.5.7,5.8 were imposed and $m_G \pm \Gamma_G/2$ integration region was chosen. Signal 2 and corresponding WW background results were obtained after $|\eta_W| < 1$ cut and integrated in $m_G \pm \Gamma_G$ window. 87

Table 5.4 Average lepton energies in the lab frame from the decay of polarized W^- bosons. For a W^+ decay, the results for the left-handed and right-handed rows need to be switched. 91

LIST OF FIGURES

Figure 3.1 Diagrams contributing to $\Omega^- \to \Xi^-\pi^+\pi^-$. Each solid blob represents an effective weak vertices which are defined in Fig.3.2 and strong vertices follow from $\mathcal{L}_{\rm s}$ in Eq. (3.4). 19

Figure 3.2 Contributions to the effective weak vertices up to NLO in HBχPT contributing to $\Omega^- \to \Xi^-\pi^+\pi^-$. Weak vertices (denoted by x) follow at LO from $\mathcal{L}_{\rm w}$ in Eq. (3.5) and at NLO from $\mathcal{L}'_{\rm w}$ in Eq. (3.11b). Correspondindly, strong vertices follow from $\mathcal{L}_{\rm s}$ in Eq. (3.4) or $\mathcal{L}'_{\rm s}$ in Eq. (3.11a). 20

Figure 3.3 (a) Distribution of $\Xi^-\pi^+$ invariant-mass in $\Omega^- \to \Xi^-\pi^+\pi^-$ at leading order with parameter values in Eqs. (3.7)-(3.8), and (b) its branching ratio as function of $|\mathcal{C}h_C|$ with $D-F$ and $\mathcal{H}$ values in Eqs. (3.7) and (3.8). 26

Figure 3.4 Distributions of $\Xi^-\pi^+$ invariant-mass in $\Omega^- \to \Xi^-\pi^+\pi^-$ obtained from our leading-order amplitude (solid curve) and from the assumption of uniform-phase-space decay distribution (dashed curve), both normalized to yield $\mathcal{B}(\Omega^- \to \Xi^-\pi^+\pi^-) = 3.6 \times 10^{-4}$ 27

Figure 3.5 (a) Branching ratios for $\Omega^- \to \Xi^-\pi^+\pi^-$ and (b,c) the corresponding distributions of $\Xi^-\pi^+$ invariant-mass. The black (dark gray) band comes from the LO amplitude only (the LO amplitude and the γ_8 terms in the NLO amplitude), and the light-gray band results from the LO and NLO amplitudes we consider, as described in the text. The dotted lines in (a) bound the range implied by the preliminary HyperCP data. The dashed curves in (b) and (c) have been reproduced from Fig. 3.4. 28

Figure 4.1 Photon energy spectrum in $b \to X_c\gamma$ with $\theta_{min} = 5°$. 31

Figure 4.2 $M^2_{\gamma\gamma}$ distribution for the process $b \to X_c\gamma\gamma$ with the cuts described in the text. 32

Figure 4.3 Pole diagrams responsible for $B \to D^\star\gamma$ at leading order in heavy quark and chiral theories. 42

Figure 4.4 Non-leading contributions to $B \to D^\star\gamma$: a)$P^* - P$ weak transitions that vanish in the $m_B = m_D$ limit; b-d) additional pole contributions from positive parity states. 44

Figure 4.5 Pole diagrams responsible for $B \to D^\star\gamma\gamma$ at leading order in heavy quark and chiral theories. 48

Figure 4.6 $\Gamma(B^0 \to \bar{D}^0\gamma\gamma)$ as a function of r_μ. We use the RQM magnetic moment for the B and we normalize the rate to its value when $r_\mu \sim 2.87$, the value of μ_D in the RQM. 49

Figure 4.7 Additional diagrams involving particles from the $(0^+, 1^+)$ and $(1^+, 2^+)$ doublets. H(S) stands for either of the H(S)-multiplet members 50

Figure 4.8 Additional diagrams involving particles from the $(0^+, 1^+)$ and$(1^+, 2^+)$ doublets. S stands for either of the S-multiplet members 51

Figure 4.9 Normalized differential decay rate for $B^0 \to \bar{D}^0\gamma\gamma$ as a function of the photon pair invariant mass. 53

Figure 4.10 Density plot for the double differential decay rate for $B^0 \to \bar{D}^0\gamma\gamma$ as a function of the two photon energies. 54

Figure 4.11 Normalized differential decay rate for $B^0 \to \bar{D}^0\gamma\gamma$ as a function of $\omega = v \cdot v'$. 55

Figure 4.12 The $D_s^+K^-$ invariant mass spectra for the $B^- \to D_s^+K^-\pi^-$. The histogram shows the non-resonant signal Monte Carlo events distribution, scaled to the number of events in the data signal region [56]. 57

Figure 4.13 Decomposition of the decay mode $B^- \to D_s^+ K^- \pi^-$ into contributions that are mediated by a $D^{\star\star}$ that is near its mass shell and those that are not. 59

Figure 4.14 Diagrams contributing to $B^- \to D_s^+ K^- \pi^-$. For diagrams of the form (a), the strange B intermediate states go with a pion emission from the weak vertex (denoted by an x). 63

Figure 4.15 $M_{D_s^+ K^-}$ invariant mass distribution for $B_1 = 1$, $B_2 = 1.13$ for: a) diagrams involving a D_0^0 (solid line); b) diagrams involving a D_2^0 (dashed line) and c) all other diagrams: for $h' > 0$ (dotted line) and for $h' < 0$ (dash-dotted). Interference terms between (a), (b), and (c) are not shown. 65

Figure 4.16 $M_{D_s^+ K^-}$ invariant mass distributions with $B_1 = 1$, $B_2 = 1.13$ (solid), $B_1 = 1.15$, $B_2 = 1.06$ (dotted), $B_1 = 1.308$, $B_2 = 1$ (dashed) for (a) $h' < 0$ and (b) $h' > 0$. 67

Figure 4.17 Contributions to the decay rate from different spin amplitudes for $B_1 = 1$, $B_2 = 1.13$ with: (a) $h' < 0$, (b) $h' > 0$. In both cases the solid line corresponds to M_0, the dotted line to M_1 and the dashed line to M_2. Higher spin contributions are negligible and are not shown. 69

Figure 4.18 Scalar component of $\Gamma(B^- \to D_s^+ K^- \pi^-)$ for three different values of $m_{D_0^0}$ corresponding to the central value in Eq. 4.65 (solid), and to the one standard deviation values (dashed, dotted), with $h' > 0$. 70

Figure 4.19 Normalized $\Gamma(B^- \to D_s^+ K^- \pi^-)$ as a function of B_1 factor for: a) full kinematic range; and b) scalar contribution in the $M_{D_s^+ K^-} \leq m_{D_0^0} + 2\Gamma_{D_0^0} \sim 2.8$ GeV range. The horizontal lines in (a) show the 1-σ range from the BaBar measurement [56]. In both cases the solid line corresponds to $h' > 0$ and the dashed line to $h' < 0$. 71

Figure 5.1 (a) Total signal cross-section for $pp \to l\nu l'\bar{\nu}_{l'}$, and (b) corresponding number of events for 300 fb^{-1}. Basic cuts from Eq.5.5 are applied and c=1. Corresponding SM background is $\approx$ 24 fb and is independent of the graviton mass. 82

Figure 5.2 (Color online) Dilepton invariant mass distributions for graviton masses of 2 TeV (dashed red) and 3 TeV (solid blue). Dotted curve corresponds to the SM background. 83

Figure 5.3 The total signal (solid) and SM background W + 1 jet (dotted) cross-section (integrated in $m_G \pm \Gamma_G/2$ window) after cuts specified in Eq.5.7 were applied. 85

Figure 5.4 Differential lepton energy distribution for the signal (solid) and SM W + 1 jet background (dotted) (integrated in $m_G \pm \Gamma_G/2$ window) after cuts specified in Eq.5.7 were applied for (a) m_G=2 TeV and (b) m_G=3.5 TeV. 86

Figure 5.5 (Color online) (a) The total signal (solid) and SM background (dashed) cross-section (integrated in $m_G \pm \Gamma_G$ window) for $pp \to W(l\nu)W(jj)$ after $|\eta_W| < 1$ cuts were applied for c=1 (red) and c=2 (blue) values, (b) Corresponding number of events for 300 fb^{-1}. 88

Figure 5.6 Contributions of the 2 TeV gauge boson and 3 TeV graviton to the $pp \to W(l\nu)W(jj)$ process. Cuts specified in Eq.5.7 were applied and c=1. 89

ACKNOWLEDGMENT

First of all, I would like to thank my advisor German Valencia for inspiring me to do research in the particle physics. His two excellent courses, continious support and encouragement gave me enormous boost at the beginning of my research. I am grateful to my committee members for their careful reading of this thesis and their important comments and attention to my work. I would also like to thank my collaborators Amarjit Soni, Jusak Tandean, Piyabut Burikham, members of high energy group at Iowa State University, especially Jim Cochran, for many interesting discussions.

Special thanks go to all my friends and fellow graduate students, in particular Sergey Gratiy, Alex Tchernatinsky, Sergey Chekmenev, and Jun Li for their help and friendship.

This thesis would not be possible without very special people in my life: my wife Dina, my sister Viola, and my parents. I thank them for their support, encouragement, and love.

Last, but not least, I thank Jerry Pierce for careful reading of this work and many stimulating discussions.

CHAPTER 1. Introduction

This chapter explains the role of the effective field theories in modern physics, especially modern elementary particle physics. We start with a brief introduction to the Standard Model (SM) which is currently the accepted theory of particle physics and, thus far, in superb agreement with experiment. However, we will see that the SM cannot be the fundamental theory of nature and can be viewed only as an Effective Field Theory (EFT) of nature. Examples of the other EFTs later in the chapter will explain how we arrived at the SM, tested its various predictions, and how they may help to find the physics beyond it.

1.1 Standard Model

The Standard Model of particle physics is a theory that describes three of the four known fundamental interactions between the elementary particles that make up all matter. The two components of the standard model are the electroweak theory, which describes the interactions via the electromagnetic and weak forces, and quantum chromodynamics, the theory of the strong nuclear force. Both theories are gauge field theories, which describe the interactions between particles in terms of the exchange of a "messenger" particles that have one unit of intrinsic angular momentum, or spin. The standard model has proved to be a highly successful framework for predicting the interactions of quarks and leptons with great accuracy. Yet, it has a number of weaknesses that leads to a search for a more complete theory of subatomic particles and their interactions. For example, it cannot explain why there are three generations of quarks and leptons; and it makes no predictions of the masses of the quarks and the leptons, nor of the strengths of the various interactions.

All of the particles present in the standard model fall into one of the three groups: matter

particles, force-mediating particles, and the Higgs boson. The matter particles described by the standard model all have an intrinsic property known as "spin," whose value is determined to be 1/2, which means that they are fermions. As a result, they follow the Pauli exclusion principle (in agreement with the spin-statistics theorem), which determines their "material" quality. A total of twelve different types of matter particles are known and accounted for by the standard model. Six of these are classified as quarks (up, down, charm, strange, top, and bottom); and the other six are classified as leptons (electron, muon, tau, and their corresponding neutrinos). In addition, every particle has its antiparticle partner, which has the same mass and opposite charge; and we specify these charges now.

Each quark can carry any one of three color charges - red, green, or blue, enabling them to participate in the strong interactions. The up-type quarks (up, charm, and top quarks) carry an electric charge of +2/3; and the down-type quarks (down, strange, and bottom) carry an electric charge of -1/3, enabling both types to participate in electromagnetic interactions. Leptons do not carry any color charge. They are color neutral; and, thus, they do not feel strong force. The electron-type leptons (the electron, the muon, and the tau lepton) carry an electric charge of -1, enabling them to participate in electromagnetic interactions. The neutrino-type leptons (the electron neutrino, the muon neutrino, and the tau neutrino) carry no electric charge, which prevents them from participating in electromagnetic interactions. Both quarks and leptons carry flavor charges, including the weak isospin, enabling all particles to interact via the weak nuclear interaction.

In contrast to matter particles, the known force-mediating particles of the Standard Model have the spin of 1; i.e., all these particles are bosons. For this reason, they do not follow the Pauli Exclusion Principle. There are three types of the force-mediating particles. First, we have a photon which mediates the electromagnetic force between electrically charged particles. The photon is massless and is well-described by the theory of quantum electrodynamics. Second, we have the W^+, W^-, and Z gauge bosons which mediate the weak interactions between particles of different flavors (all quarks and leptons). They are heavy, with the Z and $W^\pm$ having mass of about 91.2 GeV and 80.4 GeV respectively. The weak interactions involving the $W^\pm$ act on

the left-handed particles and the right-handed antiparticles exclusively. Moreover, as the $W^{\pm}$ carry an electric charge of ± 1, they couple to the electromagnetic interactions. The electrically neutral Z boson interacts with both left-handed particles and antiparticles. These three gauge bosons are grouped together and collectively mediate the electroweak interactions. Third, we have the eight gluons which mediate the strong interactions between the color charged particles (the quarks). Gluons are massless. The eightfold multiplicity of gluons is labeled by a combination of a color and an anticolor charge, which means, for example, that quarks may exchange a green-anti-blue gluon. The gluon has an effective color charge, and, thus, they can interact among themselves. The gluons and their interactions (with quarks and themselves) are described by the theory of quantum chromodynamics (QCD).

The Higgs particle is, as yet, a hypothetical particle invoked to explain why the carriers of the electroweak force (the W and Z bosons) have mass. If this particle exist at all, it requires an exceptionally large amount of energy to create and to observe it under laboratory circumstances. It has no intrinsic spin; and thus, like the force-mediating particles which also have integral spin, is also classified as a boson. The Higgs Boson plays a unique role in the Standard Model and a key role in explaining the origins of the mass of other elementary particles, in particular, the difference between the massless photon and the very heavy W and Z bosons. In the electroweak theory, it generates the masses of the massive leptons (electron, muon, and tau) and also of the quarks. As of 2007, no experiment has directly detected the existence of the Higgs boson, but there is some indirect evidence for it. It is hoped that, upon the completion of the Large Hadron Collider (LHC) at CERN, experiments conducted there would bring experimental evidence confirming the existence of this particle.

1.2 Effective field theories

The basic premise of the effective field theories is that the dynamics at low energies (or large distances) does not depend on the details of the dynamics at high energies (or short distances). As a result, low energy physics can be described using an effective Lagrangian that contains only a few degrees of freedom, ignoring additional degrees of freedom present at

higher energies.

Very often, the process of integrating out irrelevant degrees of freedom is performed using the renormalization group (RG) equations. Although this method does not always guarantee the actual construction of effective field theories, the physical understanding of their structure becomes more transparent through an RG analysis. To be more specific, imagine that in the fundamental theory, there is a single mass scale M. Then, the effective field theory can be constructed as an expansion in 1/M. This expansion would be useful if the maximum momentum scale k of the scattering or other processes under consideration would satisfy the condition $k/M \ll 1$. Since effective field theories are not valid at small length scales, they need not be renormalizable.

1.2.1 Examples of effective field theories

- Fermi theory of beta decay

  The most well-known example of an effective field theory is the Fermi theory of beta decay. This theory was developed during the early study of weak decays of nuclei when only the hadrons and leptons undergoing weak decay were known. The typical reactions studied were:

$$n \rightarrow p + e^- + \overline{\nu}_e \tag{1.1}$$

$$\mu^- \rightarrow e^- + \overline{\nu}_e + \nu_\mu \tag{1.2}$$

  This theory postulated a pointlike interaction between the four fermions involved in these reactions. The theory had great phenomenological success and was eventually understood to arise from the gauge theory of electroweak interactions, which forms a part of the standard model of particle physics. In this more fundamental theory, the interactions are mediated by a flavour-changing gauge boson, the W, described above. The enormous success of the Fermi theory has its roots in the fact that the W particle has mass of about 80 GeV, whereas the early experiments were all done at an energy scale of less than 10 MeV. It is this separation of scales that allowed Fermi to get by without the W bosons in the theory and to think of the interaction as pointlike.

- BCS theory of superconductivity

  This is a theory of superconductivity developed by Bardeen, Cooper, and Schrieffer in 1957. Under certain conditions, attractions between two electrons due to a succession of phonon exchanges can exceed slightly their Coulomb repulsion. The electrons of opposite spin will then be weakly bound together, forming a so-called Cooper electron pair. The length scale of these pairs is much larger than the wavelength of phonons. As a result, it is possible to neglect the dynamics of phonons and construct a theory in which two electrons interact at a point.

- In elementary particle physics, the effective field theory of QCD called chiral perturbation theory has had success. This theory deals with the interactions of hadrons with pions or kaons, which are the Goldstone bosons of spontaneous chiral symmetry breaking. The expansion parameter is the pion energy/momentum. In the next chapter, this EFT will be discussed in greater details.

- If a hadron contains one heavy quark (such as the bottom or charm), starting from QCD Lagrangian, we may construct an effective field theory by performing a $1/m_Q$ expansion. This is the essence of the Heavy-Quark Effective Theory (HQET), and in the next chapter we will present its field-theoretic realization.

- Heavy baryon chiral perturbation theory is an effective quantum field theory used to describe the interactions of pions and baryons. It is an extension of the chiral perturbation theory which just describes the low-energy interactions of pions. As the baryons are much heavier than the pions, heavy baryon chiral perturbation theory uses a nonrelativistic description of baryons compared to that of the pions. Higher order terms in the heavy baryon Lagrangian come at higher orders of $1/m_B$ where m_B is the baryon mass. In this thesis, all baryons and all hadrons containing bottom and/or charm quarks will be treated as heavy.

- For hadrons containing two heavy quarks, an effective field theory which expands in powers of the relative velocity of the heavy quarks, called non-relativistic QCD (NRQCD),

has been found useful, especially when used in conjunctions with lattice QCD.

- For hadron reactions with light energetic (collinear) particles, the interactions with low-energetic (soft) degrees of freedom are described by the soft-collinear effective theory (SCET).

- General relativity is expected to be the low energy effective theory of a full theory of quantum gravity, such as string theory. The expansion scale is the Planck mass. One of the EFT of gravity popular in literature called the Randall-Sundrum model will be discussed in the next chapter.

- All of the condensed matter physics consists of writing effective field theories for the particular property of matter being studied.

- Finally, as discussed above, the standard model of particle interactions can be only low energy EFT.

  With the upcoming start of the CERN LHC, our quest for the physics beyond the SM is likely to give a signal. In our search for the fundamental theory of nature, the effective field theories were proven to be a valuable tool (as in the case of the Fermi theory). In the remaining chapters of this dissertation, we will see concrete applications of the EFT to particle physics; and the next chapter describes the needed theoretical background.

CHAPTER 2. Theoretical tools

This chapter provides field-theoretical description of the effective field theories used later in this thesis. Due to the enormous amount of literature, this brief review cannot give a complete survey, nor a proper historical introduction. My main effort is to point out their effective field theories' nature, and I apologize for any developments left out of the scope of this thesis.

2.1 Chiral perturbation theory

We start with the QCD Lagrangian, which has the form:

$$\begin{aligned}
\mathcal{L}_{QCD} &= \mathcal{L}_g + \mathcal{L}_q + \mathcal{L}_m \\
\mathcal{L}_g &= -\frac{1}{4g^2}\mathrm{Tr}\,(G_{\mu\nu}G^{\mu\nu}) \\
\mathcal{L}_q &= \sum_{f=1}^{N_f} \bar{\psi}_f i D_\mu \gamma^\mu \psi_f \\
\mathcal{L}_m &= \sum_{f=1}^{N_f} m_f \bar{\psi}_f \psi_f \\
D_\mu &= \partial_\mu - igA_\mu \\
G_{\mu\nu} &= [D_\mu, D_\nu],
\end{aligned}$$

where A_μ is the gluon field, ψ_f is the quark field of the f-th flavor ($\psi_f = (u, d, c, s, t, b)$), D_μ is the covariant derivative, $G_{\mu\nu}$ is the field strength tensor, and g is the color charge. The term $\mathcal{L}_g$ describes pure gluon dynamics, the term $\mathcal{L}_q$ corresponds to the quark kinetic energy and quark-gluon interaction, and the term $\mathcal{L}_m$ is responsible for the quark masses. In the massless limit, the QCD Lagrangian ($\mathcal{L}_g + \mathcal{L}_q$) depends on only one dimensionless parameter g. At the same time the strong coupling constant $\alpha_s(\mu)$ becomes scale dependent due to renormalization. The scale parameter of QCD Λ_{QCD} is determined from experiment.

Provided the quarks are massless, the chirality (helicity) of a quark is conserved; and the QCD Lagrangian is symmetric with respect to rotations in the flavor space independently for right- and left-handed quarks. Thus, the massless QCD has the global symmetry described by the group $SU(N_F)_R \times SU(N_F)_L$. While the Lagrangian is chirally symmetric, the ground state of the massless QCD (vacuum) does not have the same property because the chiral symmetry is spontaneously broken. The characteristic feature of this spontaneous symmetry breaking is the emergence of massless, pseudoscalar particles called Goldstone bosons (in the case of two flavors, $N_F = 2$, they correspond to the triplet of pions). The essence of the chiral perturbation theory is to consider the quark mass term $\mathcal{L}_m$ as a perturbation. The mass term explicitly breaks the chiral symmetry, so the Goldstone bosons get nonzero masses; and in the leading order, the pion mass squared is proportional to the quark mass. Chiral perturbation theory (CHPT, χPT) is an effective field theory constructed as an expansion in momenta and masses of physical particles, which are considered to be small on a hadronic scale of about 1 GeV. This approach is extended in baryon chiral perturbation theory, so that the meson interaction with the "heavy" baryons can be treated as well.

The Lagrangian is constructed by introducing every interaction of particles which is not excluded by symmetry, and then ordering them based on the number of momentum and mass powers. It is also common to compress the Lagrangian by replacing the single pion fields in each term with an infinite series of all possible combinations of pion fields. One of the common choices is to incorporate the light pseudoscalar Goldstone bosons into the matrix $U = \exp(\frac{iM}{f_\pi})$ with a normalization in which the pion decay constant is $f_\pi = 132$ MeV. The matrix M is explicitly given by

$$M = \begin{pmatrix} \sqrt{\frac{1}{2}}\pi^0 + \sqrt{\frac{1}{6}}\eta & \pi^+ & K^+ \\ \pi^- & -\sqrt{\frac{1}{2}}\pi^0 + \sqrt{\frac{1}{6}}\eta & K^0 \\ K^- & \bar{K}^0 & -\sqrt{\frac{2}{3}}\eta \end{pmatrix}, \tag{2.1}$$

and we will see an example of the other choice in Chapter 3. A similar matrix can be written for the baryon octet.

After this, the leading order chiral Lagrangian, which describes the interactions among the Goldstone bosons is given by

$$\mathcal{L}_2 = \frac{f^2}{8}\mathrm{tr}(\partial_\mu U \partial^\mu U^\dagger); \tag{2.2}$$

and we will see how to write the interactions of these fields with heavy meson and baryon fields later. But first, we need to have an appropriate formalism to deal with these heavy fields which we discuss in the next section.

2.2 Heavy quark effective theory

HQET is an effective field theory, which may be obtained from QCD by performing a $1/m_Q$ expansion. The leading term corresponds to the infinite mass limit in which the heavy quark acts as a static color source. The momentum p_Q of the heavy quark scales with its mass; and, thus, in order to arrive at the infinite mass limit, it is convenient to use the velocity v of the heavy quark as the basic kinematic quantity. To this end, the heavy quark momentum is split into a large part $m_Q v$ and a residual part k, which is assumed not to scale with the heavy mass. Thus,

$$p_Q = m_Q v + k = m_Q \left(v + \frac{k}{m_Q} \right). \tag{2.3}$$

We shall consider exclusively hadrons containing only a single heavy quark such that, in the infinite mass limit, the velocity v of the heavy quark becomes simply the velocity of the heavy hadron.

In order to write down a field theory which describes the static heavy quark, one needs to go through the usual steps of the construction of an effective field theory, namely to integrate out the heavy degrees of freedom.

In order to do that, we notice that a near on-shell Dirac spinor has two large and two small components. We proceed by defining them as

$$Q(x) = e^{-im_Q v\cdot x}[h_v(x) + H_v(x)], \tag{2.4}$$

where

$$h_v(x) = e^{im_Q v\cdot x}\frac{1+\not{v}}{2}Q(x) \tag{2.5}$$

are the large components, and

$$H_v(x) = e^{im_Q v\cdot x}\frac{1-\not{v}}{2}Q(x) \tag{2.6}$$

are the small components.

Inserting these definitions into the Dirac Lagrangian and solving the classical equation of motion for the field H_v yields

$$H_v(x) = \frac{1}{2m_Q + iv\cdot D} i\not{D}_\perp h_v(x), \tag{2.7}$$

where $iD_\perp^\mu = iD^\mu - v^\mu iv\cdot D$.

In this way, one obtains

$$\begin{aligned} Q(x) &= e^{-im_Q v\cdot x}\left[1+\left(\frac{1}{2m+iv\cdot D}\right)i\not{D}_\perp\right]h_v(x) \qquad (2.8)\\ &= e^{-im_Q v\cdot x}\left[1+\frac{1}{2m_Q}\not{D}_\perp+\left(\frac{1}{2m_Q}\right)^2(-iv\cdot D)\not{D}_\perp+\cdots\right]h_v(x)\\ \mathcal{L} &= \bar{h}_v(iv\cdot D)h_v + \bar{h}_v i\not{D}_\perp\left(\frac{1}{2m+iv\cdot D}\right)i\not{D}_\perp h_v \qquad (2.9)\\ &= \bar{h}_v(iv\cdot D)h_v + \frac{1}{2m}\bar{h}_v(i\not{D}_\perp)^2 i h_v + \left(\frac{1}{2m}\right)^2\bar{h}_v(i\not{D}_\perp)(-iv\cdot D)(i\not{D}_\perp)h_v+\cdots, \end{aligned}$$

where D is the covariant derivative of QCD, $Q(x)$ is the heavy quark field in full QCD, and h_v is the static heavy quark moving with the velocity v. Note that h_v corresponds to the upper components of the full field since

$$P_+ h_v = h_v, \quad P_- h_v = 0, \quad P_\pm = \frac{1}{2}(\not{v}\pm 1). \tag{2.10}$$

The leading terms of these expansions define the static limit; the static Lagrangian

$$\mathcal{L}_{stat} = \bar{h}_v(ivD)h_v \tag{2.11}$$

is a dimension-four operator and defines, in combination with the usual Lagrangian for the light degrees of freedom, a renormalizable field theory.

2.2.1 Heavy Quark Symmetries

In the case in which the bottom quark and the charm quark are assumed to be heavy, one would write a static Lagrangian for both quarks

$$\mathcal{L}_{stat} = \bar{b}_v(v \cdot D)b_v + \bar{c}_{v'}(v \cdot D)c_{v'}, \tag{2.12}$$

where b_v ($c_{v'}$) is the field operator for the b (c) quark moving with velocity v (v'). In particular, the masses of the heavy quarks do not appear in the Lagrangian (2.12); and, as a consequence, (2.12) in the case $v = v'$ exhibits an $SU(2)$ Heavy Flavor Symmetry, which rotates the b_v field into the c_v field.

The static heavy quark field h_v is still a two-component object corresponding to the upper component of the full heavy quark field Q. However, since both spin directions couple in the same way to the gluons, we may rewrite the leading-order Lagrangian as

$$\mathcal{L} = \bar{h}_v^{+s}(ivD)h_v^{+s} + \bar{h}_v^{-s}(ivD)h_v^{-s}, \tag{2.13}$$

where $h_v^{\pm s}$ are the projections of the heavy quark field on a definite spin direction s

$$h_v^{\pm s} = \frac{1}{2}(1 \pm \gamma_5 \not{s})h_v, \quad s \cdot v = 0. \tag{2.14}$$

This Lagrangian has a symmetry under the rotations of the heavy quark spin; and, hence, all the heavy hadron states moving with the velocity v fall into spin-symmetry doublets as $m_Q \to \infty$. The simplest spin-symmetry doublet in the mesonic case consists of the pseudoscalar meson $H(v)$ and the corresponding vector meson $H^*(v, \epsilon)$, since a 90°-spin rotation $R(\epsilon)$ around the rotation axis ϵ ($v\epsilon = 0$) yields

$$R(\epsilon)|H(v)\rangle = (-i)|H^*(v, \epsilon)\rangle. \tag{2.15}$$

In the heavy-mass limit, the spin symmetry partners have to be degenerate; and their splitting has to scale as $1/m_Q$. Also, the symmetries imply relations between the matrix elements involving the heavy quarks. For a transition between heavy ground-state mesons H (either pseudoscalar or vector) with heavy flavor f (f') moving with velocities v (v'), one

obtains in the heavy-quark limit

$$\langle H^{(f')}(v')|\bar{h}_{v'}^{(f')}\Gamma h_v^{(f)}|H^{(f)}(v)\rangle = \xi(vv')\ \mathrm{Tr}\ \left\{\overline{\mathcal{H}(v)}\Gamma\mathcal{H}(v)\right\}, \tag{2.16}$$

where Γ is some arbitrary Dirac matrix and $H(v)$ are the representation matrices for the two possibilities of coupling the heavy quark spin to the spin of the light degrees of freedom, which are in a spin-1/2 state for the ground state mesons

$$\mathcal{H}(v) = \frac{\sqrt{M_H}}{2}\begin{cases} (1+\not{v})\gamma_5 & 0^-,\ (\bar{q}Q)\ \text{meson} \\ (1+\not{v})\not{\epsilon} & 1^-,\ (\bar{q}Q)\ \text{meson with polarization } \epsilon. \end{cases} \tag{2.17}$$

Due to the spin and flavor independence of the heavy mass limit, the Isgur-Wise function ξ is the only non-perturbative information needed to describe all heavy-to-heavy transitions within a spin-flavor symmetry multiplet.

Similar statements may be derived for the spin symmetry doublets of the excited heavy mesons and also for the baryons. For example, the corresponding analogue of the Isgur-Wise function for the excited state heavy mesons will be called $\tau_{3/2,1/2}$, as we will see later.

2.3 Randall-Sundrum model

Our previous two examples of EFT were derived from approximate symmetries of QCD Lagrangian. We now discuss the effective theory of gravity proposed in an attempt to solve one of the puzzles left unexplained by the SM: TeV/Planck scale hierarchy problem. The model(s) were proposed in 1999 by Lisa Randall and Raman Sundrum. Randall-Sundrum models (RS models) imagine that the real world is a higher-dimensional Universe described by warped geometry. More concretely, our Universe is a five-dimensional, anti-de Sitter space; and, in the original model, the elementary particles, except for the graviton, are localized on a (3 + 1)-dimensional brane or branes. There are two popular models. The first, called RS1, has a finite size for the extra dimension with two branes, one at each end. The second, RS2, is similar to the first; but one brane has been placed infinitely far away, so there is only one brane left in the model. Later in this thesis, we will see application of RS1 model in search for RS gravitons; and now we will discuss it in more detail.

The only new particles in RS1 model were Kaluza-Klein (KK) gravitons with no SM gauge quantum numbers. Two 3-branes, one being "visible" with the other being "hidden", with tensions opposite to each other, rigidly reside at S_1/Z_2 orbifold fixed points, taken to be $\phi = 0, \pi$, where ϕ is the angular coordinate parameterizing the extra dimension. It is assumed that the extra-dimensional bulk is only populated by gravity, and that the SM lies on the brane with negative tension at $\phi = \pi$. Gravity is localized on the Planck brane at $\phi = 0$. The solution to Einstein's equations for this configuration, maintaining 4-dimensional Poincare invariance, is given by the 5-dimensional metric

$$ds^2 = e^{-2\sigma(\phi)}\eta_{\mu\nu}dx^\mu dx^\nu + r_c^2 d\phi^2 \,, \tag{2.18}$$

where the Greek indices run over ordinary 4-dimensional spacetime, $\sigma(\phi) = kr_c|\phi|$ with r_c being the compactification radius of the extra dimension, and $0 \leq |\phi| \leq \pi$. Here, k is a scale of order the Planck scale and relates the 5-dimensional Planck scale M to the bulk cosmological constant. Here, it is assumed that the 5-dimensional curvature R_5, where $R_5 = -20k^2$, satisfies $|R_5| < M^2$ with $M \sim M_{pl}$ (where $M_{pl} \simeq 2.44 \times 10^{18}$ GeV is the reduced Planck mass) so that this solution for the bulk metric can be trusted. Otherwise, higher order terms in the curvature would need to be kept in the initial action to maintain self-consistency.

Examination of the action in the 4-dimensional effective theory in the RS scenario yields

$$M_{pl}^2 = \frac{M^3}{k}(1 - e^{-2kr_c\pi}) \tag{2.19}$$

for the reduced effective 4-D Planck scale. A field on the SM brane with the fundamental mass parameter m_0 will appear to have the physical mass $m = e^{-kr_c\pi}m_0$. The TeV scales are thus generated from fundamental scales of order M_{pl} via a geometrical exponential factor, and the observed scale hierarchy is reproduced if $kr_c \simeq 11 - 12$. Due to the exponential nature of the warp factor, no additional large hierarchies are generated. This model thus provides an interesting interpretation of the electroweak scale.

However, the fact that the SM fields live only on the TeV brane leaves higher-dimensional operators in the 5D effective field theory suppressed only by the TeV scale which, in turn, generates unacceptably large contributions to flavor changing neutral current (FCNC) and

observables related to the SM electroweak precision tests (EWPT). A natural way to avoid this problem is to allow the SM fields to propagate in the extra dimension. In this scenario, there are KK excitations of the SM gauge and fermion fields, in addition to those of the graviton. These states have mass in the TeV range and are localized near the TeV brane. The SM particles are the zero-modes of the 5D fields, and the profile of a SM fermion in the extra dimension depends on its 5D mass. By localizing light fermions near the Planck brane and heavier ones near the TeV brane, the contributions to the FCNC and EWPT are suppressed by scales $\gg$ TeV. As a consequence, the KK graviton whose profile is peaked at the TeV brane will couple mostly to the top quark, the Higgs (or, by equivalence theorem, to the longitudinal W and Z bosons), and the KK excitations of the SM fields.

Experimentally, the fact that the underlying theory is higher-dimensional would be reflected in the KK spectrum of the particles, shall they be found. Starting with the five-dimensional action of the gauge theory and performing KK expansion of the 5-D fields, one arrives at the effective 4-D description. Let us demonstrate it for the pure U(1) gauge theory, starting with the action:

$$S_{_A} = -\frac{1}{4}\int d^5x\,\sqrt{-G}\;G^{^{MK}}G^{^{NL}}F_{_{KL}}F_{_{MN}}\,, \tag{2.20}$$

where $\sqrt{-G} \equiv |det\,(G_{_{MN}})\,|^{1/2} = e^{-4\sigma}$ and $F_{_{MN}}$ is the 5-dimensional field strength tensor given by

$$F_{_{MN}} = \partial_{_M}A_{_N} - \partial_{_N}A_{_M}\,. \tag{2.21}$$

Note that this definition does not involve the affine connection terms due to the antisymmetry of $F_{_{MN}}$. After an integration by parts, Eq. (2.20) yields

$$S_{_A} = -\frac{1}{4}\int d^5x\,\left[\eta^{\mu\kappa}\eta^{\nu\lambda}F_{\kappa\lambda}F_{\mu\nu} - 2\,\eta^{\nu\lambda}A_\lambda\,\partial_4\left(e^{-2\sigma}\partial_4 A_\nu\right)\right]\,, \tag{2.22}$$

where we have used gauge freedom to choose $A_4 = 0$. This is consistent with the gauge invariant equation $\oint dx^4 A_4 = 0$, which results from our assumption that A_4 is a Z_2-odd function of the extra dimension. This choice eliminates A_4 from the theory on the 3-brane, but it will not disturb the gauge invariance of the action in the effective 4-dimensional theory, as we will see below.

Let the KK expansion of A_μ be given by

$$A_\mu(x,\phi) = \sum_{n=0}^{\infty} A_\mu^{(n)}(x)\,\frac{\chi^{(n)}(\phi)}{\sqrt{r_c}}\,, \tag{2.23}$$

with $x^4 = r_c\phi$. Using the expansion in Eq. (2.22) and integrating over ϕ give

$$S_{_A} = \int d^4x \sum_{n=0}^{\infty}\left[-\frac{1}{4}\,\eta^{\mu\kappa}\eta^{\nu\lambda}F_{\kappa\lambda}^{(n)}F_{\mu\nu}^{(n)} - \frac{1}{2}\,m_n^2\eta^{\nu\lambda}A_\nu^{(n)}A_\lambda^{(n)}\right], \tag{2.24}$$

where $F_{\mu\nu}^{(n)} = \partial_\mu A_\nu^{(n)} - \partial_\nu A_\mu^{(n)}$. In doing this, we have required that the ϕ-dependent wave-functions satisfy the orthonormality condition

$$\int_{-\pi}^{\pi} d\phi\,\chi^{(m)}\chi^{(n)} = \delta^{mn} \tag{2.25}$$

and the differential equation

$$\frac{-1}{r_c^2}\frac{d}{d\phi}\left(e^{-2\sigma}\frac{d}{d\phi}\,\chi^{(n)}\right) = m_n^2\,\chi^{(n)}\,. \tag{2.26}$$

The expression in Eq. (2.24) is the action for gauge fields $A_\mu^{(n)}$ of mass m_n in 4-dimensional Minkowski space; and, as mentioned above, for the zero mode (with $m_n = 0$), $S_{_A}$ has 4-dimensional gauge invariance.

Equipped with the theoretical background, we are now in a position to see how these formalisms are applied in the particle physics research.

CHAPTER 3. Decay $\Omega^- \to \Xi^-\pi^+\pi^-$ in heavy-baryon chiral perturbation theory

For our first application, we consider $\Omega^- \to \Xi^-\pi^+\pi^-$ decay in the heavy-baryon chiral perturbation theory. It is based on my work with my collaborators J.Tandean and G.Valencia [1] where interested reader may find additional details.

3.1 Introduction

It was suggested many years ago that the decay $\Omega^- \to \Xi^-\pi^+\pi^-$ should be dominated by the $\Xi^{*0}(1530)$ intermediate state [2, 3]. Under this assumption, the current Particle Data Group (PDG) [4] branching ratio for $\Omega^- \to \Xi^{*0}\pi^-$ has been deduced from the measurement of $\mathcal{B}(\Omega^- \to \Xi^-\pi^+\pi^-)$ [5]. More recently, the HyperCP collaboration has reported a preliminary measurement of $\Omega^- \to \Xi^-\pi^+\pi^-$ that is very surprising in that the distribution of the $\Xi^-\pi^+$ invariant-mass apparently shows no evidence for the $\Xi^{*0}(1530)$ dominance [6].

Motivated by this result, we revisit the calculation of the rate for this decay mode using heavy-baryon chiral perturbation theory (HBχPT). We first present a leading-order calculation that reproduces the expectation that the decay is completely dominated by the $\Xi^{*0}(1530)$ intermediate state.

We next explore whether higher-order contributions can reconcile the calculation with the preliminary HyperCP result. To this end, we consider the effect of next-to-leading-order diagrams, which occur at tree level.

In the spirit of the perturbation theory, all Feynman diagrams are drawn using effective vertices as in Fig.3.1. These effective vertices are defined in Fig.3.2.

3.2 Leading-order calculation

The amplitude for $\Omega^- \to \Xi^-(p_\Xi)\,\pi^+(p_+)\,\pi^-(p_-)$ can be written in the heavy-baryon approach as

$$\mathcal{M}(\Omega^- \to \Xi^-\pi^+\pi^-) \;=\; -\bar{u}_\Xi \left(A_+\, p_+^\mu + A_-\, p_-^\mu + 2B_+\, S_v\cdot p_-\, p_+^\mu + 2B_-\, S_v\cdot p_+\, p_-^\mu\right) u_{\Omega\mu}\ , \tag{3.1}$$

where $A_\pm$ and $B_\pm$ are independent form-factors and S_v is the spin operator. The most general form of the amplitude has eight independent form-factors [2], and we have included here only the ones that receive contributions from the leading-order and next-to-leading-order diagrams that we consider. The partial decay width resulting from the amplitude above is

$$d\Gamma(\Omega^- \to \Xi^-\pi^+\pi^-) \;=\; \frac{1}{32\left(2\pi\, m_\Omega\right)^3}\,\overline{|\mathcal{M}(\Omega^- \to \Xi^-\pi^+\pi^-)|^2}\, dm^2_{\Xi^-\pi^+}\, dm^2_{\Xi^-\pi^-}\ , \tag{3.2}$$

where $m^2_{\Xi^-\pi^\pm} = \left(p_\Xi + p_\pm\right)^2$ and

$$\begin{aligned}\overline{|\mathcal{M}(\Omega^- \to \Xi^-\pi^+\pi^-)|^2} \;=\; & \tfrac{4}{3}\, m_\Omega\, m_\Xi \Big\{ \left|A_+\right|^2 \boldsymbol{p}_+^2 + \left|A_-\right|^2 \boldsymbol{p}_-^2 + 2\,\mathrm{Re}\big(A_+^* A_-\big)\, \boldsymbol{p}_+\cdot\boldsymbol{p}_- \\ & + \Big[\left|B_+\right|^2 + \left|B_-\right|^2 + \mathrm{Re}\big(B_+^* B_-\big)\Big]\, \boldsymbol{p}_+^2\, \boldsymbol{p}_-^2 \\ & + \mathrm{Re}\big(B_+^* B_-\big)\, \left(\boldsymbol{p}_+\cdot\boldsymbol{p}_-\right)^2 \Big\}\ ,\end{aligned} \tag{3.3}$$

with $\boldsymbol{p}_\pm$ denoting the three-momenta of the pions in the Ω^- rest frame.

The chiral Lagrangian describing the interactions of the lowest-lying mesons and baryons is written down in terms of the lightest meson-octet, baryon-octet, and baryon-decuplet fields [7, 8, 9]. As we saw in Chapter 2, the meson and baryon octets are collected into 3×3 matrices φ (this matrix is $\varphi = \frac{M}{\sqrt{2}}$ in Eq.2.1) and B, respectively; and the decuplet fields are represented by the Rarita-Schwinger tensor T^μ_{abc}, which is completely symmetric in its SU(3) indices (a,b,c). As also described in Chapter 2, the octet mesons enter through the exponential $\Sigma = \xi^2 = \exp(i\varphi/f)$, where now the pion-decay constant $f = f_\pi \approx 93\,\mathrm{MeV}$ due to the fact that $\varphi = \frac{M}{\sqrt{2}}$ in Eq.2.1.

In the heavy-baryon formalism [9], the baryons in the chiral Lagrangian are described by velocity-dependent fields, B_v and T^μ_v. For the strong interactions, the Lagrangian at lowest

order in the derivative and m_s expansions is given by

$$\begin{aligned}\mathcal{L}_{\rm s} &= \big\langle \bar B_v\, iv^\mu \big(\partial_\mu B_v + \big[\mathcal{V}_\mu, B_v\big]\big)\big\rangle + 2D\,\big\langle \bar B_v S_v^\mu \,\{\mathcal{A}_\mu, B_v\}\big\rangle + 2F\,\big\langle \bar B_v S_v^\mu \,\big[\mathcal{A}_\mu, B_v\big]\big\rangle \\ &\quad - \bar T_v^\mu\, iv\cdot\mathcal{D} T_{v\mu} + \Delta m\, \bar T_v^\mu T_{v\mu} + \mathcal{C}\,\big(\bar T_v^\mu \mathcal{A}_\mu B_v + \bar B_v \mathcal{A}_\mu T_v^\mu\big) + 2\mathcal{H}\,\bar T_v^\mu S_v\cdot\mathcal{A} T_{v\mu} \\ &\quad + b_D\,\big\langle \bar B_v\,\{M_+, B_v\}\big\rangle + b_F\,\big\langle \bar B_v\,\big[M_+, B_v\big]\big\rangle \,+\, c\,\bar T_v^\mu M_+ T_{v\mu} \end{aligned} \tag{3.4}$$

where only the relevant terms are shown, $\langle\cdots\rangle \equiv {\rm Tr}(\cdots)$ in flavor-SU(3) space, Δm denotes the mass difference between the decuplet and the octet baryons in the chiral limit, $\mathcal{V}^\mu = \frac{1}{2}\big(\xi\,\partial^\mu\xi^\dagger + \xi^\dagger\,\partial^\mu\xi\big)$, $\mathcal{A}^\mu = \frac{i}{2}\big(\xi\,\partial^\mu\xi^\dagger - \xi^\dagger\,\partial^\mu\xi\big)$, $\mathcal{D}^\mu T^\nu_{klm} = \partial^\mu T^\nu_{klm} + \mathcal{V}^\mu_{kn} T^\nu_{lmn} + \mathcal{V}^\mu_{ln} T^\nu_{kmn} + \mathcal{V}^\mu_{mn} T^\nu_{kln}$, and $M_+ = \xi^\dagger M \xi^\dagger + \xi M^\dagger \xi$, with $M = {\rm diag}(\hat m, \hat m, m_s) = {\rm diag}\big(m_\pi^2, m_\pi^2, 2m_K^2 - m_\pi^2\big)/\big(2B_0\big)$ in the isospin-symmetric limit $m_u = m_d = \hat m$. The constants D, F, $\mathcal{C}$, $\mathcal{H}$, B_0, $b_{D,F}$, and c are free parameters which can be extracted from the data.

As is well known, the weak interactions responsible for the hyperon nonleptonic decays are described by a $|\Delta S| = 1$ Hamiltonian that transforms as $(8_{\rm L}, 1_{\rm R}) \oplus (27_{\rm L}, 1_{\rm R})$ under ${\rm SU(3)_L}\times{\rm SU(3)_R}$ rotations. It is also known empirically that the octet term dominates the 27-plet term. We therefore assume in what follows that the decays are completely characterized by the $(8_{\rm L}, 1_{\rm R})$, $|\Delta I| = 1/2$ interactions. The leading-order chiral Lagrangian for such interactions is [8, 10]

$$\mathcal{L}_{\rm w} \;=\; h_D\,\Big\langle \bar B_v\,\Big\{\xi^\dagger h \xi\,,\, B_v\Big\}\Big\rangle + h_F\,\Big\langle \bar B_v\,\Big[\xi^\dagger h \xi\,,\, B_v\Big]\Big\rangle + h_C\,\bar T_v^\mu\,\xi^\dagger h \xi\, T_{v\mu} \;+\; {\rm H.c.}\,, \tag{3.5}$$

where h is a 3×3 matrix having elements $h_{kl} = \delta_{k2}\delta_{3l}$ and the parameters $h_{D,F,C}$ can be fixed from two-body hyperon nonleptonic decays.

From $\mathcal{L}_{\rm w}$ together with $\mathcal{L}_{\rm s}$, we can derive the $\mathcal{O}(p^0)$ diagrams displayed in Fig. 3.1 and Fig. 3.2. They provide the leading-order contributions to the $A_\pm$ and $B_\pm$ form factors in Eq. (3.1), namely

$$A_+^{(0)} \;=\; \frac{+\mathcal{C}\,h_C}{6\,f^2\,\big(E_\Xi + E_+ - \bar m_{\Xi^*}\big)}\,, \tag{3.6a}$$

$$A_-^{(0)} \;=\; 0\,, \tag{3.6b}$$

$$B_+^{(0)} \;=\; \frac{-\mathcal{C}\,\mathcal{H}\,h_C}{18\,f^2\,\big(m_\Omega - m_{\Xi^*}\big)\big(E_\Xi + E_+ - \bar m_{\Xi^*}\big)}\,, \tag{3.6c}$$

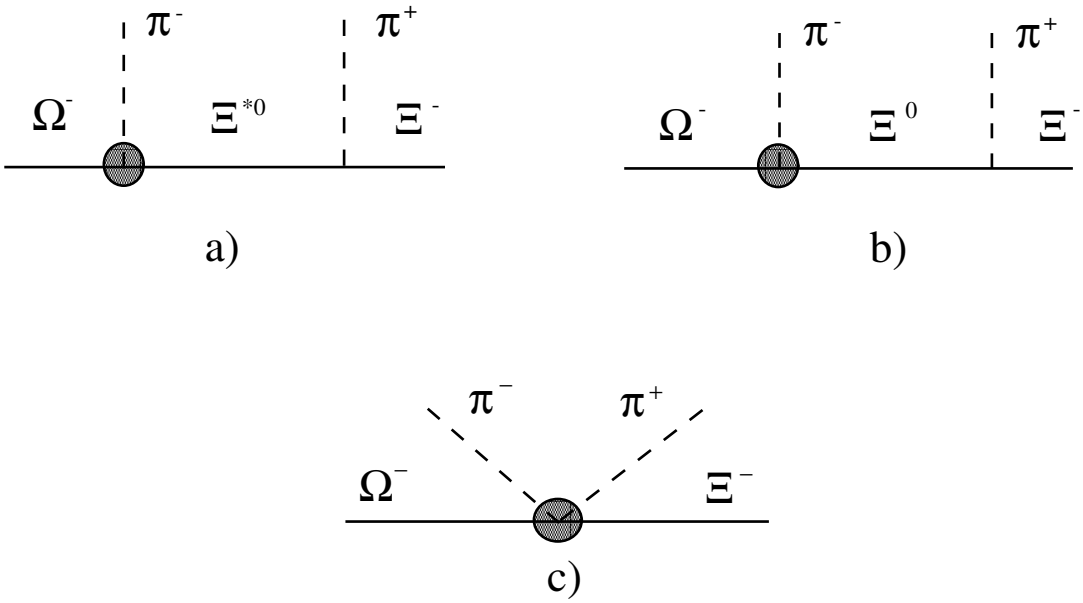

Figure 3.1 Diagrams contributing to $\Omega^- \to \Xi^-\pi^+\pi^-$. Each solid blob represents an effective weak vertices which are defined in Fig.3.2 and strong vertices follow from $\mathcal{L}_{\rm s}$ in Eq. (3.4).

$$B_-^{(0)} = \frac{-\mathcal{C}\,(D-F)\,h_C}{6\,f^2\,(m_\Omega - m_{\Xi^*})(E_\Xi + E_+ - m_\Xi)} + \frac{\mathcal{C}\,\mathcal{H}\,h_C}{27\,f^2\,(m_\Omega - m_{\Xi^*})(E_\Xi + E_+ - \bar{m}_{\Xi^*})}\ , \tag{3.6d}$$

where $\bar{m}_{\Xi^*} = m_{\Xi^*} - \frac{i}{2}\Gamma_{\Xi^*}$.

Numerically, to evaluate the decay rates resulting from the form factors above, we employ the tree-level values of the strong and weak parameters. Specifically,

$$D \;=\; 0.80\ , \qquad F \;=\; 0.46\ , \qquad |\mathcal{C}| \;=\; 1.7 \tag{3.7}$$

from the hyperon semileptonic decays and the strong decays $T \to B\varphi$, but a tree-level value of $\mathcal{H}$ is not yet available from data. Since nonrelativistic quark models [9] give $3F = 2D$, $\mathcal{C} = -2D$, and $\mathcal{H} = -3D$, which are well satisfied by D, F, and $\mathcal{C}$, we adopt

$$\mathcal{H} \;=\; -2.4\ . \tag{3.8}$$

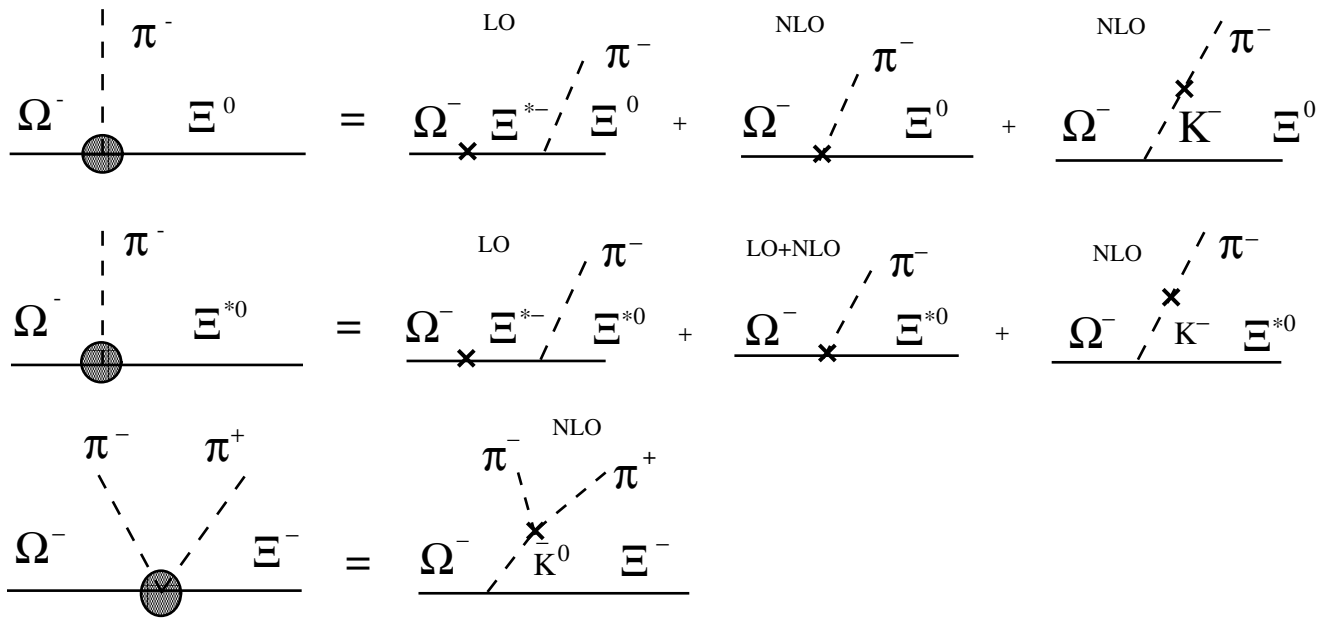

Figure 3.2 Contributions to the effective weak vertices up to NLO in HBχPT contributing to $\Omega^- \to \Xi^-\pi^+\pi^-$. Weak vertices (denoted by x) follow at LO from $\mathcal{L}_{\rm w}$ in Eq. (3.5) and at NLO from $\mathcal{L}'_{\rm w}$ in Eq. (3.11b). Correspondindly, strong vertices follow from $\mathcal{L}_{\rm s}$ in Eq. (3.4) or $\mathcal{L}'_{\rm s}$ in Eq. (3.11a).

For the weak parameters, we have

$$h_C \;=\; 3.42\times 10^{-8}\ \text{GeV}\ , \tag{3.9}$$

$h_D = -1.45\times 10^{-8}\,\text{GeV}$, and $h_F = 3.50\times 10^{-8}\,\text{GeV}$, extracted from a simultaneous tree-level fit to the S-wave octet-hyperon and P-wave Ω^- nonleptonic two-body decays, as $h_{D,F}$ contribute not only to the octet-hyperon decays but also to $\Omega^- \to \Lambda\bar{K}$, whereas h_C contributes to $\Omega^- \to \Lambda\bar{K}, \Xi\pi$ [10]. As seen above, h_C is the only weak parameter in the lowest-order contributions to $\Omega^- \to \Xi^-\pi^+\pi^-$.

The resulting branching ratio,

$$\mathcal{B}(\Omega^- \to \Xi^-\pi^+\pi^-) \;=\; 5.4\times 10^{-3}\ , \tag{3.10}$$

is roughly an order of magnitude larger than the preliminary number reported by HyperCP, $\mathcal{B}(\Omega^- \to \Xi^-\pi^+\pi^-) = [3.6 \pm 0.3(\text{stat})] \times 10^{-4}$ [6], and also the current PDG value, $\mathcal{B}(\Omega^- \to \Xi^-\pi^+\pi^-) = \left(4.3^{+3.4}_{-1.3}\right) \times 10^{-4}$ [4]. In Fig. 3.3(a), we display the corresponding $\Xi^-\pi^+$ invariant-mass distribution. As expected, these results are dominated by the Ξ^* resonance. Notice that the leading-order rate is proportional to $|\mathcal{C}h_C|^2$ so there is a large parametric uncertainty in this prediction. For example, if both $\mathcal{C}$ and h_C were 30% smaller than the values we used, the predicted rate would be four times smaller. The general dependence of the leading-order branching ratio on $|\mathcal{C}h_C|$ is shown in Fig. 3.3(b).

The HyperCP data is not available in a format suitable for direct comparison with our result due to detector effects. However, their results indicate that a uniform phase-space distribution is a much better fit to the data than a Ξ^*-dominated one [6]. In Fig. 3.4 we plot the $m_{\Xi^-\pi^+}$ distributions resulting from our leading-order amplitude (solid curve) and from assuming a uniform-phase-space decay distribution (dashed curve), both normalized to reproduce the central value of HyperCP's result. The structure of the leading-order amplitude, from Eq. (3.6), with all the terms being proportional to $\mathcal{C}h_C$, is such that the Ξ^* resonance is always the dominant feature of the spectrum. This leads us to investigate in the next section whether any of the next-to-leading-order corrections can modify the predicted spectrum in the direction indicated by experiment.

3.3 Calculation to next-to-leading order

At the next-to-leading order, $\mathcal{O}(p)$, there are two types of contributions. The first type of contributions is that in which the weak transition occurs only between mesons. To compute these contributions, we need the leading-order, $\mathcal{O}(p^2)$, strong and weak Lagrangians for mesons, which are given respectively by [7, 11]

$$\mathcal{L}'_{\rm s} \;=\; \tfrac{1}{4} f^2 \left\langle \partial^\mu \Sigma^\dagger \, \partial_\mu \Sigma \right\rangle + \tfrac{1}{2} B_0 f^2 \left\langle M_+ \right\rangle \;, \tag{3.11a}$$

$$\mathcal{L}'_{\rm w} \;=\; \gamma_8 f^2 \left\langle h \, \partial_\mu \Sigma \, \partial^\mu \Sigma^\dagger \right\rangle \;+\; \text{H.c.} \;, \tag{3.11b}$$

where the parameter γ_8 is found from $K \to \pi\pi$ data to be

$$\gamma_8 \;=\; -7.8 \times 10^{-8} \;, \tag{3.12}$$

the sign following from various predictions [12]. Notice again different normalization of the first term in Eq.3.11 compared to Eq.2.2 due to different choice for the pion decay constant.

The contributions of the γ_8 term are interesting because the $|\Delta S| = 1$ weak transitions in the meson sector are larger than naive expectations. In particular, γ_8 is several times larger than its naturally expected value $\left(\sim 1 \times 10^{-8}\right)$ and therefore could make its contributions numerically comparable to the lower-order ones.

With weak vertices from the γ_8 term alone, plus strong vertices from $\mathcal{L}_{\rm s}$ and $\mathcal{L}'_{\rm s}$, we derive the next-to-leading-order (NLO) diagrams displayed in Fig. 3.1 and Fig. 3.2, and contain kaons. They provide the NLO contributions to the $A_\pm$ and $B_\pm$ form factors in Eq. (3.1), namely

$$A_+^{(1)} \;=\; \frac{-\mathcal{C}\,\gamma_8}{f^2}\;\frac{m_\pi^2 - s_{+-}}{m_K^2 - s_{+-}} \;, \tag{3.13a}$$

$$A_-^{(1)} \;=\; A_+^{(1)} \;, \tag{3.13b}$$

$$B_+^{(1)} \;=\; \frac{-\mathcal{C}\,\mathcal{H}}{3f^2}\;\frac{\gamma_8\, m_\pi^2}{\left(m_K^2 - m_\pi^2\right)\left(E_\Xi + E_+ - \bar{m}_{\Xi^*}\right)} \;, \tag{3.13c}$$

$$\begin{aligned} B_-^{(1)} \;=\; & \frac{-\mathcal{C}\,(D-F)}{f^2}\;\frac{\gamma_8\, m_\pi^2}{\left(m_K^2 - m_\pi^2\right)\left(E_\Xi + E_+ - m_\Xi\right)} \\ & + \frac{2\mathcal{C}\,\mathcal{H}}{9f^2}\;\frac{\gamma_8\, m_\pi^2}{\left(m_K^2 - m_\pi^2\right)\left(E_\Xi + E_+ - \bar{m}_{\Xi^*}\right)} \;. \end{aligned} \tag{3.13d}$$

In obtaining these results, we have used the relations

$$m_\Omega - m_{\Xi^*} \;=\; \frac{2c}{3}\left(m_s - \hat{m}\right) \;, \qquad m_\pi^2 \;=\; 2B_0\,\hat{m} \;, \qquad m_K^2 \;=\; B_0\left(m_s + \hat{m}\right) \;, \tag{3.14}$$

which follow from $\mathcal{L}_{\rm s}$ and $\mathcal{L}'_{\rm s}$.

There is another type of NLO contribution to the amplitudes. It is given by the two remaining diagrams in Fig. 3.1 and Fig. 3.2 in which the weak vertices are from a NLO Lagrangian. Many of the parameters in NLO Lagrangians are not known, and so it is not

possible at present to include their contributions in a detailed way. The weak Lagrangian at $\mathcal{O}(p)$ that generates $\Omega^-\Xi^*\pi$ and $\Omega^-\Xi\pi$ vertices is

$$\begin{aligned}\tilde{\mathcal{L}}'_{\rm w} &= \frac{h_{\Omega\Xi^*\pi}}{f}\, v^\alpha\, \partial_\alpha\pi^+\, \bar{\Xi}^{*0}\cdot\Omega^- \;+\; \frac{\tilde{h}_{\Omega\Xi^*\pi}}{f}\, \partial_\alpha\pi^+\, \bar{\Xi}^{*0}_\mu\, 2S_v^\alpha\, \Omega^{-\mu} \\ &\quad + \frac{h_{\Omega\Xi\pi}}{f}\, \partial^\mu\pi^+\, \bar{\Xi}^0\, \Omega^-_\mu \;+\; \cdots\;, \end{aligned} \tag{3.15}$$

where only the relevant terms are displayed and $h_{\Omega\Xi^*\pi}$, $\tilde{h}_{\Omega\Xi^*\pi}$, and $h_{\Omega\Xi\pi}$ are unknown parameters. These two diagrams yield the NLO contributions

$$\tilde{A}^{(1)}_+ \;=\; \frac{-\mathcal{C}\, h_{\Omega\Xi^*\pi}\, E_-}{\sqrt{6}\, f^2\left(E_\Xi + E_+ - \bar{m}_{\Xi^*}\right)}\;, \tag{3.16a}$$

$$\tilde{A}^{(1)}_- \;=\; 0\;, \tag{3.16b}$$

$$\tilde{B}^{(1)}_+ \;=\; \frac{-\mathcal{C}\, \tilde{h}_{\Omega\Xi^*\pi}}{\sqrt{6}\, f^2\left(E_\Xi + E_+ - \bar{m}_{\Xi^*}\right)}\;, \tag{3.16c}$$

$$\tilde{B}^{(1)}_- \;=\; \frac{(D-F)\, h_{\Omega\Xi\pi}}{\sqrt{2}\, f^2\left(E_\Xi + E_+ - m_\Xi\right)} + \frac{2\mathcal{C}\, \tilde{h}_{\Omega\Xi^*\pi}}{3\sqrt{6}\, f^2\left(E_\Xi + E_+ - \bar{m}_{\Xi^*}\right)}\;. \tag{3.16d}$$

Numerically, we adopt the parametric variations

$$0 \;\le\; \left|h_{\Omega\Xi^*\pi}\right|,\, \left|\tilde{h}_{\Omega\Xi^*\pi}\right|,\, \left|h_{\Omega\Xi\pi}\right| \;\le\; 2\times 10^{-8}\;, \tag{3.17}$$

where the upper limit is the expectation from naive dimensional analysis.

As mentioned above, there are additional NLO contributions that are not included in our calculation above because they depend on more unknown parameters. We can still estimate the uncertainty in our results arising from those terms by allowing the LO parameters to vary between their value as obtained from tree-level fits and their value as obtained from one-loop fits. For our numerics we will specifically consider parameter values obtained from fits at one-loop order, which are available in the literature [9, 13, 14]. We begin by noticing that our results in Eqs. (3.6), (3.13) and (3.16) show that f is a common factor affecting the overall normalization only. Similarly, $\mathcal{C}$ is a common factor, except for the first term in Eq. (3.16d), which is numerically small. Consequently, we fix f and $\mathcal{C}$ to their tree-level values, noting that

the resulting decay rate scales with an overall factor $\mathcal{C}^2/f^4$. In addition, we keep γ_8 at its value in Eq. (3.12), as it is well determined. Thus, the ranges of the strong parameters we consider are

$$0.21 \;\le\; D-F \;\le\; 0.34\;, \qquad -2.4 \;\le\; \mathcal{H} \;\le\; -1.6\;. \tag{3.18}$$

On the other hand, since the range of the weak parameter h_C from one-loop fits is large [14], $-2 \le 10^7 h_C \le 4$, we let it vary so as to reproduce the experimental decay rates.

In Fig. 3.5(a) we display the branching ratios calculated from the leading-order (LO) and the NLO amplitudes above. The black (dark gray) band in the figure shows the effects of the parametric variations given in Eq. (3.18) on the branching ratio obtained from the LO amplitude alone (the LO amplitude and only the γ_8 terms in the NLO amplitude). The light-gray region results from the LO and the NLO amplitudes considered above and varying the parameters according to Eqs. (3.17) and (3.18). The dotted lines in this figure bound the range $3.3 \le 10^4\,\mathcal{B}(\Omega^- \to \Xi^-\pi^+\pi^-) \le 3.9$ implied by the preliminary HyperCP data. Evidently, this data can be reproduced in the three cases.

The corresponding $m_{\Xi^-\pi^+}$ distributions are plotted in Figs. 3.5(b) and (c) for $h_C < 0$ and $h_C > 0$, respectively, with the variations of the other parameters for the different bands being the same as in Fig. 3.5(a). The h_C ranges used in (b) and (c) are $0.84 < 10^8\,|h_C| < 0.92$ for the black bands, $-1.05 < 10^8\,h_C < -0.90$ and $0.55 < 10^8\,h_C < 0.65$ for the dark-gray bands, and $-1.8 < 10^8\,h_C < 0$ and $0 < 10^8\,h_C < 1.4$ for the light-gray bands, all of which have been inferred from the corresponding bands in (a). The figures indicate that some softening of the Ξ^* dominance in the spectrum is possible with the inclusion of higher-order contributions.

3.4 Conclusions

We have evaluated the decay $\Omega^- \to \Xi^-\pi^+\pi^-$ in heavy-baryon chiral perturbation theory. At the leading order, we found a spectrum dominated by the $\Xi^*(1530)$, as had been suggested before. This shape is in conflict with the recent preliminary data from HyperCP. The total branching ratio is also in conflict with experiment for the central values of $\mathcal{C}$ and h_C, but it

suffers from a large parametric uncertainty. This uncertainty, however, does not affect the shape of the $m_{\Xi^-\pi^+}$ invariant mass distribution.

A complete calculation at next-to-leading-order contains too many unknown parameters to be phenomenologically useful. We have investigated the effect of the NLO corrections in three different ways. First, we considered the diagrams in which the weak transition occurs in the meson sector. These corrections are induced by the low-energy constant γ_8 which is known from kaon decay. Second, we considered the NLO terms in the weak effective Lagrangian which introduce three new effective constants. We studied the effect of these constants by varying their value between zero and the value suggested by naive dimensional analysis. Third and last, we varied the LO parameters in ranges that included their values as determined from tree-level and one-loop fits to other hyperon decay modes. The difference between the two kinds of fit is indicative of the size of NLO counter-terms that we have not included explicitly. When all these factors are considered, we found that it is possible to lower the branching ratio and soften the importance of the Ξ^* in the $m_{\Xi^-\pi^+}$ distribution, as suggested by the data.

In this project we witnessed how the disagreement between experiment and LO theoretical prediction shows the importance of NLO contributions. Even though the complete NLO prediction was not possible, I benefited from this project in many ways. First, I learned how to calculate experimentally observable quatities in chiral perturbation theory. The calculations in this framework often show non-trivial interplay between various terms from different diagrams or even different orders. Second, I learned the meaning of many phenomenological parameters as well as experimental origin for their values. In the next chapter we will consider particles containing charm and bottom quarks absent in this project. As we will see, they will be treated in a different way.

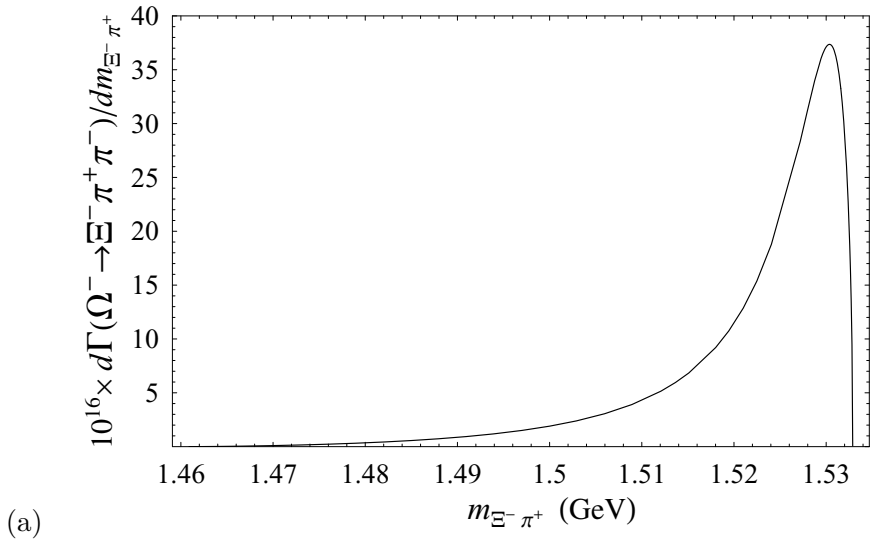

(a)

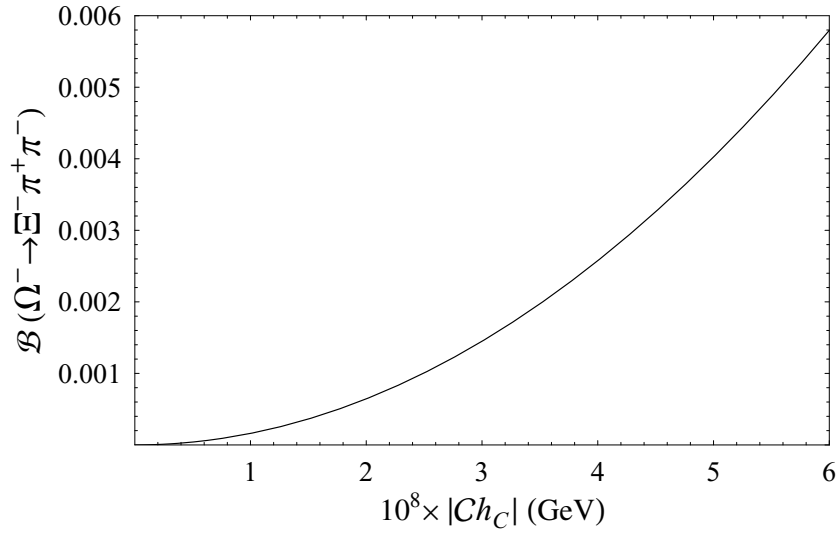

(b)

Figure 3.3 (a) Distribution of $\Xi^-\pi^+$ invariant-mass in $\Omega^- \to \Xi^-\pi^+\pi^-$ at leading order with parameter values in Eqs. (3.7)-(3.8), and (b) its branching ratio as function of $|\mathcal{C}h_C|$ with $D-F$ and $\mathcal{H}$ values in Eqs. (3.7) and (3.8).

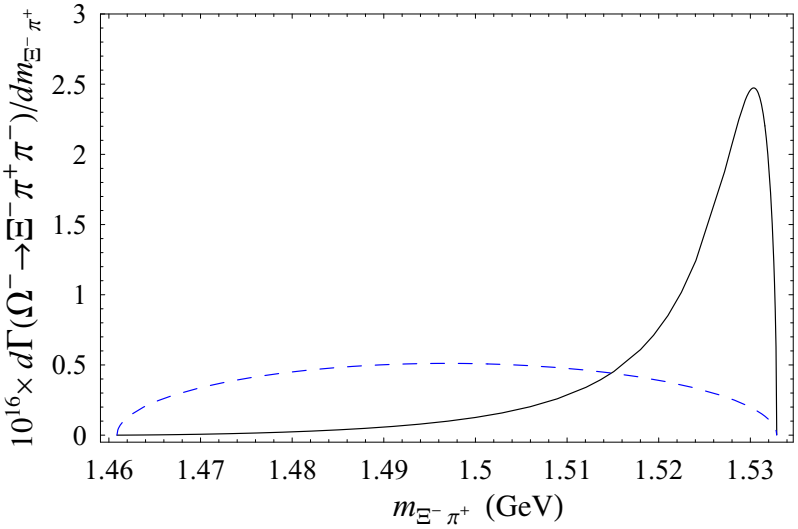

Figure 3.4 Distributions of $\Xi^-\pi^+$ invariant-mass in $\Omega^- \to \Xi^-\pi^+\pi^-$ obtained from our leading-order amplitude (solid curve) and from the assumption of uniform-phase-space decay distribution (dashed curve), both normalized to yield $\mathcal{B}(\Omega^- \to \Xi^-\pi^+\pi^-) = 3.6 \times 10^{-4}$.

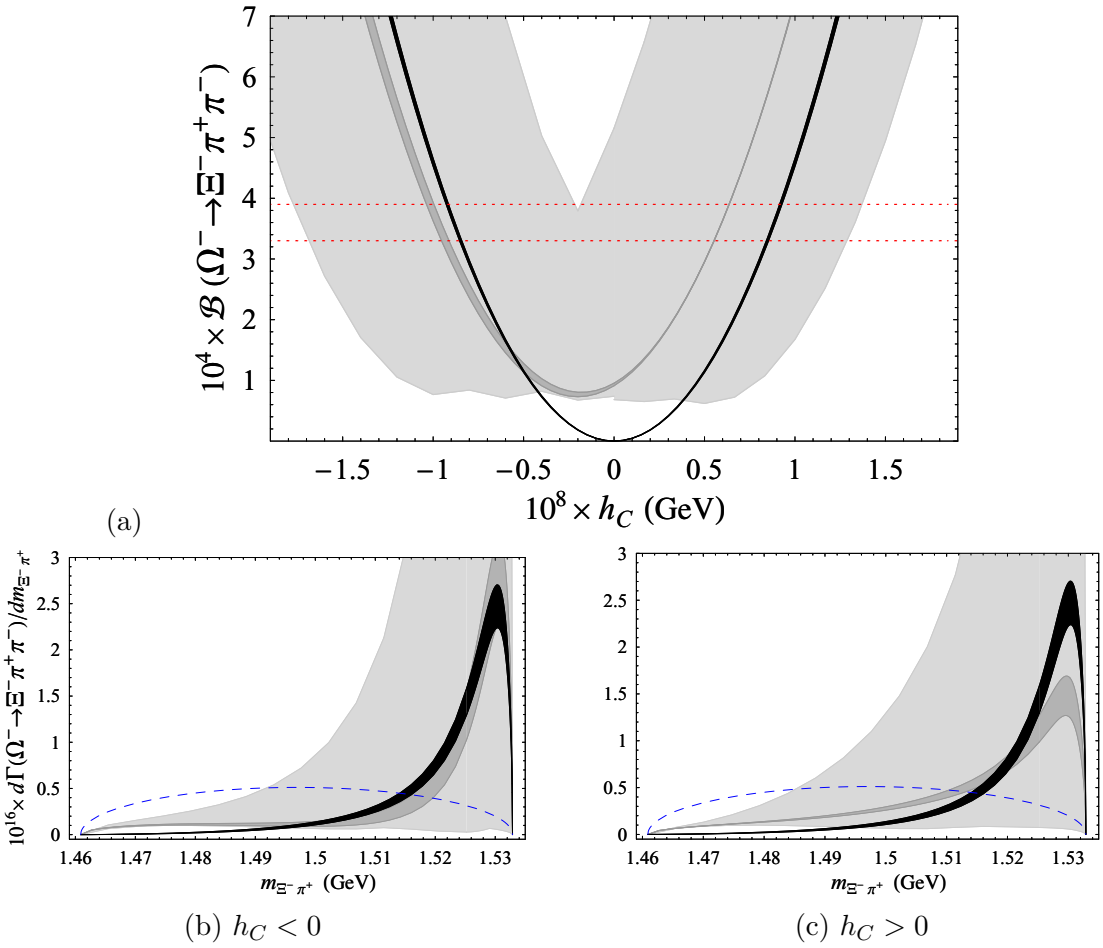

(a)

(b) $h_C < 0$

(c) $h_C > 0$

Figure 3.5 (a) Branching ratios for $\Omega^- \to \Xi^- \pi^+ \pi^-$ and (b,c) the corresponding distributions of $\Xi^- \pi^+$ invariant-mass. The black (dark gray) band comes from the LO amplitude only (the LO amplitude and the γ_8 terms in the NLO amplitude), and the light-gray band results from the LO and NLO amplitudes we consider, as described in the text. The dotted lines in (a) bound the range implied by the preliminary HyperCP data. The dashed curves in (b) and (c) have been reproduced from Fig. 3.4.

CHAPTER 4. B-physics

In this chapter we consider applications of χPT and HQET to the decay of B mesons. B-physics is a large and active field, and having large BaBar experimental group here at Iowa State University (ISU) has allowed me to be in the frontier of experimental discoveries in it. I concentrated on phenomenological analysis of latest measurements by BaBar collaboration which were of interest to our experimental group at ISU. In particular, collaborating with my adviser G.Valencia, we studied recently reported observation by BaBar of the decay mode $B^- \to D_s^+ K^- \pi^-$ [15]. The $D_s^+ K^-$ pair could come from intermediate charm resonances, and we found that they play a significant role despite their masses lying below the $m(D_s K)$ production threshold. As our investigation was undergoing in parallel with experimental analysis for this decay mode, we continuously exchanged ideas with BaBar representatives (especially with Soeren Prell and Vitaly Eyges) which provided me with invaluable physics input, especially during my visit to SLAC. My other B-physics project with Dr.Valencia was focused on analysis of weak radiative decays of B mesons [16]. With the $B^+ \to D^{\star +}\gamma$ mode as a potential probe for $|V_{ub}|$, we reviewed the $B \to D^\star \gamma$ decay modes in the framework of HQET and χPT and improved the existing LO results in the literature by including the positive parity intermediate states. Then, we extended these ideas to the double radiative decay modes $B \to D\gamma\gamma$ and found that positive parity states play an important role in both $B \to D^\star\gamma$ and $B \to D\gamma\gamma$ channels. We now discuss both of these projects in detail and start with the weak radiative decays of the B mesons first.

4.1 Radiative B decays

We begin with the (tree-level) weak radiative decays of B mesons. We present a numerical estimate for the inclusive $b \to X_c\gamma(\gamma)$ modes based on the free-quark decay. We then discuss the $B \to D^\star\gamma$ modes in the framework of heavy quark effective theory and chiral perturbation theory. Continuing along these lines, we will calculate the double radiative decay rates for the $B \to D\gamma\gamma$ decay modes. We will find that the $b \to X_c\gamma\gamma$ rate is about an order of magnitude larger than the corresponding $b \to X_s\gamma\gamma$ rate. We also will find that the branching ratio for the $B \to D\gamma\gamma$ mode with the biggest CKM angles is at the (few $\times 10^{-8}$) level, comparable to predictions for $B \to K\gamma\gamma$.

4.1.1 Introduction

The radiative penguin b decay of the form $b \to s\gamma$ has received much attention in the literature because it is sensitive to certain types of physics beyond the standard model. The Heavy Flavor Averaging Group (HFAG) quotes an average for the measured branching ratio $B(b \to s\gamma) = (354^{+30}_{-28}) \times 10^{-6}$ [17]. Also, the double radiative decay mode $b \to s\gamma\gamma$ has been studied extensively due to the possibility of measuring it at a Super-B factory at the 10^{-7} level [18], which is the level it is expected to occur in the standard model [20, 19].

We may also have a tree-level radiative b decay which proceeds via the charged current as in $b \to X_c\gamma(\gamma)$ and $b \to X_u\gamma(\gamma)$ channels. These modes are expected to be dominated by standard model physics and have received much less attention. To fill this gap, we begin with a simple numerical estimate for these modes suggesting that $b \to X_c\gamma\gamma$ can also be observed at a Super-B factory. We then turn our attention to some of the exclusive modes.

4.1.2 $\mathbf{b \to X_c\gamma}$ and $\mathbf{b \to X_c\gamma\gamma}$

We work in the free quark approximation where $b \to X_c\gamma$ and $b \to X_c\gamma\gamma$ arise from the tree-level quark processes $b \to c\bar{u}d\gamma$ and $b \to c\bar{u}d\gamma\gamma$ (we take $V_{ud} = 1$). Our goal is to compare these processes to the one-loop processes $b \to X_s\gamma$ and $b \to X_s\gamma\gamma$; and in order to do this, we will use the CompHEP package [23].

As the photon energy range studied by the Belle collaboration [24] is 1.8 GeV $\leq E_\gamma \leq$ 2.8 GeV, this will be our first acceptance cut. We also impose a $5^\circ \leq \theta_{min} \leq 20^\circ$ separation on a minimum angle θ_{min} between the photon and the final state quarks, in parallel with $b \to X_s\gamma\gamma$ mode discussed next [20, 19]. Using these cuts, we obtain rates $\Gamma(b \to c\bar{u}d\gamma)$ between 3×10^{-18} GeV and 5×10^{-18} GeV, which translates into the branching ratio for the inclusive process:

$$\begin{aligned} B(b \to X_c\gamma) &= \frac{\Gamma(b \to c\bar{u}d\gamma)_{th}}{\Gamma(b \to ce^-\nu)_{th}} B(B^+ \to X_c e^+\nu)_{exp} \\ &\sim (7-11) \times 10^{-6}. \end{aligned} \tag{4.1}$$

To obtain this number, we used $V_{cb} = 0.0413$ [25], $B(B^+ \to X_c e^+\nu)_{exp} = (11.15 \pm 0.26 \pm 0.41)\%$ [26] and quark mass values $m_b = 4.8$ GeV, $m_c = 1.5$ GeV which are the ones used in the theory estimates of $b \to X_s\gamma\gamma$. In Figure 4.1 we show the photon energy spectrum for the case of $\theta_{min} = 5^\circ$. We observe that the characteristic bremsstrahlung spectrum falls rapidly with the photon energy and, for this reason, $B(b \to X_c\gamma)$ is much smaller than the penguin mode $B(b \to X_s\gamma) = (3.3 \pm 0.4) \times 10^{-4}$ [25] in this energy range.

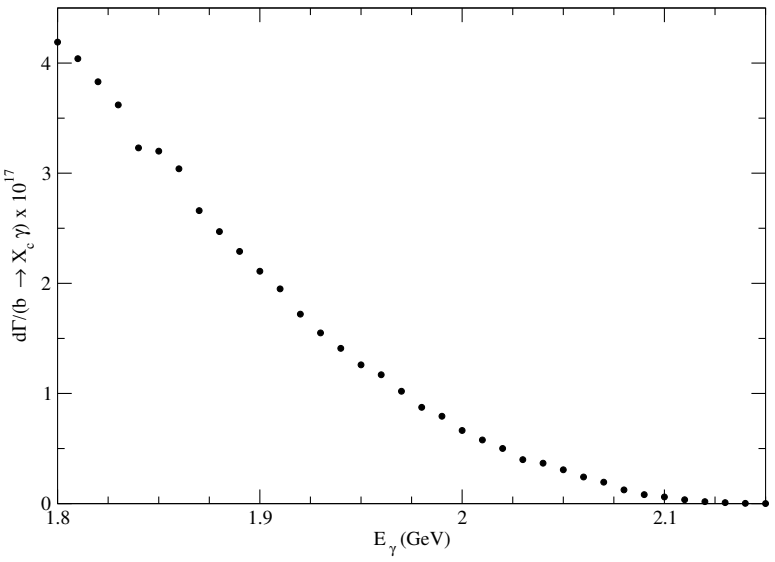

Figure 4.1 Photon energy spectrum in $b \to X_c\gamma$ with $\theta_{min} = 5^\circ$.

Next we consider the double radiative mode $B \to X_c\gamma\gamma$ in a similar way. We wish to

compare it to the penguin process $B \to X_s\gamma\gamma$ which has not been observed. We use instead the theoretical calculation of Reina *et. al.* [20, 19] which finds $B(B \to X_s\gamma\gamma) \sim 3.7 \times 10^{-7}$ (including Lowest Order (LO) QCD corrections and using the quark masses mentioned above). In order to isolate two hard photons, they also require that the energy of each photon be larger than 0.1 GeV, that the photon pair invariant mass be larger than $0.1m_b$, and that the photons be separated from each other and from final state quarks by at least 20°. They find a spectrum that is sharply peaked at low $M_{\gamma\gamma}$ invariant mass.

For our calculation we estimate $B \to X_c\gamma\gamma$ from the leading tree-level contribution $b \to c\bar{u}d\gamma\gamma$. With the same cuts used by Ref. [20, 19] for $B \to X_s\gamma\gamma$ we obtain $\Gamma(b \to c\bar{u}d\gamma\gamma) = 1.9 \times 10^{-18}$ GeV; and this goes up to 3.2×10^{-18} GeV if the angular cuts are relaxed to 10°. Proceeding as in Eq. (4.1), we arrive at

$$B(B \to X_c\gamma\gamma) \sim (4.2 - 7.2) \times 10^{-6}. \tag{4.2}$$

In Figure 4.2 we show the two photon invariant mass distribution.

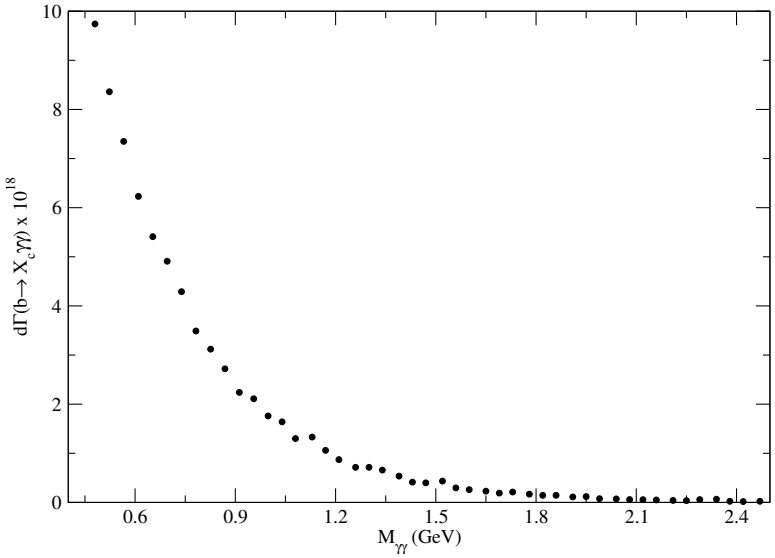

Figure 4.2 $M^2_{\gamma\gamma}$ distribution for the process $b \to X_c\gamma\gamma$ with the cuts described in the text.

Once again we see a spectrum that is strongly peaked at low invariant mass. Comparing

our results to those of Ref. [20, 19], it is clear that $B \to X_c\gamma\gamma$ can be a significant background to $B \to X_s\gamma\gamma$. Notice that the total rate for the double radiative decay mode is comparable to that for $b \to X_c\gamma$. This, of course, is due to the much tighter photon energy cuts imposed in that case.

4.1.3 Exclusive Modes and HQET

In this section we collect the ingredients necessary to calculate the amplitudes for the exclusive modes guided by heavy quark effective theory. We will extend the ideas presented in Chapter 2, shaping them suitably for our current application.

A.Radiative decays of heavy mesons

Following our discussion in Chapter 2, the strong interactions involving the heavy meson $(0^-, 1^-)$ doublet (the lightest pseudoscalar and vector mesons containing one heavy quark) and light pseudo-scalars are described by the effective Lagrangian (we drop the subscript v that indicates the velocity of the heavy meson to simplify the notation) [27, 28, 29]

$$\mathcal{L} = -iTr(\bar{H}_a^{(Q)} v \cdot D_{ba} H_b^{(Q)}) + gTr(\bar{H}_a^{(Q)} H_b^{(Q)} \gamma_\nu \gamma_5 A_{ba}^\nu). \tag{4.3}$$

In Eq. (4.3) we use the standard notation in which

- The heavy pseudoscalar and vector meson fields with heavy quark Q and light anti-quark $\bar{q}_a$ are destroyed and created by the field $H_a^{(Q)}$ and its Hermitian conjugate. They are given by
$$H_a^{(Q)} = \frac{1+\not{v}}{2}\left(P_{a\mu}^{(Q)\star}\gamma^\mu - P_a^{(Q)}\gamma_5\right) \tag{4.4}$$
which transforms under chiral symmetry as $H_a^{(Q)} \to H_b^{(Q)} U_{ba}^\dagger$. The Hermitian conjugate matrix $\bar{H}_a^{(Q)} = \gamma_0 H_a^{(Q)\dagger}\gamma_0$.

- Mesons containing heavy anti-quarks $\bar{Q}$ and light quarks q_a are destroyed and created

by the fields

$$\begin{aligned} H_a^{(\bar{Q})} &= (P_{a\mu}^{(\bar{Q})\star}\gamma^\mu - P_a^{(\bar{Q})}\gamma_5)\frac{1-\not{v}}{2} \\ \bar{H}_a^{(\bar{Q})} &= \gamma_0 H_a^{(\bar{Q})\dagger}\gamma_0. \end{aligned} \tag{4.5}$$

- As usual, the pseudo-Goldstone boson octet, ϕ is incorporated into a 3×3 unitary matrix $\Sigma = \exp(2i\phi/f_\pi)$ which transforms under chiral symmetry as $\Sigma \to L\Sigma R^\dagger$. In Eq. (4.3) they enter through the matrix ξ where $\Sigma = \xi^2$ and the transformation properties of ξ under chiral symmetry $\xi \to L\xi U^\dagger = U\xi R^\dagger$ define the matrix U. The charges of the light quarks appear through the diagonal matrix $\mathcal{Q}$ with entries $2/3, -1/3, -1/3$.

- The chiral covariant derivative and axial current in Eq. (4.3) are given by

$$\begin{aligned} D_{ab}^\mu &= \delta_{ab}\partial^\mu - V_{ab}^\mu = \delta_{ab}\partial^\mu - \frac{1}{2}(\xi^\dagger\partial^\mu\xi + \xi\partial^\mu\xi^\dagger)_{ab} \\ A_{ab}^\mu &= \frac{i}{2}(\xi^\dagger\partial^\mu\xi - \xi\partial^\mu\xi^\dagger)_{ab}. \end{aligned} \tag{4.6}$$

The leading order electromagnetic coupling is obtained from Eq. (4.3) by minimal substitution. However, the couplings arising from this procedure (for charged B and D mesons) do not contribute to the processes $B \to D\gamma$ or $B \to D\gamma\gamma$ as can be seen by explicit computation. The lowest order electromagnetic coupling that will contribute to these processes is the transition magnetic moment [30, 31, 32, 29]. For mesons containing a heavy quark, it can be written as

$$\mathcal{L}_{em} = -\frac{ee_Q\mu_a^{(h)}}{4}Tr(\bar{H}_a^{(Q)}\sigma_{\mu\nu}H_a^{(Q)})F^{\mu\nu} - \frac{e\mu_a^{(l)}}{4}Tr(\bar{H}_a^{(Q)}H_b^{(Q)}\sigma_{\mu\nu}\mathcal{Q}^{ab}F^{\mu\nu}). \tag{4.7}$$

The coupling consists of two terms corresponding to the decomposition of the electromagnetic current into heavy and light quark parts,

$$\mu_a = \mu_a^{(h)} + \mu_a^{(l)} = \frac{e_Q}{\Lambda_Q} + \frac{e_a}{\Lambda_a}, \tag{4.8}$$

where e_a is the charge of the light-quark. The heavy quark contribution at leading order in the $1/m_Q$ expansion is given by $\Lambda_Q = m_Q$ [33, 34]. The light quark contribution in the SU(3) symmetry limit is usually called $\Lambda_a^{-1} = \beta$ [29]. This constant has been estimated in vector meson dominance models [35] as well as in chiral quark models [36] (along with SU(3)

breaking corrections). The leading SU(3) violations have also been calculated [31]. More generally, the heavy quark contribution when the mesons have different velocity is modified to $\mu_a^{(h)} = e_Q \xi(\omega)/m_Q$ where $\omega = v \cdot v'$ and $\xi(\omega)$ is the Isgur and Wise function.

Eq. (4.7) generates the following amplitudes,

$$\begin{aligned} \mathcal{M}(D^\star(\eta) \to D\gamma(q,\epsilon)) &= -ie\mu_D \epsilon^{\mu\nu\alpha\beta} \epsilon^\star_\mu \eta_\nu q_\alpha v_\beta, \\ \mathcal{M}(D^\star(\eta_1) \to D^\star(\eta_2)\gamma(q,\epsilon)) &= e\mu_{D\star} \left(q \cdot \eta_1 \epsilon^\star \cdot \eta_2^\star - q \cdot \eta_2^\star \epsilon^\star \cdot \eta_1 \right), \end{aligned} \tag{4.9}$$

where we have defined $\mu_{D\star} \equiv (\mu_a^{D(h)} - \mu_a^{D(l)})$. Analogous relations with $\mu_{D,D\star} \to \mu_{B,B\star}$ then hold for the B system. In the heavy quark and SU(3) limits, the magnetic moments consist only of the light quark contribution given by $\mu_a = e_a \beta$. For our numerical estimates we will use the leading magnetic moments as well as the magnetic moments in three models tabulated in Ref. [32]: "χLM" a chiral loop model; "VMD" a vector meson dominance model; and "RQM" a relativistic quark model.

The magnetic moments from Eq. (4.7) are defined for on-shell transitions between a vector and a pseudo-scalar of the same mass. In our calculations one of the mesons will be off its mass shell and the corresponding form-factors should be evaluated at $k^2 \sim -\delta m^2$ for the single radiative decay modes: $e\mu \equiv g_M(0) \to e\mu g_M(-\delta m^2)$ where $\delta m \equiv m_b - m_c$. On general grounds one expects the form factor to change over a characteristic scale Λ_{QCD}, so there is large uncertainty associated with the use of the on-shell form factors. Formally, the results we obtain correspond to the so called generally low velocity (GL) limit in which [21]

$$\delta m \sim \Lambda_{QCD} \ll m_b. \tag{4.10}$$

Alternatively, one can model the momentum dependence of the form factors as was done in Ref. [22] for the neutral modes. We will not include a momentum dependence of the form factors in our estimates, but instead introduce two additional effects. First, we will keep certain terms that are formally of order $\delta m/m_b$ arising from spin one propagators as described later on. We will also consider additional heavy meson intermediate states; the positive parity P-waves of the system $Q\bar{q}$. However, we will neglect higher total spin resonances.

The positive parity states that we include are predicted by HQET to lie in two distinct multiplets: $(0^+,1^+)$=(B_0,B_1) and $(1^+,2^+)$=$(\tilde{B_1},B_2)$. Generically, we will refer to them as $B^{\star\star}$ and will discuss the case of B mesons for definiteness, with corresponding results for D mesons also used in our calculation. The velocity dependent fields are introduced in a manner similar to the field H in Eq. (4.4) [37, 38]

$$\begin{aligned} S &= \frac{1}{2}(1+\not{v})[\not{B}_1\gamma_5 - B_0] \\ T^\mu &= \frac{1}{2}(1+\not{v})\left[B_2^{\mu\nu}\gamma_\nu - \sqrt{3/2}\tilde{B}_{1\nu}\gamma_5(g^{\mu\nu}-\frac{1}{3}\gamma^\nu(\gamma^\mu - v^\mu))\right] \end{aligned} \tag{4.11}$$

The electromagnetic transitions between a member of these doublets and a member of the $(0^-,1^-)$ doublet have also been discussed in the literature. Analogously to Eq. (4.7), the couplings receive contributions from the heavy and light quark currents.

The heavy quark contribution to the $(1^+,2^+)$ to $(0^-,1^-)$ transition in the charm case can be found in [39]. A simple way to reproduce those results consists of using the matrix elements for $< B^{\star\star}|V^\mu|B >$ obtained by Isgur and Wise [40] to match the effective Lagrangian $\mathcal{L} \sim Tr\left(\bar{H}_i\gamma^\beta T_j^\alpha \mathcal{Q}_{ij}F_{\alpha\beta}\right)$. Similarly, one can start from the Isgur and Wise results and impose gauge invariance for the kinematic conditions we consider to obtain the heavy quark contribution to the $(0^+,1^+)$ to $(0^-,1^-)$ transition.

The light quark contributions can be determined at leading order in chiral perturbation theory in terms of two unknown constants,

$$\mathcal{L} = -\frac{ie}{\Lambda'_{3/2}}Tr\left(\bar{H}_i T_j^\alpha \gamma^\beta \mathcal{Q}_{ij}F_{\alpha\beta}\right) - \frac{e}{4\Lambda'_{1/2}}Tr\left(\bar{H}_i S_j \sigma_{\mu\nu}\mathcal{Q}_{ij}F^{\mu\nu}\right) + \text{ h. c.} \tag{4.12}$$

Combining the heavy and light quark contributions for the T doublet leads to the amplitudes (we include only those that do not vanish at leading order in the $1/m_Q$ and chiral expansions)

$$\begin{aligned} \mathcal{M}(B_2(v,\epsilon_2)\to B^\star(v,\epsilon_V)\gamma(q,\epsilon)) &= -2\sqrt{3}e\mu_B^T\left(\epsilon_2^{\alpha\beta}q_\alpha\epsilon^\star_{V\beta}\epsilon^\star\cdot v - \epsilon_2^{\mu\beta}\epsilon^\star_{V\beta}\epsilon^\star_\mu q\cdot v\right) \\ \mathcal{M}(\tilde{B}_1(v,\epsilon_1)\to B^\star(v,\epsilon_V)\gamma(q,\epsilon)) &= i\sqrt{2}e\mu_B^T\epsilon^{\mu\nu\alpha\beta}q_\mu\epsilon^\star_\nu\epsilon^\star_{V\alpha}\epsilon_{1\beta} \\ \mathcal{M}(\tilde{B}_1(v,\epsilon_1)\to B(v)\gamma(q,\epsilon)) &= 2\sqrt{2}e\mu_B^T\left(q\cdot\epsilon_1 v\cdot\epsilon^\star - q\cdot v\epsilon_1\cdot\epsilon^\star\right). \end{aligned} \tag{4.13}$$

Similarly for the S doublet, we obtain

$$\begin{aligned}
\mathcal{M}(B_1(v,\epsilon_1) \to B^\star(v,\epsilon_V)\gamma(q,\epsilon)) &= -ie\mu_B^S \epsilon^{\mu\nu\alpha\beta} q_\mu \epsilon^\star_\nu \epsilon^\star_{V\alpha} \epsilon_{1\beta} \\
\mathcal{M}(B_1(v,\epsilon_1) \to B(v)\gamma(q,\epsilon)) &= e\mu_B^S \left(q\cdot\epsilon_1 v\cdot\epsilon^\star - q\cdot v\epsilon_1\cdot\epsilon^\star\right) \\
\mathcal{M}(B_0(v) \to B^\star(v,\epsilon_V)\gamma(q,\epsilon)) &= e\mu_B^S \left(q\cdot\epsilon^\star_V v\cdot\epsilon^\star - q\cdot v\epsilon^\star_V\cdot\epsilon^\star\right). \qquad (4.14)
\end{aligned}$$

Corresponding expressions for charm are obtained with the obvious replacements $\mu_B^{T,S} \to \mu_D^{T,S}$. For bottom, these effective coupling constants are

$$\mu_B^T \equiv \left(\frac{e_b \tau^{3/2}(1)}{m_b} + \frac{e_a}{\Lambda'_{3/2}}\right), \qquad \mu_B^S \equiv \left(\frac{2e_b \tau^{1/2}(1)}{m_b} + \frac{e_a}{\Lambda'_{1/2}}\right). \qquad (4.15)$$

For the light quark contributions, $\Lambda'_{3/2}$ corresponds to $\sqrt{3}/(f-f')$ of Ref. [39]. Using their estimate for the D system, we take $\Lambda'_{3/2} \sim (2.75-3.5)$ GeV. Similarly, $\Lambda'_{1/2}$ corresponds to Λ' of Ref. [41] where it is estimated that $\Lambda'_{1/2} \sim 1.25$ GeV. For the heavy quark contributions we have used the Isgur-Wise functions $\tau^{1/2,3/2}$ estimated in Ref. [42] to be $\tau^{1/2,3/2}(1) \sim 0.24$ ($\xi^{3/2}$ of Ref. [39] corresponds to $\sqrt{3}\tau^{3/2}$) .

Finally, we will also need both $(0^+,1^+)$ to $(0^+,1^+)$ and $(0^+,1^+)$ to $(1^+,2^+)$ electromagnetic transitions. The former receives heavy and light quark contributions, whereas the latter only receives light quark contributions at order $1/m_Q$. They can be obtained from the Lagrangian

$$\mathcal{L} = -\frac{ee_Q}{4m_Q} Tr(\bar{S}_a \sigma_{\mu\nu} S_a) F^{\mu\nu} - \frac{e}{4\tilde{\Lambda}_{1/2}} Tr(\bar{S}_a S_b \sigma_{\mu\nu} \mathcal{Q}^{ab} F^{\mu\nu}) - \frac{ie}{\tilde{\Lambda}_{3/2}} Tr\left(\bar{S}_i T^\alpha_j \gamma^\beta \mathcal{Q}_{ij} F_{\alpha\beta}\right). \quad (4.16)$$

The new constants $\tilde{\Lambda}_{1/2,3/2}$ are not known. For our numerical estimates, we use $\tilde{\Lambda}_{1/2} \sim \Lambda_a$ and $\tilde{\Lambda}_{3/2} \sim \Lambda_{3/2}$. With this choice, the magnetic transitions within the S multiplet are the same as those between members of the H multiplet; for charm, for example, one has

$$\begin{aligned}
\mathcal{M}(D_1(\eta) \to D_0\gamma(q,\epsilon)) &= -ie\mu_D \epsilon^{\mu\nu\alpha\beta} \epsilon^\star_\mu \eta_\nu q_\alpha v_\beta, \\
\mathcal{M}(D_1(\eta_1) \to D_1(\eta_2)\gamma(q,\epsilon)) &= e\mu_{D\star} \left(q\cdot\eta_1 \epsilon^\star\cdot\eta_2^\star - q\cdot\eta_2^\star \epsilon^\star\cdot\eta_1\right), \qquad (4.17)
\end{aligned}$$

and the corresponding expressions for the bottom. The $(0^+,1^+)$ to $(1^+,2^+)$ vertices for bottom

are

$$\begin{aligned}
\mathcal{M}(B_2(v,\epsilon_2)\to B_1(v,\epsilon_V)\gamma(q,\epsilon)) &= i2e\mu_B^{TS}\left(\epsilon^{\alpha\mu\nu\gamma}\epsilon_2^{\alpha\beta}q_\beta v_\mu\epsilon^\star_\nu\epsilon^\star_{1\gamma}+\epsilon^{\alpha\mu\nu\gamma}\epsilon_2^{\alpha\beta}q_\mu v_\nu\epsilon^\star_\beta\epsilon^\star_{1\gamma}\right)\\
\mathcal{M}(\tilde{B}_1(v,\epsilon_i)\to B_1(v,\epsilon_f)\gamma(q,\epsilon)) &= -e\mu_B^{TS}\sqrt{\frac{2}{3}}\left(q\cdot\epsilon_i\epsilon^\star\cdot\epsilon^\star_f-q\cdot\epsilon^\star_f\epsilon^\star\cdot\epsilon_i\right)\\
\mathcal{M}(\tilde{B}_1(v,\epsilon_1)\to B_0(v)\gamma(q,\epsilon)) &= i2e\mu_B^{TS}\sqrt{\frac{2}{3}}\epsilon^{\alpha\mu\nu\gamma}q_\alpha v_\mu\epsilon^\star_\nu\epsilon_{1\gamma},
\end{aligned}\tag{4.18}$$

and corresponding expressions for charm. We have defined

$$\mu_B^{TS}\equiv\frac{e_a}{\tilde{\Lambda}_{3/2}}.\tag{4.19}$$

B.Weak transitions

Within the standard model, the effective weak Hamiltonian responsible for the $\Delta B=1$ transitions at tree-level is (with $d_i=d$ or s)

$$\mathcal{H}=\frac{G_F}{\sqrt{2}}\left[V^\star_{cb}V_{ud_i}\left(C_1Q_1^n+C_2Q_2^n\right)+V^\star_{ub}V_{cd_i}\left(C_1Q_1^c+C_2Q_2^c\right)\right]+\text{ h. c.}\tag{4.20}$$

where the neutral modes $B^0\to\bar{D}^0(\bar{D}^{0\star})$ are mediated by $Q_1^n=(\bar{b}d_i)_{V-A}(\bar{u}c)_{V-A}$ and $Q_2^n=(\bar{b}c)_{V-A}(\bar{u}d_i)_{V-A}$; and the charged modes $B^+\to D^+(D^{+\star})$ are mediated by $Q_1^c=(\bar{b}d_i)_{V-A}(\bar{c}u)_{V-A}$ and $Q_2^c=(\bar{b}u)_{V-A}(\bar{c}d_i)_{V-A}$ respectively. [1] Our first task is to write the operators corresponding to Eq. (4.20) in the heavy quark effective theory.

For the charged modes, this was already done in Ref. [21]. The operators $Q^c_{1,2}$ can be written in terms of their heavy (A,B) and light (a,b) degrees of freedom in the more general form

$$\mathcal{O}^{ab\bar{A}B}=\bar{A}\gamma_\mu(1-\gamma_5)a\bar{B}\gamma^\mu(1-\gamma_5)b.\tag{4.21}$$

As pointed out by Grinstein and Lebed [21], this form illustrates there are symmetry relations that would allow one to extract the coupling of this effective Lagrangian from the measurements of $B-\bar{B}$ mixing.

For the charged transitions, this operator has to destroy a heavy quark and a light quark of flavors $(\bar{A},a)=(\bar{b},u)$ and create a heavy quark and a light quark of flavors $(\bar{B},b)=(c,\bar{d}_i)$.

[1] For our numerical estimates, we will use the tree-level coefficients $C_1=0$, $C_2=1$.

This operator transforms as a $(6_L, 1_R)$ under the chiral symmetry and, as shown in Ref. [43], Eq. (4.21) matches in the symmetry limit of the effective theory onto

$$\mathcal{O}^{ab\bar{A}B} = \beta_W Tr\left[(\xi_{ac}H_c^{(\bar{A})})\gamma_\mu(1-\gamma_5)\right] Tr\left[(\xi_{bd}\bar{H}_d^{(B)})\gamma^\mu(1-\gamma_5)\right] \tag{4.22}$$

As pointed out in Ref. [21], this same operator with $(\bar{A}, a) = (\bar{b}, d)$ and $(\bar{B}, b) = (b, \bar{d})$ is responsible for $B - \bar{B}$ mixing; so that, in principle, the coefficient β_W can be extracted from experiment (for this case there is an additional color factor of 8/3). This heavy quark symmetry relation is valid in the GL limit where $m_B - m_D << \Lambda_{QCD}$ and the four-velocity of the B and $D^\star$ mesons is the same. For our numerical estimates, we will use

$$\beta_W = \frac{1}{4} f_B f_D \sqrt{m_B m_D} \sim (0.034 \pm 0.009)\ \text{GeV}^3, \tag{4.23}$$

where we used the decay constants $f_B = (191 \pm 27)\ MeV$ [44] and $f_D = (225^{+11}_{-13} \pm 21)\ MeV$ [45]. This last one is in good agreement with the recent CLEO measurement $f_D = (222.6 \pm 16.7^{+2.8}_{-3.4}\ MeV$ [46].

For the radiative decay modes that we consider in this chapter, there are no light pseudoscalars involved so we set $\xi = 1$ in Eq. (4.22) to obtain the matrix elements:

$$\begin{aligned}
< D_v^*(\eta)|\mathcal{O}^{ab\bar{A}B}|B_v^*(\eta^{'}) > &= 4\beta_W \eta\cdot\eta'^\star, \\
< D_v|\mathcal{O}^{ab\bar{A}B}|B_v > &= 4\beta_W, \\
< D_v^*(\eta)|\mathcal{O}^{ab\bar{A}B}|B_v > &= -4\beta_W \eta\cdot v, \\
< B_v^*(\eta)|\mathcal{O}^{ab\bar{A}B}|D_v > &= -4\beta_W \eta\cdot v,
\end{aligned} \tag{4.24}$$

where η, η' are the vector meson polarization vectors and v the B meson velocity. The last two terms vanish when the condition $v\cdot\eta = 0$ is used. We retain them because we will use them beyond leading order in the heavy quark expansion later on, as they contribute known terms of order $(m_b - m_c)/m_c$.

The neutral modes involving the weak transition $B_i^0 \to \bar{D}^0$ are mediated by the operators $Q_{1,2}^n$ in Eq. (4.20). To construct a matching operator in the effective theory, we notice that they transform as $(8_L, 1_R)$ under the chiral symmetry. We also need to extract the part of

the operators responsible for destroying a heavy anti-quark (of flavor b) and creating a heavy anti-quark (of flavor c). A possible match for Q_2^n of the current-current form is

$$\mathcal{O} = Tr\left[\bar{H}_a^{(\bar{c})}\gamma_\mu(1-\gamma_5)H_f^{(\bar{b})}\right]\left(\xi^\dagger\partial^\mu\xi\right)_{fa}. \tag{4.25}$$

However, this operator does not contribute to the processes without light pseudo-scalars that we are discussing.

A possible operator that does contributes to $B_i^0 \to \bar{D}^0$ transitions at tree level is of the form

$$\mathcal{O} \;=\; \beta'_W Tr\left[(\xi_{uj}\bar{H}_j^{(\bar{c})})\gamma_\mu(1-\gamma_5)\right] Tr\left[(\xi_{dk}H_k^{(\bar{b})})\gamma^\mu(1-\gamma_5)\right]. \tag{4.26}$$

This operator leads to matrix elements analogous to those in Eq.(4.24) with $\beta_W \to \beta'_W$. As was the case with the charged modes, there are other possible matches; but they lead to the same result [43]. We have not found a way to determine β'_W from symmetry relations and must resort to the factorization model

$$\beta'_W = \frac{1}{12} f_B f_D \sqrt{m_B m_D} = \frac{\beta_W}{N_c}. \tag{4.27}$$

An additional factor of $1/N_c = 1/3$ relative to β_W occurs because the contribution of Q_2^n to these weak transitions in factorization requires a Fierz transformation and color rearrangement.

For weak transitions involving the positive parity states, $B \to D^{\star\star}$, we have two new operators for the S doublet. The operators Q_2^c and Q_2^n in Eq. (4.20) for the charged and neutral modes can be matched in the factorization approximation into the operators

$$\begin{aligned} Q_2^c &\to -\beta_W Tr\left[(\xi_{uj}\bar{H}_j^{(\bar{c})})\gamma_\mu(1-\gamma_5)\right] Tr\left[\gamma^\mu(1-\gamma_5)(S_j^{(\bar{b})}\xi_{jd}^\dagger)\right] \\ Q_2^n &\to -\beta'_W Tr\left[(\xi_{uj}\bar{H}_j^{(\bar{c})})\gamma_\mu(1-\gamma_5)\right] Tr\left[\gamma^\mu(1-\gamma_5)(S_j^{(\bar{b})}\xi_{jd}^\dagger)\right] \end{aligned} \tag{4.28}$$

for transitions of the form $(0^-, 1^-)_b \to (0^+, 1^+)_c$. The extra minus sign is chosen so that the coefficients β_W and β'_W are the same as those in Eqs. (4.23) and (4.27) if we take the decay constants and masses of the two doublets to be the same. This is approximately true for the decay constants in the analysis of Ref. [42] based on QCD sum rules.

The $T = (1^+, 2^+)$ multiplet does not participate in the weak transitions in this approximation since its decay constant vanishes [47].

The matrix elements obtained from Eq. (4.28) (and corresponding ones for $(0^-, 1^-)_b \to (0^+, 1^+)_c$ transitions) that do not involve light mesons are then

$$\begin{aligned} < D_v^*(\eta)|Q_2^c|B_{1v}(\eta^{'}) > &= -4\beta_W \eta \cdot \eta^{'}, \\ < D_v|Q_2^c|B_{0v} > &= -4\beta_W, \\ < D_v^*(\eta)|Q_2^c|B_{0v} > &= 4\beta_W \eta \cdot v, \\ < D_v|Q_2^c|B_{1v}(\eta') > &= 4\beta_W \eta^\star \cdot v, \end{aligned} \tag{4.29}$$

and the same expressions with $\beta_W \to \beta'_W$ for the neutral modes. Finally, we will need weak transitions from $(0^+, 1^+)_b \to (0^+, 1^+)_c$. They follow from an effective Lagrangian like the one in Eq. (4.22) with S fields replacing H fields and produce matrix elements with the same sign as those in Eq. (4.24).

4.1.4 $\mathbf{B \to D^\star \gamma}$

We now turn our attention to the single radiative decay for exclusive channels and begin with the kinematics of this decay.

Kinematics

The most general amplitude for decays of the form $M \to V(\eta)\gamma(q, \epsilon)$ consistent with electromagnetic gauge invariance can be written in terms of two form factors. Labeling the momentum of the initial state M with its four velocity in its rest frame, $p = M_M v$, and denoting the polarization of V, γ by η, ϵ respectively

$$\mathcal{M}(M \to V\gamma) = \epsilon^{\star\mu} \left[iF_M \epsilon_{\mu\nu\alpha\beta} v^\nu q^\alpha \eta^{\star\beta} + F_E \left(q \cdot \eta^\star v_\mu - q \cdot v \eta^\star_\mu \right) \right]. \tag{4.30}$$

Summing over the photon and vector meson polarizations, the partial decay rate is given by

$$\Gamma(M \to V\gamma) = \frac{E_\gamma^3}{4\pi M_M^2} \left(|F_M|^2 + |F_E|^2 \right). \tag{4.31}$$

For the heavy meson formalism in which the meson fields are normalized as

$$< M(v', k')|M(v, k) >= 2v^0 \delta_{vv'} (2\pi)^3 \delta^3(\vec{k} - \vec{k}'), \tag{4.32}$$

the decay rate becomes instead

$$\Gamma(M \to V\gamma) = \frac{E_\gamma^3}{4\pi}\frac{E_V}{M_M}\left(|F_M|^2 + |F_E|^2\right), \tag{4.33}$$

where we have used exact kinematics, otherwise in the heavy quark symmetry limit $E_V = M_M$ as well.

Calculation

Both the charged $B^+ \to D^{\star+}\gamma$ and neutral $B^0 \to \bar{D}^{\star 0}\gamma$ modes have been estimated before. We begin with the charged mode discussion of Ref. [21]. With the ingredients introduced in the previous section, it is straight-forward to compute the amplitude from the two diagrams in Figure 4.3.

Figure 4.3 Pole diagrams responsible for $B \to D^\star\gamma$ at leading order in heavy quark and chiral theories.

For the process $B_v^+ \to D_{vi}^{\star+}(\eta)\gamma(q,\epsilon)$, we find a leading order amplitude containing only a magnetic form factor: $F_M = (F_M)_{LO} r_\mu^+$ with

$$\begin{aligned}(F_M)_{LO}\,(B^+ \to D_i^{\star+}\gamma) &\equiv \sqrt{2}G_F V_{ub}^\star V_{cd_i}\beta_W e\left(\frac{\mu_{D^+}}{m_{B^+} - m_{D^{\star+}}}\right)\\ r_\mu^+ &\equiv \left(1 + \frac{\mu_{B^+}}{\mu_{D^+}}\frac{2m_{B^+}}{m_{B^+} + m_{D^{\star+}}}\right).\end{aligned} \tag{4.34}$$

Similarly, for the neutral modes $F_M = (F_M)_{LO} r_\mu^0$ with

$$\begin{aligned}(F_M)_{LO}(B_i^0 \to \bar{D}^{\star 0}\gamma) &= \sqrt{2}G_F V_{cb}^\star V_{ud_i}\beta'_W e\left(\frac{\mu_{D^0}}{m_{B^0} - m_{D^{\star 0}}}\right)\\ r_\mu^0 &\equiv \left(1 + \frac{\mu_{B^0}}{\mu_{D^0}}\frac{2m_{B^0}}{m_{B^0} + m_{D^{\star 0}}}\right).\end{aligned} \tag{4.35}$$

Using the leading order magnetic moments and the GL limit to evaluate these amplitudes yields $r_\mu^+ = -1$, $r_\mu^0 = 1/2$. Combining this with exact kinematics for the phase space, one

obtains [2]

$$\begin{aligned}\Gamma(B^+ \to D_i^{\star +}\gamma) &= \frac{G_F^2}{36}\,|V_{ub}^\star V_{cd_i}|^2\,\alpha\left(\beta_W\beta r_\mu^+\right)^2\,\frac{m_D^\star}{m_B^4}(m_B - m_{D^\star})(m_B + m_{D^\star})^3 \\ \Gamma(B_i^0 \to \bar{D}^{\star 0}\gamma) &= \frac{G_F^2}{9}\,|V_{cb}^\star V_{ud_i}|^2\,\alpha\left(\beta_W'\beta r_\mu^0\right)^2\,\frac{m_D^\star}{m_B^4}(m_B - m_{D^\star})(m_B + m_{D^\star})^3. \quad (4.36)\end{aligned}$$

We wish to emphasize that these results exhibit a high sensitivity to non-leading contributions to the magnetic moments. With exact kinematics (i.e. taking $m_B \neq m_D$) and using the three models for magnetic moments in Table 8 of Ref. [32], one finds

$$\begin{aligned}\chi - \text{loop}: &\qquad r_\mu^+ = -6.3, \quad r_\mu^0 = 0.28, \\ VMD: &\qquad r_\mu^+ = -4.7, \quad r_\mu^0 = 0.38, \\ RQM: &\qquad r_\mu^+ = -4.7, \quad r_\mu^0 = 0.50. \quad (4.37)\end{aligned}$$

These numbers lead to predicted rates that are larger than the leading order prediction by factors between 16 and 36 for the charged modes. For the neutral modes the effect is more modest. Allowing the magnetic moments to vary in the ranges predicted by these models results in the rates

$$\begin{aligned}0.7\times 10^{-7} \lesssim &\quad B(B^0 \to \bar{D}^{\star 0}\gamma) \quad \lesssim 4.6\times 10^{-7}, \\ 1.5\times 10^{-8} \lesssim &\quad B(B_s^0 \to \bar{D}^{\star 0}\gamma) \quad \lesssim 3.0\times 10^{-8}, \\ 3.6\times 10^{-9} \lesssim &\quad B(B^+ \to D^{\star +}\gamma) \quad \lesssim 4.9\times 10^{-9}, \\ 0.7\times 10^{-7} \lesssim &\quad B(B^+ \to D_s^{\star +}\gamma) \quad \lesssim 1.0\times 10^{-7}. \quad (4.38)\end{aligned}$$

There is also a significant uncertainty from the use of $g_M(0)$ for the electromagnetic transitions, when in these reactions one should use $g_M(k^2 \sim -E_\gamma^2 \sim -(2\text{ GeV})^2)$.

We now consider two types of higher order corrections to these results that are counterpart to additional terms present in the pole model calculation of the neutral modes in Ref. [48, 22]. They correspond to the diagrams shown in Figure 4.4.

The first diagram (Figure 4.4a) contributes beyond leading order in the heavy quark symmetry when we allow for $m_B \neq m_D$. It generates an electric amplitude from corrections to the

[2] Our rate for the charged process is a factor of 9 smaller than the result obtained in Ref. [21] which corresponds to this limit.

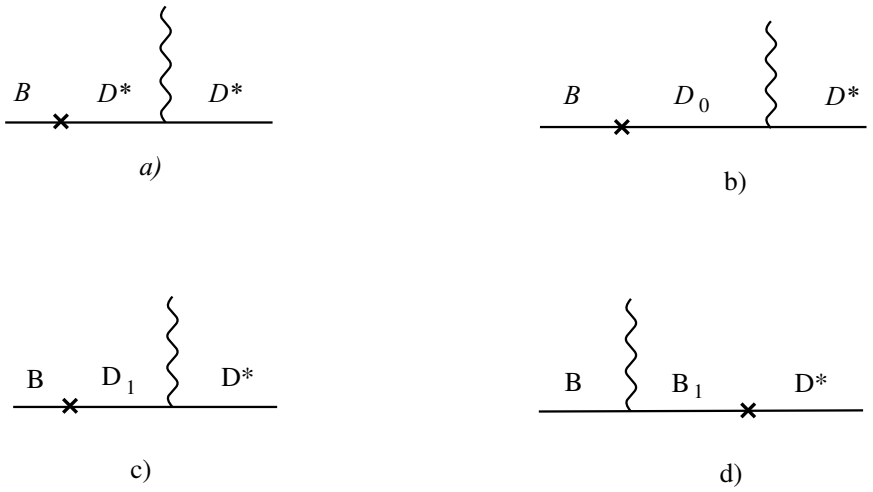

Figure 4.4 Non-leading contributions to $B \to D^\star\gamma$: a)$P^* - P$ weak transitions that vanish in the $m_B = m_D$ limit; b-d) additional pole contributions from positive parity states.

leading order 1^- propagator fixed by reparametrization invariance

$$F_E(B^+ \to D_i^{\star +}\gamma) = -\sqrt{2}G_F V_{ub}^\star V_{cd_i}\beta_W e\left(\frac{\mu_{D^{\star +}}}{m_{B^+} - m_{D^{\star +}}}\right)\left(1 - \frac{m_B^2}{m_D^2}\right). \tag{4.39}$$

The next two diagrams (Figure 4.4b,c) involve an intermediate positive parity state that can be either the D_0 or the D_1 from the S multiplet. They generate an electric and magnetic form factor respectively that can be written as

$$\begin{aligned} F_E(B^+ \to D_i^{\star +}\gamma) &= -\sqrt{2}G_F V_{ub}^\star V_{cd_i}\beta_W e\left(\frac{\mu^S_{D^+}}{m_{B^+} - m_{D_0}}\right) \\ F_M(B^+ \to D_i^{\star +}\gamma) &= -\sqrt{2}G_F V_{ub}^\star V_{cd_i}\beta_W e\left(\frac{\mu^S_{D^+}}{m_{B^+} - m_{D_1}}\right)\left(1 - \frac{m_B^2}{m_{D_1}^2}\right). \end{aligned} \tag{4.40}$$

Finally, the last diagram (Figure 4.4d) involving an intermediate B_1 meson contributes to the electric form factor as

$$F_E(B^+ \to D_i^{\star +}\gamma) = -\sqrt{2}G_F V_{ub}^\star V_{cd_i}\beta_W e\mu^S_{B^+}\left(\frac{2m_B}{m_B^2 - m_{D^\star}^2}\right). \tag{4.41}$$

Analogous results are obtained for the neutral mode with the obvious replacement $V_{ub}^{\star}V_{cd_i}\beta_W \to V_{cb}^{\star}V_{ud_i}\beta'_W$ and magnetic moments and masses appropriate for neutral mesons. Combining all these partial results, we finally obtain

$$\begin{aligned} F_M(B^+ \to D_i^{\star +}\gamma) &= \sqrt{2}G_F V_{ub}^{\star}V_{cd_i}\beta_W e \left(\frac{\mu_{D^+}}{m_{B^+}-m_{D^{\star +}}}\right) \\ &\cdot \left(1+\frac{\mu_{B^+}}{\mu_{D^+}}\frac{2m_{B^+}}{m_{B^+}+m_{D^{\star +}}}+\frac{\mu_{D^+}^S}{\mu_{D^+}}\frac{m_B^2-m_{D_1^+}^2}{m_{D_1^+}^2}\frac{m_B-m_{D^{\star +}}}{m_B-m_{D_1^+}}\right), \\ F_E(B^+ \to D_i^{\star +}\gamma) &= -\sqrt{2}G_F V_{ub}^{\star}V_{cd_i}\beta_W e \left(\frac{\mu_{D^+}^S}{m_{B^+}-m_{D^{\star +}}}\right) \\ &\cdot \left(\frac{m_B-m_{D^{\star +}}}{m_B-m_{D_0^+}}-\frac{\mu_{D^{\star +}}}{\mu_{D^+}^S}\frac{m_B^2-m_{D^{\star +}}^2}{m_{D^{\star +}}^2}+\frac{\mu_{B^+}^S}{\mu_{D^+}^S}\frac{2m_B}{m_B+m_{D^{\star +}}}\right). \end{aligned} \tag{4.42}$$

With the range of magnetic moments provided by the three models, we find

$$\begin{aligned} 1.2\times 10^{-5} \lesssim\ & B(B^0 \to \bar{D}^{\star 0}\gamma) \lesssim 3.1\times 10^{-5}, \\ 0.7\times 10^{-6} \lesssim\ & B(B_s^0 \to \bar{D}^{\star 0}\gamma) \lesssim 1.7\times 10^{-6}, \\ 0.6\times 10^{-7} \lesssim\ & B(B^+ \to D^{\star +}\gamma) \lesssim 1.0\times 10^{-7}, \\ 0.6\times 10^{-6} \lesssim\ & B(B^+ \to D_s^{\star +}\gamma) \lesssim 1.4\times 10^{-6}. \end{aligned} \tag{4.43}$$

These ranges indicate only the uncertainty in the magnetic moments; in particular, they do not include the uncertainty in β_W or any other parameters. For comparison, Grinstein and Lebed obtained $B(B^+ \to D_s^{\star +}\gamma) = 2\times 10^{-8}$ [21] (when we correct their number for the missing factor 1/9). As mentioned before, the charge mode exhibits a large sensitivity to the value of the magnetic moments due to a partial cancellation between the two terms in Eq. (4.34). This sensitivity is milder when the additional terms are included as can be seen from the range in Eq. (4.43). Similarly, we can compare our result to that of Ref. [22], $B(\bar{B}^0 \to D^{\star 0}\gamma) = 9.2\times 10^{-7}$. Again this result has the same order of magnitude as the leading order contribution, Eq. (4.35), and the larger number in Eq. (4.43) is due to the contributions of the positive parity states. The prediction for $B(\bar{B}^0 \to D^{\star 0}\gamma)$ in Eq. (4.43) is, in fact, close to the experimental upper bound $\mathcal{B}(\bar{B}^0 \to D^{\star 0}\gamma) < 2.5\times 10^{-5}$ [49]; and part of the range is already excluded. For comparison, a recent calculation finds $\mathcal{B}(\bar{B}^0 \to D^{\star 0}\gamma) \sim 1.6\times 10^{-6}$

[50] using a different framework. Although smaller than our range in Eq. (4.43), this result is not incompatible with ours given the large uncertainty illustrated by the differences between Eqs. (4.38) and (4.43).

4.1.5 $B \to D\gamma\gamma$ and HQET

We are now in a position to estimate the $B \to D\gamma\gamma$ amplitudes and let us start with the kinematics again.

Kinematics

The amplitude for decays of the type $M \to M'\gamma\gamma$, with M, M' pseudoscalar mesons,

$$\mathcal{M}(M(p) \to M'(p_3)\gamma(k_1,\epsilon_1)\gamma(k_2,\epsilon_2)) = \epsilon^{\star\mu}(k_1)\epsilon^{\star\nu}(k_2)M_{\mu\nu}(p,k_1,k_2), \tag{4.44}$$

is well known from the kaon literature [53]. The most general decay amplitude $M_{\mu\nu}(p,k_1,k_2)$ consistent with electromagnetic gauge invariance and Bose symmetry contains four form factors. We write them here in terms of the velocity of M in its rest frame, so that $p = M_M v$ as it appears within the HQET.

$$\begin{aligned} M_{\mu\nu} &= \frac{A(z,y)}{M_M^2}\left(k_{2\mu}k_{1\nu} - g_{\mu\nu}k_1\cdot k_2\right) + i\frac{C(z,y)}{M_M^2}\epsilon_{\mu\nu\alpha\beta}k_1^\alpha k_2^\beta \\ &+ \frac{2B(z,y)}{M_M^2}\left[v\cdot k_1 v_\nu k_{2\mu} + v\cdot k_2 v_\mu k_{1\nu} - v\cdot k_1 v\cdot k_2 g_{\mu\nu} - k_1\cdot k_2 v_\mu v_\nu\right] \\ &+ i\frac{D(z,y)}{M_M^2}\left[v\cdot k_1\epsilon_{\mu\nu\alpha\beta}k_2^\alpha v^\beta + v\cdot k_2\epsilon_{\mu\nu\alpha\beta}k_1^\alpha v^\beta + (v_\mu\epsilon_{\nu\alpha\beta\gamma} + v_\nu\epsilon_{\mu\alpha\beta\gamma})k_1^\alpha k_2^\beta v^\gamma\right], \end{aligned} \tag{4.45}$$

where

$$y = \frac{v\cdot(k_1-k_2)}{M_M}, \qquad z = \frac{(k_1+k_2)^2}{M_M^2}, \qquad r = \frac{M_{M'}}{M_M}. \tag{4.46}$$

The relation between these dimensionless variables and the energy of the two photons is

$$\begin{aligned} E_1 &= \frac{1}{4}M_M((z+2y+1)-r^2) \\ E_2 &= \frac{1}{4}M_M((z-2y+1)-r^2). \end{aligned} \tag{4.47}$$

Recently, Hiller and Safir [54] have claimed in the context of $B \to K\gamma\gamma$ that there are three

additional form factors,

$$\begin{aligned} M'_{\mu\nu} &= i\frac{C^+(z,y)}{M_M^3}\left[k_1\cdot k_2\epsilon_{\mu\nu\alpha\beta}(k_1^\alpha+k_2^\beta)v^\beta+(k_{2\mu}\epsilon_{\nu\alpha\beta\gamma}+k_{1\nu}\epsilon_{\mu\alpha\beta\gamma})k_1^\alpha k_2^\beta v^\gamma\right] \\ &+ i\frac{C^-(z,y)}{M_M^3}\left[k_1\cdot k_2\epsilon_{\mu\nu\alpha\beta}(k_1^\alpha-k_2^\alpha)v^\beta-(k_{2\mu}\epsilon_{\nu\alpha\beta\gamma}-k_{1\nu}\epsilon_{\mu\alpha\beta\gamma})k_1^\alpha k_2^\beta v^\gamma\right] \\ &+ i\frac{D^-(z,y)}{M_M^2}\left[v\cdot k_1\epsilon_{\mu\nu\alpha\beta}k_2^\alpha v^\beta-v\cdot k_2\epsilon_{\mu\nu\alpha\beta}k_1^\alpha v^\beta+(v_\mu\epsilon_{\nu\alpha\beta\gamma}-v_\nu\epsilon_{\mu\alpha\beta\gamma})k_1^\alpha k_2^\beta v^\gamma\right]. \end{aligned} \tag{4.48}$$

It is well known, however, that these form factors are not independent and can be reduced to the ones in Eq. (4.45). This follows from the fact that in four dimensions there are at most four linearly independent four vectors, and this gives rise to the Schouten identity [55]. In this case all three terms in Eq. (4.49) reduce to the second form factor in Eq. (4.45) so that

$$M'_{\mu\nu}=\left(M_M y C^+(z,y)+\frac{M_M}{2}\left(1+z-r^2\right)C^-(z,y)-D^-(z,y)\right)\epsilon_{\mu\nu\alpha\beta}k_1^\alpha k_2^\beta. \tag{4.49}$$

The physical region in the dimensionless variables z and y is given by

$$0\le|y|\le\frac{1}{2}\lambda^{1/2}(1,r^2,z),\quad 0\le z\le(1-r)^2, \tag{4.50}$$

with

$$\lambda(a,b,c)=a^2+b^2+c^2-2(ab+ac+bc). \tag{4.51}$$

Note that the invariant amplitudes $A(z,y)$, $B(z,y)$ and $C(z,y)$ have to be symmetric under the interchange of k_1 and k_2 as required by Bose symmetry, while $D(z,y)$ is antisymmetric. Using the definitions (4.45), the double differential rate for unpolarized photons and conventionally normalized meson fields is given by (in the rest frame of M)

$$\begin{aligned} \frac{\partial^2\Gamma}{\partial y\partial z} &= \frac{M_M}{2^9\pi^3}\ [z^2(\ |A+B|^2+|C|^2\ ) \\ &+ \quad (\ |B|^2+|D|^2\ )\ (y^2-\frac{1}{4}\lambda(1,r^2,z))^2]. \end{aligned} \tag{4.52}$$

With HQET normalization for the meson fields and with the two photons retaining their usual normalization, Eq. (4.53) is replaced by

$$\begin{aligned} \frac{\partial^2\Gamma}{\partial y\partial z} &= \frac{M_M^2 E_{M'}}{2^9\pi^3}\ [z^2(\ |A+B|^2+|C|^2\ ) \\ &+ \quad (\ |B|^2+|D|^2\ )\ (y^2-\frac{1}{4}\lambda(1,r^2,z))^2], \end{aligned} \tag{4.53}$$

of course, in the heavy quark limit $E_{M'} \to M'$ as well.

Calculation

For the process $B \to D\gamma\gamma$ there are 5 diagrams involving only the H doublet, shown schematically on Fig.4.5. Diagrams Fig.4.5 (d) and (e) vanish at leading order due to the condition $v_\mu(g^{\mu\nu} - v^\mu v^\nu) = 0$ at the weak vertex, and we are left with three LO diagrams. Two of these diagrams have a $B - D$ weak transition and the third one has a $B^\star - D^\star$ weak transition. In all cases the two photons are emitted from magnetic dipole couplings on the external legs.

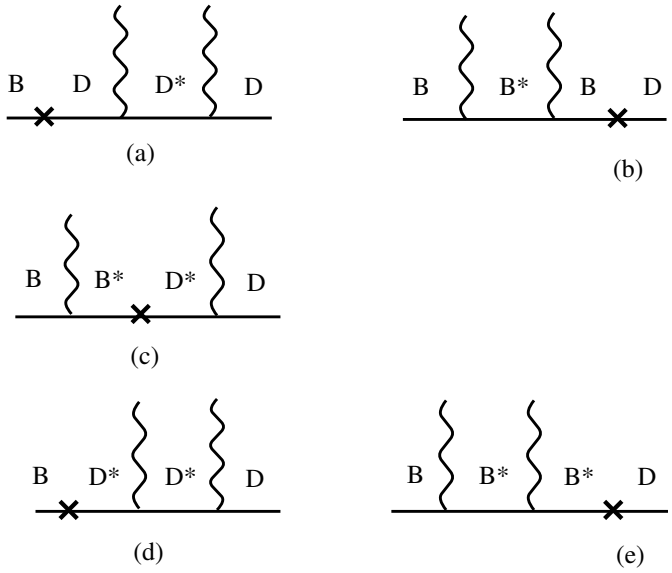

Figure 4.5 Pole diagrams responsible for $B \to D^\star\gamma\gamma$ at leading order in heavy quark and chiral theories.

A straightforward calculation then yields the desired amplitude for $B^0 \to \bar{D}^0\gamma\gamma$. In terms of the form factors defined in Eq.4.45, we find

$$\begin{aligned} A &= -C_n\left[\frac{\mu_D^2}{\Delta m}\left(\frac{1}{\Delta m - E_1} + \frac{1}{\Delta m - E_2}\right) + \frac{\mu_B^2}{E_1 E_2}\right. \\ &+ \left.\mu_B\mu_D\left(\frac{1}{E_1(\Delta m - E_1)} + \frac{1}{E_2(\Delta m - E_2)}\right)\right], \\ B &= -\frac{A}{2}, \end{aligned} \tag{4.54}$$

where E_1 and E_2 are photons energies, $\Delta m \equiv m_B - m_D$, and we have defined

$$C_n \equiv 2\sqrt{2}\pi G_F \alpha_{em} \beta'_W V^\star_{cb} V_{ud} M_B^2. \tag{4.55}$$

Using these lowest order form factors, we find a large range for the double radiative decay rates depending on the model used for the magnetic moments; for the mode with most favored Cabibbo-Kobayashi-Maskawa (CKM) angles,

$$0.3 \times 10^{-10} \lesssim B(B^0 \to \bar{D}^0 \gamma\gamma) \lesssim 3.5 \times 10^{-10}. \tag{4.56}$$

This large sensitivity to the input parameters is due in part to a cancellation between the terms involving the magnetic moments for the charm and bottom mesons. To illustrate this, we write

$$\mu_D = -r_\mu \mu_B, \tag{4.57}$$

and show in Figure 4.6 $\Gamma(B^0 \to \bar{D}^0\gamma\gamma)$ as a function of r_μ. We use the RQM magnetic moment for the B; and we normalize the rate to its value when $r_\mu \sim 2.87$, the value of μ_D in the RQM.

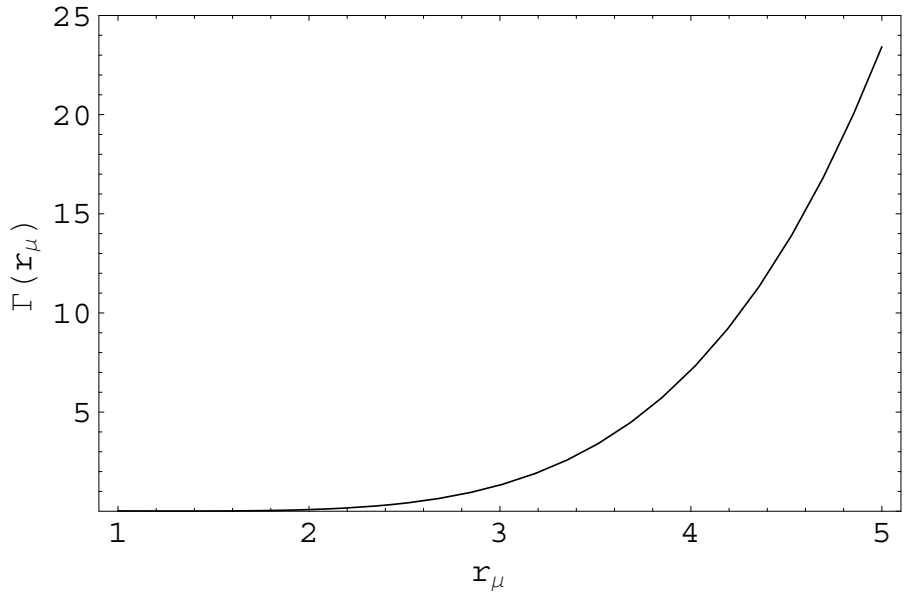

Figure 4.6 $\Gamma(B^0 \to \bar{D}^0\gamma\gamma)$ as a function of r_μ. We use the RQM magnetic moment for the B and we normalize the rate to its value when $r_\mu \sim 2.87$, the value of μ_D in the RQM.

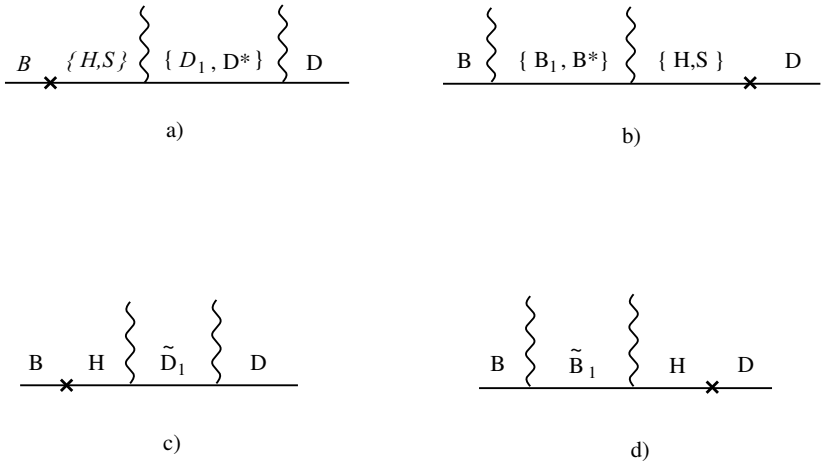

Figure 4.7 Additional diagrams involving particles from the $(0^+, 1^+)$ and $(1^+, 2^+)$ doublets. H(S) stands for either of the H(S)-multiplet members

We next consider two other types of contribution. First, the non-leading contributions from diagrams d and e. They arise from corrections to the 1^- propagator that are fixed by reparametrization invariance resulting in

$$\begin{aligned} C &= \frac{C_n}{2}\left[\frac{\mu_D\mu_{D^\star}}{\Delta m}\frac{m_B^2-m_D^2}{m_D^2}\left(\frac{1}{\Delta m-E_1}+\frac{1}{\Delta m-E_2}\right)+\frac{\mu_B\mu_{B^\star}}{E_1E_2}\frac{m_B^2-m_D^2}{m_B^2}\right] \\ D &= -\frac{C_n}{2}\left[\frac{\mu_D\mu_{D^\star}}{\Delta m}\frac{m_B^2-m_D^2}{m_D^2}\left(\frac{1}{\Delta m-E_1}-\frac{1}{\Delta m-E_2}\right)-\frac{\mu_B\mu_{B^\star}(E_2-E_1)}{E_1E_2(E_1+E_2)}\frac{m_B^2-m_D^2}{m_B^2}\right]. \end{aligned} \tag{4.58}$$

Additional contributions arise when the positive parity states appear as in Figure 4.7. The contributions from the S multiplet are

$$A = -C_n\left[\frac{\mu_D^S\mu_D}{\Delta m}\frac{m_B^2-m_D^2}{m_D^2}\left(\frac{1}{\Delta m-E_1}+\frac{1}{\Delta m-E_2}\right)-\frac{\mu_B^S\mu_B}{E_1E_2}\frac{m_B^2-m_D^2}{m_B^2}\right] \tag{4.59}$$

$$\begin{aligned} B &= \frac{C_n}{2}\left[\frac{\mu_D^S(\mu_D^S+\mu_D\frac{m_B^2-m_D^2}{m_D^2})}{\Delta m}\left(\frac{1}{\Delta m-E_1}+\frac{1}{\Delta m-E_2}\right)+\frac{\mu_B^S(\mu_B^S-\mu_B\frac{m_B^2-m_D^2}{m_B^2})}{E_1E_2}\right] \\ C &= -\frac{C_n}{2}\left[\frac{\mu_D^S}{\Delta m}(\mu_D-\mu_D^S\frac{m_B^2-m_D^2}{m_D^2})\left(\frac{1}{\Delta m-E_1}+\frac{1}{\Delta m-E_2}\right)+\frac{\mu_B^S}{E_1E_2}(\mu_B-\mu_B^S\frac{m_B^2-m_D^2}{m_B^2})\right] \\ D &= \frac{C_n}{2}[\ \frac{\mu_D^S}{\Delta m}(\mu_D+\mu_D^S\frac{m_B^2-m_D^2}{m_D^2})\left(\frac{1}{\Delta m-E_1}-\frac{1}{\Delta m-E_2}\right) \\ &\quad -\ \frac{\mu_B^S(E_2-E_1)}{E_1E_2(E_1+E_2)}(\mu_B+\mu_B^S\frac{m_B^2-m_D^2}{m_B^2})\ ]. \end{aligned} \tag{4.60}$$

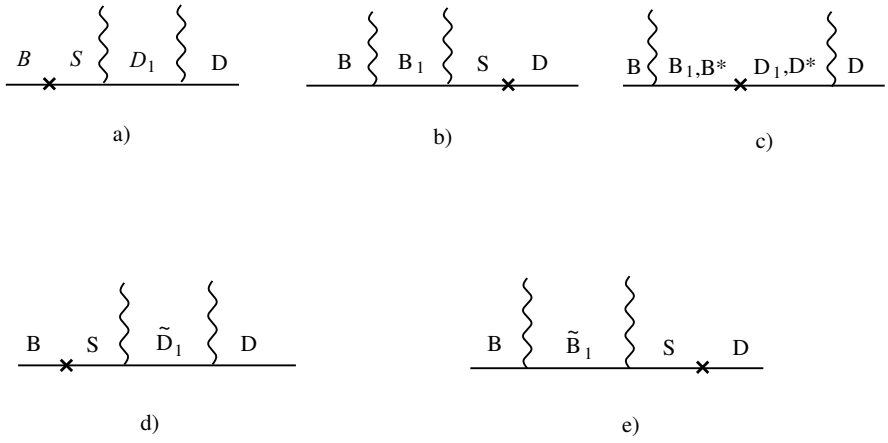

Figure 4.8 Additional diagrams involving particles from the $(0^+, 1^+)$ and$(1^+, 2^+)$ doublets. S stands for either of the S-multiplet members

The contributions from intermediate T doublet states are

$$
\begin{aligned}
B &= 4C_n \left[\frac{(\mu_D^T)^2}{\Delta m} \left(\frac{1}{\Delta m - E_1} + \frac{1}{\Delta m - E_2} \right) + \frac{(\mu_B^T)^2}{E_1 E_2} \right] \qquad (4.61) \\
C &= -2C_n \left[\frac{(\mu_D^T)^2}{\Delta m} \frac{m_B^2 - m_D^2}{m_D^2} \left(\frac{1}{\Delta m - E_1} + \frac{1}{\Delta m - E_2} \right) + \frac{(\mu_B^T)^2}{E_1 E_2} \frac{m_B^2 - m_D^2}{m_B^2} \right] \\
D &= -2C_n \left[\frac{(\mu_D^T)^2}{\Delta m} \frac{m_B^2 - m_D^2}{m_D^2} \left(\frac{1}{\Delta m - E_1} - \frac{1}{\Delta m - E_2} \right) - \frac{(\mu_B^T)^2 (E_2 - E_1)}{E_1 E_2 (E_1 + E_2)} \frac{m_B^2 - m_D^2}{m_B^2} \right].
\end{aligned}
$$

Additional contributions from SS and TS multiplet transitions are shown in Figure 4.8. We

split them into those from diagrams with two members of the S doublet:

$$\begin{aligned}
B &= \frac{C_n}{2}\left[\frac{\mu_D^S\mu_{D^\star}\frac{m_B^2-m_D^2}{m_D^2}}{\Delta m}\left(\frac{1}{\Delta m-E_1}+\frac{1}{\Delta m-E_2}\right)-\frac{\mu_B^S\mu_{B^\star}\frac{m_B^2-m_D^2}{m_B^2}}{E_1E_2}\right.\\
&+ \left.\mu_B^S\mu_D^S\left(\frac{1}{E_1(\Delta m-E_1)}+\frac{1}{E_2(\Delta m-E_2)}\right)\right],\\
C &= -\frac{C_n}{2}\left[\frac{\mu_D^S\mu_D}{\Delta m}\left(\frac{1}{\Delta m-E_1}+\frac{1}{\Delta m-E_2}\right)+\frac{\mu_B^S\mu_B}{E_1E_2}\right.\\
&- \left.(\mu_B^S\mu_D-\mu_D^S\mu_B)\left(\frac{1}{E_1(\Delta m-E_1)}+\frac{1}{E_2(\Delta m-E_2)}\right)\right],\\
D &= -\frac{C_n}{2}\left[\frac{\mu_D^S\mu_D}{\Delta m}\left(\frac{1}{\Delta m-E_1}-\frac{1}{\Delta m-E_2}\right)-\frac{\mu_B^S\mu_B(E_2-E_1)}{E_1E_2(E_1+E_2)}\right.\\
&+ \left.(\mu_B^S\mu_D+\mu_D^S\mu_B)\left(\frac{1}{E_1(\Delta m-E_1)}-\frac{1}{E_2(\Delta m-E_2)}\right)\right],
\end{aligned} \tag{4.62}$$

and those from diagrams with one member of the S doublet and one member of the T doublet:

$$\begin{aligned}
B &= \frac{2C_n}{\sqrt{3}}\left[\frac{\mu_D^T\mu_D^{TS}}{\Delta m}\frac{m_B^2-m_D^2}{m_D^2}\left(\frac{1}{\Delta m-E_1}+\frac{1}{\Delta m-E_2}\right)+\frac{\mu_B^T\mu_B^{TS}}{E_1E_2}\frac{m_B^2-m_D^2}{m_B^2}\right]\\
C &= \frac{4C_n}{\sqrt{3}}\left[\frac{\mu_D^T\mu_D^{TS}}{\Delta m}\left(\frac{1}{\Delta m-E_1}+\frac{1}{\Delta m-E_2}\right)-\frac{\mu_B^T\mu_B^{TS}}{E_1E_2}\right]\\
D &= \frac{4C_n}{\sqrt{3}}\left[\frac{\mu_D^T\mu_D^{TS}}{\Delta m}\left(\frac{1}{\Delta m-E_1}-\frac{1}{\Delta m-E_2}\right)+\frac{\mu_B^T\mu_B^{TS}(E_2-E_1)}{E_1E_2(E_1+E_2)}\right].
\end{aligned} \tag{4.63}$$

In a similar manner we obtain the result for $B^\pm \to D^\pm\gamma\gamma$ with the replacements $V_{cb}V_{ud}\beta'_W \to V_{ub}V_{cd}\beta_W$, for $B_s^0 \to D^0\gamma\gamma$ with $V_{ud} \to V_{us}$ and $B^\pm \to D_s^\pm\gamma\gamma$ with $V_{cb}V_{ud}\beta'_W \to V_{ub}V_{cs}\beta_W$.

Numerically, we find the following ranges for the branching ratios when we vary the magnetic moments over the range predicted in the three different models:

$$\begin{aligned}
1.7\times10^{-8} \lesssim\ & B(B^0\to\bar D^0\gamma\gamma) \lesssim 8.0\times10^{-8},\\
0.8\times10^{-9} \lesssim\ & B(B_s^0\to\bar D^0\gamma\gamma) \lesssim 4.3\times10^{-9},\\
0.6\cdot10^{-11} \lesssim\ & B(B^\pm\to D^\pm\gamma\gamma) \lesssim 2.0\cdot10^{-11},\\
1.1\cdot10^{-10} \lesssim\ & B(B^\pm\to D_s^\pm\gamma\gamma) \sim 3.6\cdot10^{-10}.
\end{aligned} \tag{4.64}$$

Once again these ranges include only variations of the rates with the magnetic moments in the χLM, VMD and RQM. They do not include other uncertainties such as that in the value of β_W.

It is instructive to examine some of the features of the differential decay rates, and we do so for the mode with most favorable CKM angles, $B^0 \to \bar{D}^0\gamma\gamma$. We first plot in Figure 4.9 the normalized differential decay rate as a function of z, the dimensionless photon pair invariant mass defined in Eq. (4.46). The distribution does not have any thresholds as our calculation does not include absorptive parts. It is peaked at the higher invariant masses. To evaluate

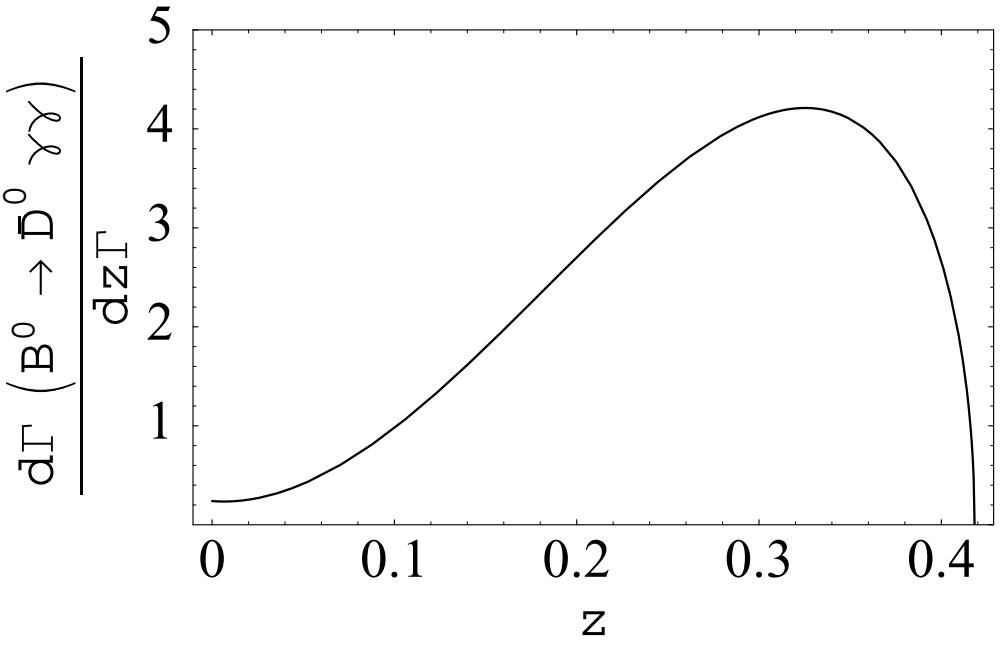

Figure 4.9 Normalized differential decay rate for $B^0 \to \bar{D}^0\gamma\gamma$ as a function of the photon pair invariant mass.

the limits of the heavy quark expansion, we first show in Figure 4.10 the double differential decay rate as a function of the energies of the two photons as a density plot. The darker regions correspond to the most populated ones. The distribution is dominated by the region in which both photons tend to have similar energy between 1 and 2 GeV. This indicates that the approximation of constant magnetic moments for the photon emission vertices is slightly better for the double radiative decay modes than it was for the single radiative decay mode where $E_\gamma \sim 2.3$ GeV. However, it is clear that a substantial uncertainty remains due to this approximation.

Finally, we show again the normalized differential decay rate as a function of $\omega = v \cdot v'$

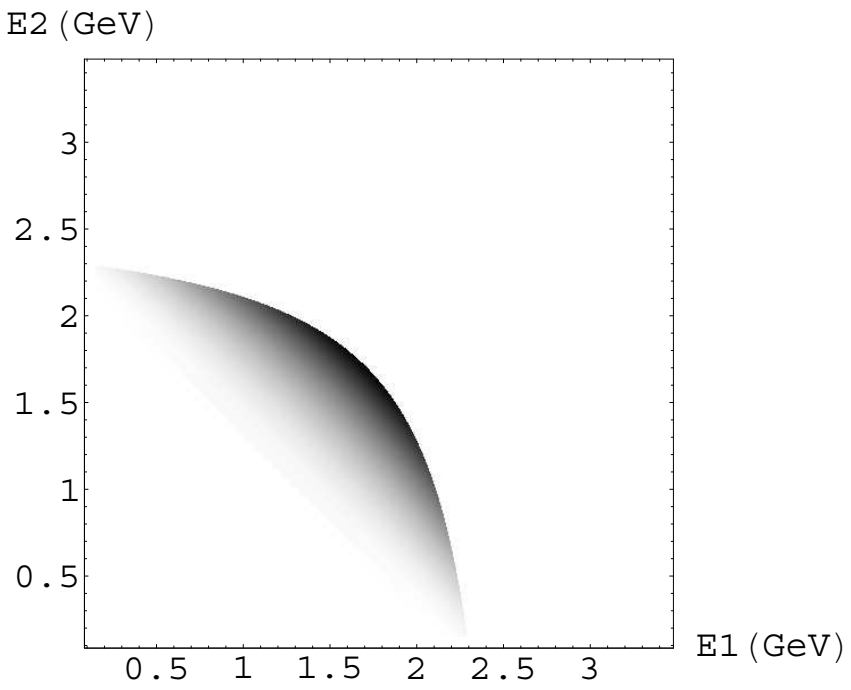

Figure 4.10 Density plot for the double differential decay rate for $B^0 \to \bar{D}^0\gamma\gamma$ as a function of the two photon energies.

in Figure 4.11. Here we see that the distribution is peaked at $\omega \sim 1.1$, not too far from the symmetry limit. The heavy quark expansion should be better behaved for these modes than it is for the single radiative decays where $\omega \sim 1.5$.

Additional contributions

We turn our attention to potential contributions with a different topology that have not appeared so far. Specifically, we have in mind contributions in which the weak decay $B \to DX$ is followed by the electromagnetic $X \to \gamma\gamma$ vertex. We do not have a systematic way to include these contributions, but we illustrate them with a few examples. In any case, if there is a dominant contribution of this form, the photon pair invariant mass would be concentrated around M_X and would be easy to isolate experimentally.

An example of this topology with a $c\bar{c}$ resonance is $B \to D\eta_c \to D\gamma\gamma$. Using the narrow

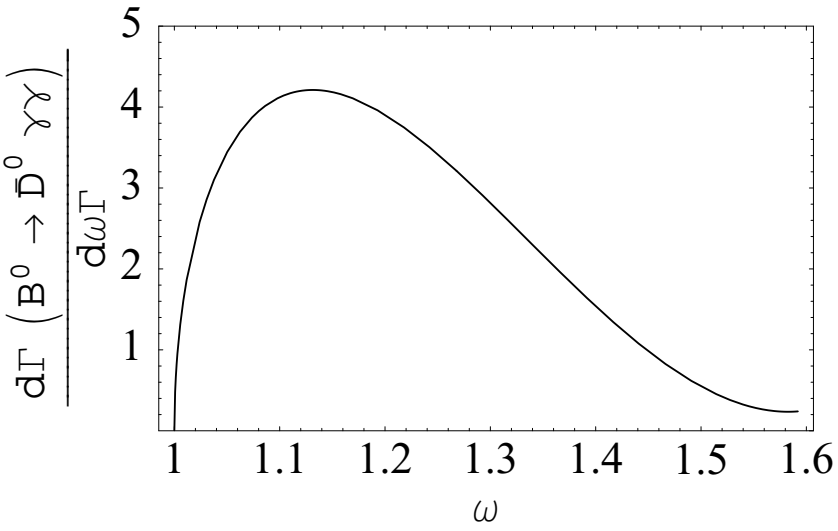

Figure 4.11 Normalized differential decay rate for $B^0 \to \bar{D}^0\gamma\gamma$ as a function of $\omega = v \cdot v'$.

width approximation, one finds $\Gamma(B \to D\gamma\gamma) = \Gamma(B \to \eta_c D) \cdot \mathcal{B}(\eta_c \to \gamma\gamma)$. Experimentally, it is known that $\mathcal{B}(\eta_c \to \gamma\gamma) = 4.3 \cdot 10^{-4}$ [25]. For the weak vertex we can use a recent perturbative QCD (pQCD) calculation as an illustration, $\mathcal{B}(B \to \eta_c D) = 1.28 \cdot 10^{-5}$ [51]. This then leads to a contribution $\mathcal{B}(B^0 \to \bar{D}^0\gamma\gamma) \sim 5.5 \cdot 10^{-9}$ smaller than our result in Eq. 4.64. A different estimate $\mathcal{B}(B \to \eta_c D) = 1.52 \cdot 10^{-7}$ [52] would make this contribution even smaller. Another charmonium resonance with a measured two photon width is the $\chi_{c0}(1P)(0^+)$. Since the measured branching ratio is $\mathcal{B}(\chi_{c0}(1P)(0^+) \to \gamma\gamma) = 2.6 \cdot 10^{-4}$, similar to that for $\eta_c \to \gamma\gamma$ we expect, at most, a similar contribution to the double radiative B decay.

We expect much larger contributions from the light pseudoscalars. This can be illustrated using the measured rates for $\mathcal{B}(B^0 \to \bar{D}^0 X)$, $X = \pi^0, \eta, \eta'$, which are all at the 10^{-4} level, and the respective two photon widths which range from nearly 100% for the π^0 to a few percent for the η'. These contributions would, however, be easily separated experimentally as the two photon invariant mass distribution would correspond to sharp peaks at the respective m_X.

4.1.6 Summary and Conclusions

We studied the weak radiative decays of B mesons that occur at tree-level in the Standard Model. We presented a numerical estimate for the inclusive double radiative decay $b \to X_c\gamma\gamma$ based on a free quark decay calculation. Our estimate indicates that this mode is about an order of magnitude larger than the double radiative penguin mode $b \to X_s\gamma\gamma$. As such, it can be studied at future Super-B factories.

We applied the HQET formalism in connection with the study of the single radiative exclusive modes of the form $B \to D^\star\gamma$. We first reproduced existing results in the literature for both charged and neutral modes with a leading order calculation including only the $(0^-, 1^-)$ doublet as intermediate states. These calculations exhibit a large sensitivity to the value of the electromagnetic couplings due to a partial cancellation. We then improved these lowest order results by including certain known terms of order $(m_b - m_c)/m_c$ as well as by introducing the positive parity doublets S and T as intermediate states. These two ingredients significantly enhance the predictions as they remove the cancellation that occurs at lowest order. The framework is a good approximation in the $m_b \sim m_c$ limit, but significant corrections are expected for the physical values of quark masses.

Finally, we extended the calculations to the double radiative decay modes of the form $B \to D\gamma\gamma$. Once again we found significant cancellations between the lowest order terms and a much larger rate when the positive parity states are included in the calculation. The mode with the most favorable CKM angles is predicted at the 10^{-8} level, comparable to predictions for $B \to K\gamma\gamma$.

We expect the HQET formalism to work best in the case when the velocity of the heavy hadrons remains constant during the transition. Whereas this is kinematically impossible in the single radiative decay modes, there are regions of phase space in the double radiative decay modes where this could be tested (in principle at least). We illustrate these regions with plots of the relevant differential decay rates.

4.2 The role of D^{**} in $B \to D_S K\pi$ decay

Our next example deals with the recently reported observation of the decay mode $B^- \to D_s^+ K^- \pi^-$ by the The BaBar collaboration. We will investigate the role played by the $D^{\star\star}$ excited meson states resonances in this decay mode using HQET. Although these resonances cannot appear as physical intermediate states in this reaction, their mass is very close to the $D_s^+ K^-$ production threshold and may, therefore, play a prominent role. We will pursue this possibility to extract information on the properties of the strong $D^{\star\star}DM$ couplings. As a byproduct of this analysis, we will point out that future super-B factories may be able to measure the $D_0^0 D^\star\gamma$ radiative coupling through the reaction $B^- \to D^\star\gamma\pi^-$.

4.2.1 Introduction

The BaBar collaboration has recently reported the observation of the decay mode $B^- \to D_s^+ K^- \pi^-$ with a branching ratio $\mathcal{B}(B^- \to D_s^+ K^- \pi^-) = (2.02 \pm 0.13_{stat} \pm 0.38_{syst}) \times 10^{-4}$ and the $D_s^+ K^-$ invariant mass spectra shown on Fig.4.12 [56].

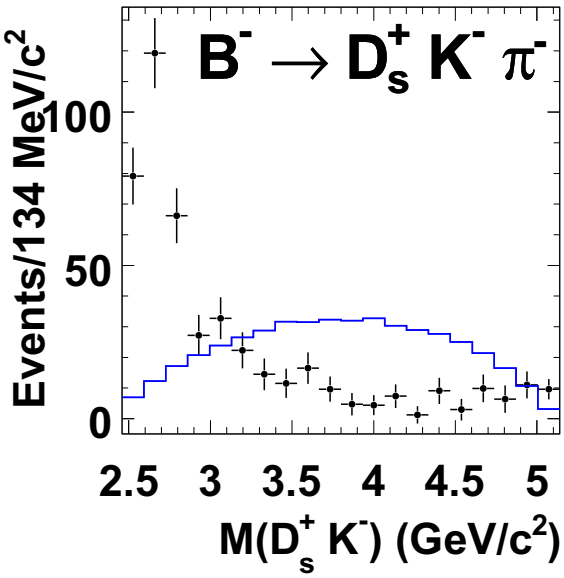

Figure 4.12 The $D_s^+ K^-$ invariant mass spectra for the $B^- \to D_s^+ K^- \pi^-$. The histogram shows the non-resonant signal Monte Carlo events distribution, scaled to the number of events in the data signal region [56].

This decay mode is different from the mode $B^- \to D^{\star\star}\pi^- \to D^+\pi^-\pi^-$ observed by Belle [57] in that the $D^{\star\star}$ resonances are too light to decay into $D_s^+K^-$. Nevertheless their masses [57],

$$\begin{aligned} m_{D_0^{\star\star}} &= (2308 \pm 17 \pm 15 \pm 28)\ MeV \\ m_{D_2^{\star\star}} &= (2461.6 \pm 2.1 \pm 0.5 \pm 3.3)\ MeV, \end{aligned} \tag{4.65}$$

are sufficiently close to the threshold for production of $D_s^+K^-$ that we can entertain the possibility of them playing a significant role in $B^- \to D_s^+K^-\pi^-$ as "quasi-resonant" intermediate states. This hypothesis is supported by Fig.4.12, as the $D_s^+K^-$ spectra is incompartible with the three-body phase space [56].

We use HQET to investigate this possibility. This study will serve as a probe of the properties of the $D^{\star\star}DM$ interactions, where M is a member of the light pseudoscalar meson octet. In particular, we can check the $SU(3)$ relations in strong $D^{\star\star}$ decay. In addition, an analysis of a distribution with respect to the angle between the pion and kaon momenta can further constrain the D_2^0 tensor couplings.

Schematically, our procedure consists of splitting the decay $B^- \to D_s^+K^-\pi^-$ into "quasi-resonant" and non-resonant contributions as depicted in Figure 4.13, where, again, we are using the effective vertices which we will specify later.

If the $D^{\star\star}$ resonances were heavy enough to decay into $D_s^+K^-$, we would expect the "quasi-resonant" contribution to dominate. Furthermore, in the narrow width approximation the production and decay processes would factorize; and we could study the properties of the strong decay vertex. We investigate the extent to which the "quasi-resonant" process dominates by first computing the amplitudes with the aid of HQET. We then normalize the resulting rates to the two-body $B^- \to D_{0,2}^0\pi^-$ weak decay rates and use this as a constraint on the weak transition. Finally, we study the behavior of the normalized rates for different parametrizations of the weak vertex, treating the residual dependence on the weak vertex as an indication of the extent to which the "quasi-resonant" contribution dominates.

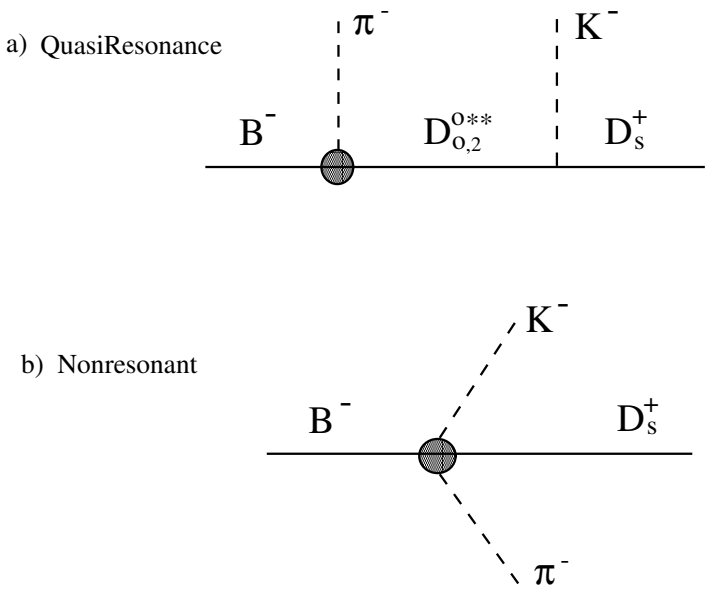

Figure 4.13 Decomposition of the decay mode $B^- \to D_s^+ K^- \pi^-$ into contributions that are mediated by a $D^{\star\star}$ that is near its mass shell and those that are not.

4.2.2 Formalism

We use the HQET formalism to describe the interactions involving the heavy meson $(0^-, 1^-)$ doublet, its excited positive parity partners $(0^+, 1^+)$ and $(1^+, 2^+)$, and light pseudo-scalar mesons [27, 58, 28, 37, 29, 32]. We again follow standard notation to incorporate the light pseudo-scalars as the Goldstone bosons of spontaneously broken chiral symmetry through the matrix $\xi = \exp(\frac{iM}{f_\pi})$ with a normalization in which the pion decay constant is $f_\pi = 132$ MeV (the matrix M is explicitly given in Eq.2.1).

Similarly, the heavy meson doublets are described by the following fields and their conju-

gates,

$$\begin{aligned}
(0^-,1^-) &\rightarrow H = \frac{1+\not{v}}{2}(P\!\!\!/^* - P\gamma_5),\ \bar{H} = \gamma_0 H^\dagger \gamma_0 \\
(0^+,1^+) &\rightarrow S = \frac{1+\not{v}}{2}(P\!\!\!/_1\gamma_5 - P_0),\ \bar{S} = \gamma_0 S^\dagger \gamma_0 \\
(1^+,2^+) &\rightarrow T^\mu = \frac{1}{2}(1+\not{v})\left[P_2^{\mu\nu}\gamma_\nu - \sqrt{3/2}\tilde{P}_{1\nu}\gamma_5(g^{\mu\nu} - \frac{1}{3}\gamma^\nu(\gamma^\mu - v^\mu))\right], \\
&\quad \bar{T}^\mu = \gamma_0 T^{\dagger\mu}\gamma_0.
\end{aligned} \tag{4.66}$$

At leading order in the heavy quark and chiral expansions, the strong interaction mediated decays of the form $H, S, T \rightarrow HM$ are described by the Lagrangians [27, 58, 28, 38]

$$\begin{aligned}
\mathcal{L}_H &= g\ Tr\left[H\gamma_\mu\gamma_5 A^\mu \bar{H}\right], \\
\mathcal{L}_S &= h\ Tr\left[S\gamma_\mu\gamma_5 A^\mu \bar{H}\right] + \text{h.c.}, \\
\mathcal{L}_T &= \frac{h_1}{\Lambda_\chi} Tr\left[H\gamma_\lambda\gamma_5(D_\mu A^\lambda)\bar{T}^\mu\right] + \frac{h_2}{\Lambda_\chi} Tr\left[H\gamma_\lambda\gamma_5(D^\lambda A_\mu)\bar{T}^\mu\right] + \text{h.c.},
\end{aligned} \tag{4.67}$$

where the axial current is given by

$$A_\mu \equiv \frac{i}{2}(\xi^\dagger\partial_\mu\xi - \xi\partial_\mu\xi^\dagger), \tag{4.68}$$

and the traces are over Dirac and flavor indices. For our numerical estimates we will use the values $|h'| = |(h_1+h_2)/\Lambda_\chi| \approx 0.5\ \text{GeV}^{-1}$, $h = -0.52$ and $g = 0.4$ [59, 32]. We will also replace $f_\pi \rightarrow f_K \sim 1.3 f_\pi$ where appropriate.

It is a simple exercise to write the corresponding weak vertices describing the transitions from a b-quark meson to a c-quark meson. In this case, however, we do not expect a reliable description of the weak transition as the $m_b - m_c$ mass difference is larger than Λ_χ. We will use the HQET framework to parametrize the weak transitions in a manner similar to that of Ref. [60]. We then treat the result as a phenomenological description of the weak transition in terms of three free parameters that are constrained by the two body decays $B^- \rightarrow D^0_{0,2}\pi^-$.

The dominant short distance operator responsible for the decays $B^- \rightarrow D_s^+ K^-\pi^-$, $B^- \rightarrow D^+\pi^-\pi^-$ is an $SU(3)$ octet of the form $\bar{c}\gamma_\mu(1-\gamma_5)b\bar{d}\gamma^\mu(1-\gamma_5)u$. We use standard techniques [61] to introduce this operator into the HQET formalism. We first construct the matrix λ_{12} with ${\lambda_{12}}^i_j = \delta^i_1\delta^2_j$ to represent the $SU(3)$ properties of the operator. We then pretend that λ_{12}

transforms as $\lambda_{12} \to L\lambda_{12}L^\dagger$ under chiral symmetry and construct chiral symmetric operators that include λ_{12}. The transformation properties under chiral symmetry of the other relevant objects are $H_Q \to H_Q U^\dagger$, $\bar{H}_Q \to U\bar{H}_Q$, $\xi \to L\xi U^\dagger$, and $\xi^\dagger \to U\xi^\dagger L^\dagger$. With these ingredients we construct the effective weak Lagrangian beginning with the $H_b \to H_c$ transitions. There is only one term without derivatives (the sign is chosen to match the notation in [16]),

$$\mathcal{L}_W \;=\; \beta'_W Tr\left[\, H_b \xi^\dagger\, \gamma_\mu(1-\gamma_5)\, \lambda_{12}\, \xi \bar{H}^{\bar{c}}\, \gamma^\mu(1-\gamma_5)\,\right]. \tag{4.69}$$

There is also a unique term with one derivative,

$$\mathcal{L}_{W1} = ik_H\, Tr\left[H_{bj}\bar{H}^{\bar{c}j}\gamma_\mu(1-\gamma_5)\right]\;\; Tr\left[\xi^\dagger\lambda_{12}\partial^\mu\xi\right]. \tag{4.70}$$

Even though the operator Eq. 4.70 is formally suppressed by one order in the momentum expansion with respect to the one in Eq. 4.69, we will keep both of them for several reasons. First, because in a matching to the underlying quark-operator Eq. 4.69 is suppressed by $1/N_c$ with respect to Eq. 4.70; second, because we do not really expect the momentum expansion to be relevant in $b \to c$ transitions; and third, because Ref. [60] finds that an interplay of these two operators is necessary to describe the $B^- \to D^+\pi^-\pi^-$ decay. For all these reasons we will limit our discussion of the weak transitions to these two operators. In particular we will also ignore small contributions proportional to V_{ub}, as well as perturbative QCD corrections to the Wilson coefficient of the quark operator.

For weak transitions of the form $H_b \to S_c$, we consider two weak operators analogous to Eqs. 4.69 and 4.70 obtained by replacing $H_c \to S_c$. In principle these operators have different coefficients than those in Eqs. 4.69 and 4.70. However, we estimate all the weak coefficients in naive factorization where the constant β'_W for $H_b \to S_c$ transitions is related to the constant β'_W for $H_b \to H_c$ transitions by the factor $(f_{D_0}\sqrt{m_{D_0}})/(f_D\sqrt{m_D})$. For our estimates we take this factor to be one. Several models to estimate the quantities in this ratio are discussed in Ref. [60], resulting in the ratio differing from one by factors of at most two. In all the models considered in Ref. [60], the two constants have the same sign.

For weak transitions involving a T field, Eq. 4.69 will not have an analogue in this approximation (the tensor decay constant vanishes [32, 62, 63, 64]). The single weak operator in this

case reads

$$\mathcal{L}_T = ik_T Tr\left[v_\alpha \bar{T}^\alpha_{v'}\gamma_\mu(1-\gamma_5)H_v\right]\ Tr[\xi^\dagger\lambda_{12}\partial^\mu\xi\Big]\,. \tag{4.71}$$

The k_H, k_S and k_T coefficients are related in factorization, with their relative signs being given by those of the Isgur-Wise functions [40] $\xi(\omega), \tau_{1/2,3/2}(\omega)$. The factorization results that we use are

$$\begin{aligned}
\beta'_W &= \frac{G_F V_{cb}V_{ud}}{\sqrt{2}}\frac{1}{12} f_B f_D\sqrt{m_B m_D}B_1 \\
k_H &= -\frac{G_F V_{cb}V_{ud}}{\sqrt{2}} f_\pi^2 \xi(\omega) B_2 \\
k_S &= 2\frac{G_F V_{cb}V_{ud}}{\sqrt{2}} f_\pi^2 \tau_{1/2}(\omega) B_2 \\
k_T &= \frac{G_F V_{cb}V_{ud}}{\sqrt{2}}\sqrt{3}\tau_{3/2}(\omega) f_\pi^2 B_3.
\end{aligned} \tag{4.72}$$

In order to treat these weak vertices as a phenomenological parametrization, we have introduced "bag factors" $B_{1,2,3}$ that are equal to 1 in simple factorization but that we will allow to vary. We will also use recent estimates for the IW functions in the light-front formalism [65], taking $\omega \equiv v\cdot v' \approx 1.26$, an average for the range (1 - 1.53) that occurs in our application. We thus use $\xi(\omega) \approx 0.7$, $\tau_{1/2}(\omega) \approx 0.25$, and $\tau_{3/2}(\omega) \approx 0.35$. In addition, we take $f_B = 191$ MeV and $f_D = 225$ MeV. The relative sign of the constants β_W and k_S is important to reproduce the two body decay $B^- \to D_0^0\pi^-$, as discussed in Ref. [60]. Here we use the sign implied in Eq. 4.72 which reproduces the measured $B^- \to D_0^0\pi^-$ rate with bag parameters close to one.

Notice that this framework will describe all the non-resonant diagrams in terms of the same coupling constants as the "quasi-resonant" diagrams. Our strategy is thus to fix as many constants as possible from the on-shell two-body decay modes $B^- \to D^{\star\star}\pi^-$ and then use these results, supplemented with the HQET description of the strong $D^{\star\star}$ couplings, to predict the three-body decay mode.

4.2.3 $\mathbf{B^- \to D_s^+ K^-\pi^-}$ and the $\mathbf{D^{\star\star}}$ resonances

We are now in a position to investigate the contribution of the $D^{\star\star}$ resonances to the $B^- \to D_s^+K^-\pi^-$ process. Our strategy will be to compute the amplitude with the ingredients given in the previous section, schematically splitting it into the two terms pictured in Figure 4.13. In

the limit in which the quasi-resonant states dominate, it is possible to make reliable predictions that depend only on the theory of the strong $D^{\star\star}DM$ transitions because the weak production vertex and the strong decay vertex factorize, as they do in the narrow width approximation for a resonant channel. The weak transition can then be eliminated in favor of the measured $B^- \to D^+\pi^-\pi^-$. This approach completely fails as the non-resonant contribution becomes dominant in which case the two decay modes are not directly related. The formalism in the previous section will serve to interpolate between these two extremes, allowing us to explore the sensitivity of our result to the weak couplings.

We begin by computing the $B^- \to D_s^+K^-\pi^-$ amplitude from the diagrams shown in Fig.4.14. To construct these diagrams, we note that weak transitions involving the T multiplet arise only from Eq. 4.71, so the corresponding vertices always involve a π^-.

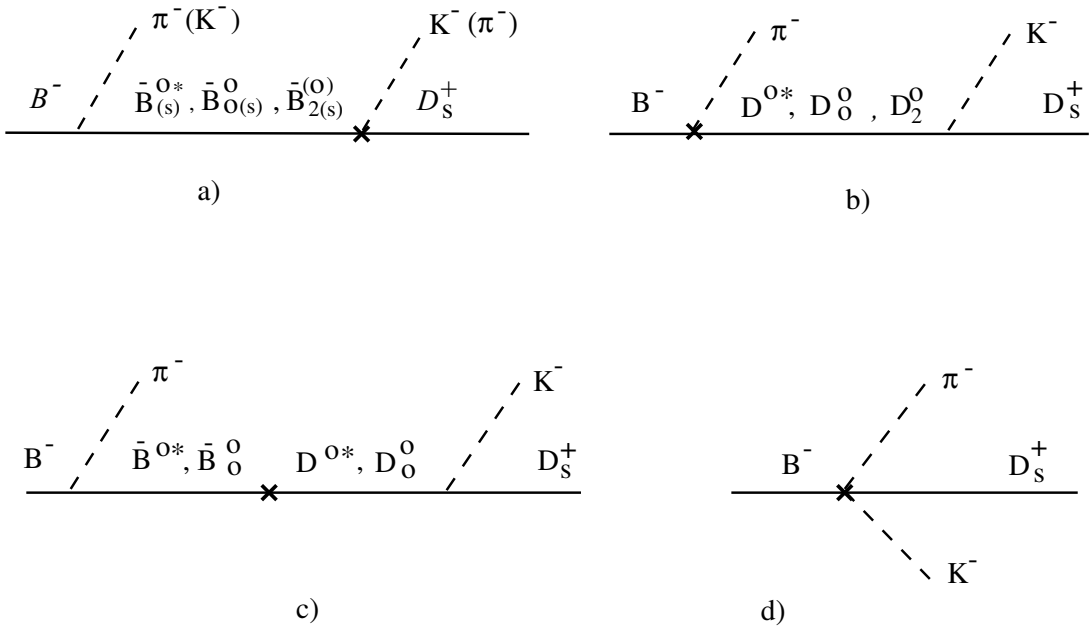

Figure 4.14 Diagrams contributing to $B^- \to D_s^+K^-\pi^-$. For diagrams of the form (a), the strange B intermediate states go with a pion emission from the weak vertex (denoted by an x).

The calculation proceeds as follows. We work in the B rest frame in which the heavy

meson has four velocity $v^\mu = (1,0,0,0)$. After a weak light meson emission, we solve for the velocity of the charmed heavy meson, v' for $D^0_{0,2}, D^{0*}$, using exact kinematics so that the residual momentum in the intermediate heavy meson propagator corresponds exactly to its off-shellness. For a weak vertex with pion emission, we use

$$v' = (\frac{m_B - E_\pi}{M_{D_s^+ K^-}}, -\frac{\vec{p}_\pi}{M_{D_s^+ K^-}}),\ \omega = v \cdot v' = \frac{m_B^2 + M^2_{D_s^+ K^-}}{2 m_B M_{D_s^+ K^-}}; \tag{4.73}$$

whereas for a weak vertex with a kaon emission, we use

$$v'' = (\frac{m_B - E_K}{M_{D_s^+ \pi^-}}, -\frac{\vec{p}_K}{M_{D_s^+ \pi^-}}). \tag{4.74}$$

To determine phenomenological values for our "bag factors," we use the experimental results [57],

$$\begin{aligned} \mathcal{B}(B^- \to D_0^0 \pi^-)\mathcal{B}(D_0^0 \to D^+\pi^-) &= (6.1 \pm 0.6 \pm 0.9 \pm 1.6) \times 10^{-4} \\ \mathcal{B}(B^- \to D_2^0 \pi^-)\mathcal{B}(D_2^0 \to D^+\pi^-) &= (3.4 \pm 0.3 \pm 0.6 \pm 0.4) \times 10^{-4}, \end{aligned} \tag{4.75}$$

supplemented with the theoretical input for the strong $D^{\star\star}$ decays as in [60, 66]. For the central values then,

$$\begin{aligned} \mathcal{B}(B^- \to D_0^0 \pi^-) &= 9.1 \times 10^{-4} \\ \mathcal{B}(B^- \to D_2^0 \pi^-) &= 8.7 \times 10^{-4}. \end{aligned} \tag{4.76}$$

The weak decay rates $B^- \to D_0^0 \pi^-$ and $B^- \to D_2^0 \pi^-$ can be calculated in the above framework with the results being

$$\begin{aligned} \Gamma(B^- \to D_0^0 \pi^-) &= \frac{E_{D_0^0} E_\pi}{8\pi m_B f_\pi} \left[4\beta'_W \omega_0 \left(1 + h \frac{m_B + m_{D_0^0}}{2 m_{D_0^0}} \right) - \frac{k_S E_\pi (m_{D_0^0} - m_B)}{m_{D_0^0}} \right]^2, \\ \Gamma(B^- \to D_2^0 \pi^-) &= \frac{k_T^2 E_{D_2} E_\pi (\omega_2^2 - 1)^2 (m_B + m_{D_2})^2}{12\pi^2 m_B f_\pi^2}, \end{aligned} \tag{4.77}$$

where $\omega_0 = \frac{E_{D_0^0}}{m_{D_0^0}} = 1.362$ and $\omega_2 = \frac{E_{D_2^0}}{m_{D_2^0}} = 1.306$. Setting these predictions, Eq. 4.77, equal to the values in Eq. 4.76, we find B_2 as a function of B_1. For our numerics we will use the three pairs $B_1 = 1$, $B_2 = 1.13$; $B_1 = 1.308$, $B_2 = 1$; and $B_1 = 1.15$, $B_2 = 1.06$. This comparison has also been used to fix the relative sign of k_S with respect to β'_W. From the second line it also follows that $B_3 = 1.3$.

We neglect mass splittings between members of a doublet, H, S, T, but include mass splittings between the different doublets. In addition, we set the pion mass to zero. We find it convenient to evaluate scalar products involving v' in the $D_s^+ K^-$ center of mass frame.

All this results in the following amplitudes. The three "quasi-resonant" diagrams (those that contain a D_0^0 meson in Fig.4.14.b,c) give:

$$\mathcal{M}_S = -\frac{h}{f_\pi f_K} \frac{v' \cdot q_K}{M_{D_s^+ K^-} - m_{D_0^0}} \left[4\beta'_W \omega \left(1 + h \frac{m_B + M_{D_s^+ K^-}}{2 M_{D_s^+ K^-}} \right) - \frac{k_S E_\pi (M_{D_s^+ K^-} - m_B)}{M_{D_s^+ K^-}} \right], \tag{4.78}$$

with E_π evaluated in the B rest frame. This D_0^0 contribution by itself has an $M_{D_s^+ K^-}$ invariant mass distribution shown as the solid line in Fig.4.15.

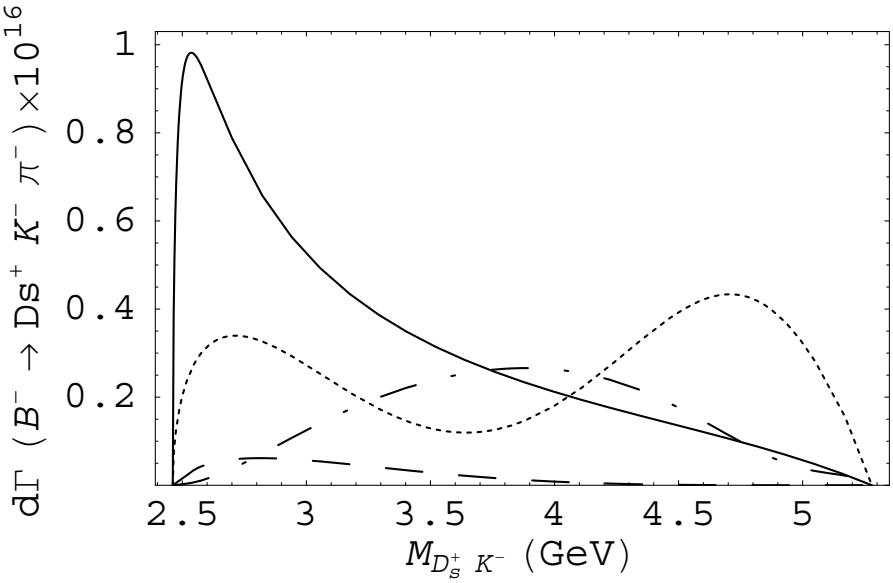

Figure 4.15 $M_{D_s^+ K^-}$ invariant mass distribution for $B_1 = 1$, $B_2 = 1.13$ for: a) diagrams involving a D_0^0 (solid line); b) diagrams involving a D_2^0 (dashed line) and c) all other diagrams: for $h' > 0$ (dotted line) and for $h' < 0$ (dash-dotted). Interference terms between (a), (b), and (c) are not shown.

There is one "quasi-resonant" diagram with an intermediate tensor $D_2^{\star\star}$ state (Fig.4.14.b). It yields an amplitude,

$$\mathcal{M}_T = \frac{h' k_T}{f_\pi f_K (M_{D_s^+ K^-} - m_{D_2^0})} \left\{ q_\pi \cdot v' \left[(E_K - \omega q_K \cdot v')^2 - \frac{1}{3}(1-\omega^2)(m_K^2 - (q_K \cdot v')^2) \right] \right.$$
$$\left. - (\omega + 1) \left[(q_\pi \cdot q_K - q_\pi \cdot v' q_K \cdot v')(E_K - \omega q_K \cdot v') - \frac{1}{3}(m_K^2 - (q_K \cdot v')^2)(E_\pi - \omega q_\pi \cdot v') \right] \right\}, \tag{4.79}$$

where $E_{\pi,K}$ are evaluated in the B rest frame. By itself the D_2^0 contribution has an $M_{D_s^+ K^-}$ invariant mass distribution shown as the dashed line in Fig.4.15.

Finally, there are the "non-resonant" diagrams that we divide into two groups. The diagrams from Fig.4.14.a,d give

$$\begin{aligned}
\mathcal{M}_{other} &= -\frac{4\beta'_W \omega}{f_\pi f_K} \left(1 - \frac{h q_\pi \cdot v'}{M_{D_s^+ K^-} - m_B} \right) + \frac{h k_S (v_{D_s^+} - v'') \cdot q_\pi \; v'' \cdot q_K}{f_\pi f_K (M_{D_s^+ \pi^-} - m_{B_{0s}^0})} \\
&+ \frac{4\beta'_W g (q_\pi \cdot q_D - q_\pi \cdot v' q_D \cdot v')}{f_\pi f_K (M_{D_s^+ K^-} - m_B) m_D} \\
&- \frac{g k_H (q_\pi \cdot q_K - q_\pi \cdot v'' q_K \cdot v'')}{f_\pi f_K (M_{D_s^+ \pi^-} - m_{B_s^\star})} \left(\frac{2 q_D \cdot q_\pi}{m_B m_D} + \frac{m_D}{m_B} + 1 \right) \\
&- \frac{h' k_T}{f_\pi f_K (M_{D_s^+ \pi^-} - m_{B_{2s}})} \left\{ (v'' \cdot v_{D_s^+} + 1) \left[(q_\pi \cdot q_K - q_\pi \cdot v'' q_K \cdot v'') \right. \right. \\
&\times (q_K \cdot v_{D_s^+} - v'' \cdot v_{D_s^+} q_K \cdot v'') - \frac{1}{3}(m_K^2 - (q_K \cdot v'')^2)(q_\pi \cdot v_{D_s^+} - v'' \cdot v_{D_s^+} q_\pi \cdot v'') \Big] \\
&- \left. \left. q_\pi \cdot v'' \left[(q_K \cdot v_{D_s^+} - v'' \cdot v_{D_s^+} q_K \cdot v'')^2 - \frac{1}{3}(1 - (v'' \cdot v_{D_s^+})^2)(m_K^2 - (q_K \cdot v'')^2) \right] \right\}.
\end{aligned} \tag{4.80}$$

Diagrams from Fig.4.14.b,c containing a D^{0*} intermediate state give:

$$\begin{aligned}
\mathcal{M}_{D^\star} &= -\frac{4 g \beta'_W}{f_\pi f_K (M_{D_s^+ K^-} - m_{D^\star})} \left[1 - \frac{k_H}{4\beta'_W} q_\pi \cdot v' \right] (E_K - \omega q_K \cdot v') \\
&+ \frac{g (q_\pi \cdot q_K - q_\pi \cdot v' q_K \cdot v')}{f_\pi f_K (M_{D_s^+ K^-} - m_{D^\star})} \left[-k_H (\omega + 1) + \frac{4 g \beta'_W}{M_{D_s^+ K^-} - m_{B^*}} \right].
\end{aligned} \tag{4.81}$$

To obtain the partial contribution from the "non-resonant" diagrams to the $M_{D_s^+ K^-}$ invariant mass distribution, it is necessary to know the sign of h'. Since this sign is not known, we present results for both signs shown as dotted and dash-dotted lines in Figure 4.15.

We now show the full result obtained by adding all contributions. This is not equal to the sum of the three curves in Figure 4.15 because that decomposition ignored the interference

between different terms. With $h' < 0$, we obtain a total $\mathcal{B}(B^- \to D_s^+ K^- \pi^-) = 1.63 \times 10^{-4}$; and with $h' > 0$, we find $\mathcal{B}(B^- \to D_s^+ K^- \pi^-) = 1.24 \times 10^{-4}$. The corresponding $M_{D_s^+ K^-}$ invariant mass distributions are shown in Fig.4.16 for three values of B_1 and B_2 as described earlier.

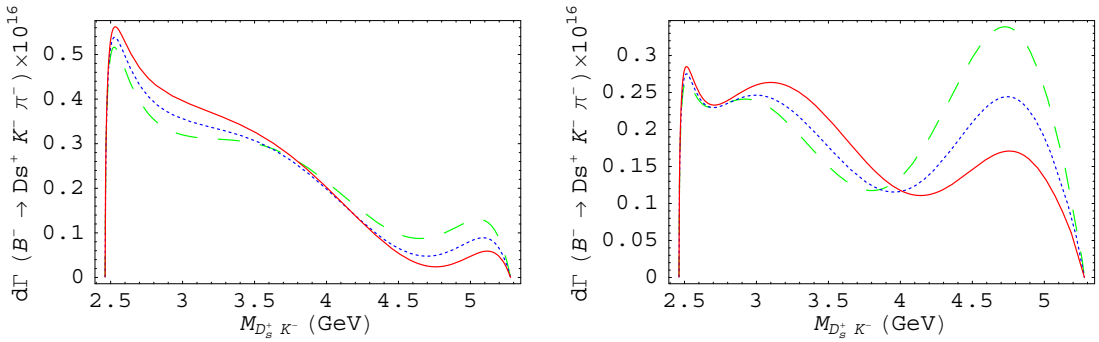

Figure 4.16 $M_{D_s^+ K^-}$ invariant mass distributions with $B_1 = 1$, $B_2 = 1.13$ (solid), $B_1 = 1.15$, $B_2 = 1.06$ (dotted), $B_1 = 1.308$, $B_2 = 1$ (dashed) for (a) $h' < 0$ and (b) $h' > 0$.

4.2.4 Discussion

A.Angular distributions

We now turn our attention to angular distributions and the additional information they provide. In particular, by studying the angular distribution $d\Gamma(B^- \to D_s^+ K^- \pi^-)/d\cos\theta$ for the angle θ between the momenta of the pion and the kaon in the $D_s^+ K^-$ center of mass frame, we can extract the amplitudes with different angular momentum. This frame would correspond to the rest frame of the $D^{\star\star}$ if it were produced as a physical intermediate state, so that this is the angular distribution that would normally be used to determine the spin of the resonance. In $B^- \to D_s^+ K^- \pi^-$ there is no resonance in the physical region, but we expect the different contributions to the rate to exhibit different angular distributions depending on the virtual intermediate state. This is made evident by rewriting the amplitudes in the $D_s^+ K^-$ center of mass frame. We find that the total amplitude in this frame can be written as a linear superposition of Legendre polynomials in $\cos\theta_{K^-\pi^-}$ (the angle between the K^- and π^-

momenta in the $D_s^+K^-$ center of mass frame),

$$\mathcal{M}(B^- \to D_s^+K^-\pi^-) = \mathcal{M}_0 P_0(\cos\theta_{K^-\pi^-}) + \mathcal{M}_1 P_1(\cos\theta_{K^-\pi^-}) + \mathcal{M}_2 P_2(\cos\theta_{K^-\pi^-}) + \cdots \tag{4.82}$$

With sufficient statistics it should be possible to fit the observed angular distribution to this form and to extract the different $\mathcal{M}_i$ components.

In terms of these components, we can write the differential decay rate as[3]

$$\frac{d\Gamma(B^- \to D_s^+K^-\pi^-)}{dM_{D_s^+K^-}} = \frac{E_{D_s^+}|\vec{p}_K^{\,\star}||\vec{p}_\pi|}{4(2\pi)^3 m_B}\left[|\mathcal{M}_0|^2 + \frac{1}{3}|\mathcal{M}_1|^2 + \frac{1}{5}|\mathcal{M}_2|^2 + \cdots\right], \tag{4.83}$$

and compare the different contributions, which correspond to the $D_s^+K^-$ system having angular momentum 0, 1 or 2 respectively.

Within our framework, the partial amplitudes are predicted to be,

$$\begin{aligned}
\mathcal{M}_0 &= -\frac{hE_K^\star}{f_\pi f_K(M_{D_s^+K^-} - m_{D_0^0})}\left\{4\beta'_W\omega\left[1 + h\frac{M_{D_s^+K^-}+m_B}{2M_{D_s^+K^-}} - \frac{E_\pi^\star(M_{D_s^+K^-}-m_{D_0^0})}{E_K^\star(M_{D_s^+K^-}-m_B)}\right]\right. \\
&- \left. k_S E_\pi^\star \frac{M_{D_s^+K^-}-m_B}{m_B}\right\} - \frac{4\beta'_W\omega}{f_\pi f_K} + a_0 \\
\mathcal{M}_1 &= \frac{g|\vec{q}_\pi||\vec{q}_K|}{f_\pi f_K(M_{D_s^+K^-} - m_{D^{*0}})}\left\{4\beta'_W\left[\frac{1}{m_B} - \frac{g}{M_{D_s^+K^-}-m_{B^*}} + \frac{M_{D_s^+K^-}-m_{D^{*0}}}{(M_{D_s^+K^-}-m_{B^*})m_D}\right]\right. \\
&+ \left. k_H\frac{M_{D_s^+K^-}+m_B}{m_B}\right\} + a_1 \\
\mathcal{M}_2 &= \frac{2}{3}\frac{h'k_T|\vec{q}_\pi|^2|\vec{q}_K|^2}{f_\pi f_K}\frac{M_{D_s^+K^-}+m_B}{(M_{D_s^+K^-}-m_{D_2^0})m_B^2} + a_2.
\end{aligned} \tag{4.84}$$

In Eq. 4.84 we have shown explicitly the contributions to the $J = 0, 1, 2$ amplitudes from the diagrams with an intermediate, "quasi-resonant" D_0^0, $D^{\star 0}$, and D_2^0 respectively. Additional contributions arise from the non-resonant diagrams; in particular, the diagrams in which B_{0s}^0, B_s^{0*} and B_{2s}^0 are exchanged with the K^- connected to the B vertex and the π^- connected to the D_s^+ vertex contribute to all values of angular momentum. We denote their projections into $J = 0, 1, 2$ by a_0, a_1, a_2 and evaluate these contributions numerically. We show this decomposition in Fig.4.17 for $B_1 = 1$, $B_2 = 1.13$ as a function of $D_s^+K^-$ invariant mass.

In Figure 4.17 we see that the contribution from M_0 is peaked at low $M_{D_s^+K^-}$ and that the height of the peak depends on the sign of h' through the interference between quasi-resonant

[3]The starred energies and momenta are evaluated in the $D_s^+K^-$ center of mass frame.

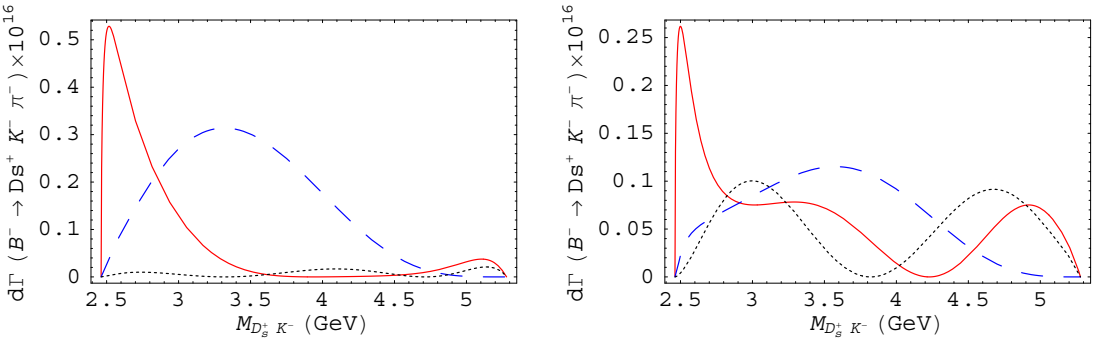

Figure 4.17 Contributions to the decay rate from different spin amplitudes for $B_1 = 1$, $B_2 = 1.13$ with: (a) $h' < 0$, (b) $h' > 0$. In both cases the solid line corresponds to M_0, the dotted line to M_1 and the dashed line to M_2. Higher spin contributions are negligible and are not shown.

Table 4.1 Partial branching ratios for spin amplitudes.

	$h' > 0$	$h' < 0$
$\mathcal{B}_0(B^- \to D_s^+ K^- \pi^-)$	4.4×10^{-5}	5.3×10^{-5}
$\mathcal{B}_1(B^- \to D_s^+ K^- \pi^-)$	3.6×10^{-5}	5.6×10^{-6}
$\mathcal{B}_2(B^- \to D_s^+ K^- \pi^-)$	4.3×10^{-5}	1.0×10^{-4}
$\mathcal{B}_{J>2}(B^- \to D_s^+ K^- \pi^-)$	4.2×10^{-8}	5.4×10^{-7}

and non-resonant diagrams. It is larger for $h' < 0$ where the non-resonant background is smaller in the low $M_{D_s^+ K^-}$ region as seen in Figure 4.15. This peak reflects the presence of the D_0^0 resonance just outside the physical region, and its height is sensitive to the mass of the D_0^0 as illustrated in Figure 4.18. In that figure we show the result with the central value of Eq. 4.65 as a solid line, and the one standard deviation values (adding all errors in quadrature) of $m_{D_0^0}$ as dashed and dotted lines.

Figure 4.17 also shows a large difference between the size of the M_1 contribution for different signs of h', and this may be exploited to determine this sign. Similarly, the contribution from M_2 is significantly larger when $h' < 0$ providing another handle on determining this sign. To further quantify the different contributions, we show the respective partial branching ratios in Table 5.1.

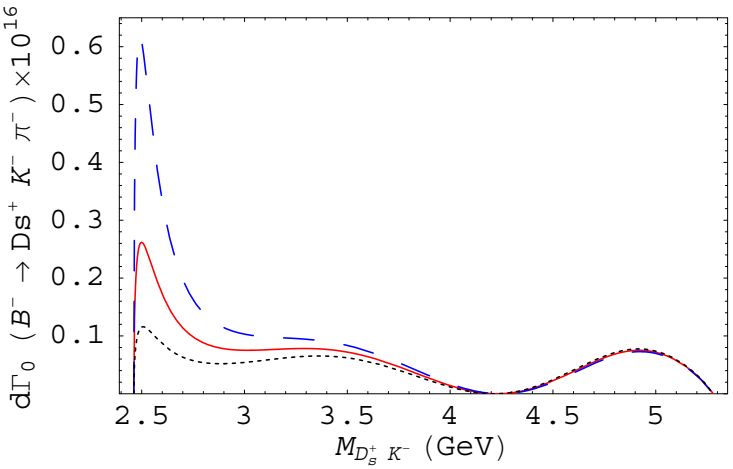

Figure 4.18 Scalar component of $\Gamma(B^- \to D_s^+ K^- \pi^-)$ for three different values of $m_{D_0^0}$ corresponding to the central value in Eq. 4.65 (solid), and to the one standard deviation values (dashed, dotted), with $h' > 0$.

B.Dependence on the parametrization of the weak vertex

In Figure 4.16 we have already presented results for three different pairs of values for B_1 and B_2. These correspond to different parametrizations for the weak vertex that reproduce the central value of the two body decay rates. We see from that figure that the variations are not large in the low $M_{D_s^+ K^-}$ region. We now explore in more detail the dependence of the total rate on these parameters. To this end, we first normalize the total decay rate $\Gamma(B^- \to D_s^+ K^- \pi^-)$ to the rate $\Gamma(B^- \to D_0^0 \pi^-)$ calculated in Eq. 4.77. We then plot this ratio as a function of the "bag factor" B_1 while adjusting B_2 in such a way that $B^- \to D_0^0 \pi^-$ remains fixed to its experimental (central) value in Figure 4.19a.

We see that the ratio changes by about a factor of two when we span the value of B_1 from 1/2 to 2 (recall $B_1 = 1$ in naive factorization). This variation indicates that our prediction for the full rate $\mathcal{B}(B^- \to D_s^+ K^- \pi^-)$ is not robust over the full kinematic range and that the process is not dominated by the $D_0^{\star\star}$ quasi-resonance. In the figure we also show the 1-σ band from the BaBar measurement [56], and we see that our prediction for the total rate is in good agreement.

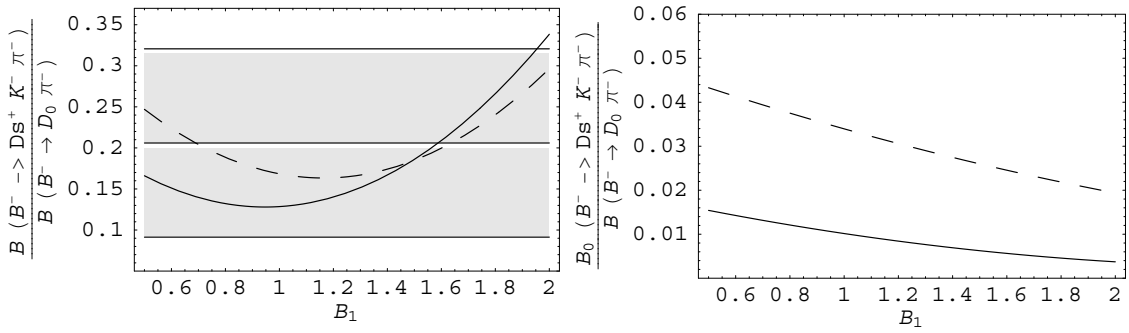

Figure 4.19 Normalized $\Gamma(B^- \to D_s^+ K^- \pi^-)$ as a function of B_1 factor for: a) full kinematic range; and b) scalar contribution in the $M_{D_s^+ K^-} \leq m_{D_0^0} + 2\Gamma_{D_0^0} \sim 2.8$ GeV range. The horizontal lines in (a) show the 1-σ range from the BaBar measurement [56]. In both cases the solid line corresponds to $h' > 0$ and the dashed line to $h' < 0$.

Following our general discussion, we might expect to do better if we limit the range for $M_{D_s^+ K^-}$ to values closer to the physical $m_{D_0^0}$ mass, since this would enhance the relative contribution of the "quasi-resonance". For illustration, we repeat the above exercise including only the partial branching ratio $\mathcal{B}_0(B^- \to D_s^+ K^- \pi^-)$ from the region $M_{D_s^+ K^-} \leq m_{D_0^0} + 2\Gamma_{D_0^0} \sim 2.8$ GeV. We also limit the comparison to the scalar contribution to the rate, as this is the one that could be dominated by the D_0^0 quasi-resonance. We show these results in Fig.4.19b. We notice a slight improvement in the form of reduced dependence of our prediction on the parametrization of the weak vertex. However, there is still a large dependence on the parametrization of the weak vertex as the ratio varies by a factor of about two in the range $0.5 < B_1 < 2$. This is not surprising as Figure 4.17 already showed that there is a large non-resonant contribution present.

4.2.5 $\mathbf{B^- \to D^0_{0,2}\pi^- \to D^{0*}\gamma\pi^-}$

We end with a brief discussion of the radiative decays $D_{0,2}^0 \to D_0^*\gamma$. Our framework should be more reliable for the decay chains $B^- \to D_{0,2}^0\pi^- \to D_0^*\gamma\pi^-$ because in this case the resonance is in the physical region and should dominate the amplitude. In this case the approximation in which the weak production of $D_{0,2}^0$ and the subsequent radiative decay

factorize should be more reliable.

The production rates $B^- \to D^0_{0,2}\pi^-$ were already obtained in Eq.4.76. The radiative decays of the $D^0_{0,2}$ can be readily extracted from the vertices in Ref. [16] (see Eqs. 13,14,15,A4 in that reference). We find

$$\Gamma(D_0^0 \to D^{0*}\gamma) = (e\mu_D^S)^2 \cdot \frac{E_\gamma^3}{m_{D_0^0}} \cdot \frac{E_{D^{*0}}}{4\pi} \approx 0.09 MeV,$$
$$\Gamma(D_2^0 \to D^{0*}\gamma) = (e\mu_D^T)^2 \cdot \frac{E_\gamma^3}{m_{D_2^0}} \cdot \frac{E_{D^{*0}}}{\pi} \approx 0.20 MeV. \tag{4.85}$$

Numerically, we used the results $\mu_D^S = \frac{2e_c\tau^{1/2}(1)}{m_c} + \frac{e_u}{\Lambda'_{1/2}} \approx 0.75 GeV^{-1}$ and $\mu_D^T = \frac{e_c\tau^{3/2}(1)}{m_c} + \frac{e_u}{\Lambda'_{3/2}} \approx 0.33 GeV^{-1}$ with input parameters discussed in Ref. [16].

Using $\Gamma_{D_0^0} = 276$ MeV and $\Gamma_{D_2^0} = 45$ MeV, we find $\mathcal{B}(D_0^0 \to D^{0*}\gamma) = 3.3 \times 10^{-4}$ and $\mathcal{B}(D_2^0 \to D^{0*}\gamma) = 4.5 \times 10^{-3}$. With sufficient statistics to observe these modes, it will then be possible to extract the coupling constants μ_D^S and μ_D^T. We present the result for D_2^0 for completeness, as it has already appeared in the literature [39].

4.2.6 Conclusions

We have analyzed the mode $B^- \to D_s^+ K^- \pi^-$ using HQET to parametrize "quasi-resonant" and non-resonant contributions. With the aid of angular analysis, it should be possible to extract the contributions of virtual intermediate states with spin 0, 1, or 2 leading to the $D_s^+ K^-$ final state.

The spin zero partial rate receives a large but not dominant contribution from the D_0^0 intermediate state. This means that it is not possible to test the $D_0^0 D_s^+ K^-$ vertex in a model independent way. However, we have seen that the HQET description gives a picture for this decay that can be tested qualitatively at least. The shape of the $M_{D_s^+ K^-}$ distribution for this partial rate depends both on the precise value of the D_0^0 mass, as well as on the relative size of the non-resonant contributions.

The spin one contribution can be almost as large as the spin zero contribution if $h' > 0$. This is quite surprising as this is dominated by an intermediate $D^{\star 0}$ with a mass significantly below threshold. This reinforces the conclusion that the decay is not dominated by the $D^{\star\star}$

resonances, although they play an important role. A determination of this contribution should provide strong evidence for the sign of h'.

The contribution of spin two is also very large and strongly dependent on the sign of h' indicating that it is not saturated by the "quasi-resonant" D_2^0 state. Contributions of spins higher than two are negligible.

Given the large $m_b - m_c$ mass difference, we do not expect the momentum expansion to describe this weak decay quantitatively. In particular, the pion and kaon in the non-resonant diagrams are not soft for most of the kinematically allowed range. However, we have provided a mixed framework that uses HQET to describe strong transitions and a naive factorization to describe weak transitions in terms of a few phenomenological parameters. This framework also provides a model for the non-resonant terms and produces a qualitative description for this decay mode that can be used to compare with experiment and to extract information on the signs and $SU(3)$ properties of the strong couplings.

CHAPTER 5. Search for gravitons in RS model

In our final application of the EFTs we will work beyond the SM. In the search for the new physics many models have been proposed trying to address theoretical problems present in the SM. Although every model predicts certain collider signatures these signatures may overlap with each other depending on the detailed workings and the parameter values within them. Thus, it is very important to search for the most unique signals in our quest for the next unifying theory. In this way, discovery of spin-2 gravitons at the LHC would be signal for the theory predicting TeV gravity scale. One of the most popular scenarios for the TeV scale gravity is the Randall-Sundrum model and in this chapter we will see how the RS gravitons may reveal themself at the LHC.

5.1 Introduction

As we discussed in Chapter 2, the original Randall-Sundrum [67] model with a warped extra dimension along with extensions provides the possibility for a simultaneous solution to Planck-weak hierarchy problem as well as the flavor puzzle in the Standard Model. The most distinctive feature of this scenario is the existence of Kaluza-Klein (KK) gravitons whose masses and couplings to the SM fields are set by the TeV scale. In realistic versions of this framework, the flavor structure of the SM is addressed through localization of fermions in the warped bulk compared to the models where all SM fieds were localized on the TeV brane. In this framework, the largest coupling of the gravitons to the observed particles is to the top quark and unphysical Higgses ($W_L^{\pm}$ and Z_L) with the KK graviton (G) masses predicted to be $\gtrsim$ 4 TeV. We now study the resonant production of the gravitons and their subsequent decay to $W_L W_L$ pair. We will find that, with 300 fb^{-1} integrated luminosity of data, the

semileptonic $G \to W(\to l\nu_l)W(\to 2jets)$ mode offers a good opportunity to search for the RS KK graviton mode with mass lighter than $\sim$ 3-3.5 TeV at the CERN LHC. Efficient WW mass reconstruction in the semileptonic mode combined with an analysis of dilepton mass distribution in the purely leptonic channel, $pp \to W(\to l\nu_l)W(\to l'\nu_{l'})$ may help to observe KK Z' and KK graviton separately. Suitably defined average energy of the charged lepton in the semileptonic mode may be used to distinguish decays from longitudinal versus transverse W-bosons.

The promising channels to observe RS gravitons are those where produced gravitons are decaying to fields localized near the TeV brane. Search for the KK gravitons using its decays to the top quarks was performed in [68]. The 4-lepton signal through the decay to a pair of Z_L's was studied in [69]. Reconstruction possibility of the Z's via their leptonic decays makes this a uniquely clean mode. Both analyses concluded that with $\sim$ 100-300fb^{-1} of data provided by LHC the gravitons of masses up to $\sim$2 TeV can be probed.

In this chapter we will study purely leptonic $G \to W_L W_L \to l\bar{\nu}_l l'\nu_{l'}$ and semileptonic modes, i.e. $(W \to l\nu)(W \to jets)$ from the decay of W_L pair [70]. Our analysis will suggests that we may be able to observe RS KK graviton mode with mass up to about $\sim$ 3-3.5 TeV as well as to separate its contribution from that of the RS KK Z'; thus, if they exist at all, providing strong evidence in favor of the RS framework [71]. Our strategy relies on the fact that in the class of models we are working $m_1^G \approx 1.5 m_1^{Z'}$ for the lightest KK masses of the graviton and the gauge fields [72]. Thus, since Z' has only 2/3 of the graviton mass and since cross-section falls quickly as we go up in mass of the resonance being produced, we may expect that the gauge KK modes would be more accessible [73, 74, 75]. Then, by making use of the above relationship between masses, we may look for the presence of the graviton in some other mode(s) where they could be well separated. In particular, we will show that using the purely leptonic mode to observe KK Z' (where graviton contribution will be hard to see due to its higher mass), we then may use the semileptonic mode with the knowledge of Z' mass to pin down the graviton contribution. However, the last channel is challenging as it requires to distinguish two collimated jets from highly boosted W boson from one QCD jet. Therefore, in

addition to WW irreducible SM background, we include W + 1 jet background in our study for this mode.

The reason for the enhancement of the graviton signal in the WW channel compared to the ZZ mode lies in the fact that the branching ratio (BR) to a W_L pair is twice as big as the BR to a Z_L pair. In addition to that, Br($W \to hadrons$) $\approx 2/3$ and Br($W \to l\nu$) $\approx 1/9$ compared to Br ($Z \to l^+l^-$) $\approx 3.3\%$, where l indicates each type of the lepton, not sum over them [76]. Also, it is worth mentioning that a RS graviton decays to top quark pairs about $\sim 70\%$ of the time compared to $\sim 15\%$ for a W_L pair. The important point for the $t\bar{t}$ final state, however, is that KK gluon couples to the top pair as well and surpasses graviton production [73, 74]. Also, the reconstruction of such energetic tops far away from the $t\bar{t}$ production threshold might be an additional challenge.

The main experimental problem in using the WW final state with subsequent leptonic decays is the presence of one or two neutrinos. In particular, we most probably will not be able to reconstruct WW mass in the leptonic case; although this channel will be a useful discovery channel to reveal the existence of KK gauge bosons. Then, we will show that the semileptonic mode should be able to see both signals as they will be well separated due to the significant mass differences mentioned before.

To summarize, our channels allow us to probe first RS KK graviton mode with mass below 3-3.5 TeV and, also, to distinguish it from the contributions of RS spin-1 KK gauge bosons. Certainly, the full establishment of the existence of spin-2 graviton from the RS model will need combined analysis of modes discussed later in this chapter with other decay modes considered before in the literature [68, 69]. The role of the Z_LZ_L mode is extremely important as this mode is forbidden for Z''s to decay into. Note, though, that the "gold-plated" nature of this special mode, with each Z decaying to e^+e^- and $\mu^+\mu^-$, comes at the price of needing a higher luminosity [71]. Thus, with the strategy discussed above and better statistics in (semi)leptonic modes of W's, we may optimistically have evidence for the RS gravitons.

5.2 Model

We closely follow the model discussed in [69] and briefly review it here. As discussed above, we allow SM fields to propagate in the extra dimension and distribute fermions along it to generate observed mass spectrum without introducing additional hierarchies. SM particles are identified with zero-modes of 5D fields, and the profile of the fermion in the extra dimension depends on its 5D mass. As was shown before [77, 78, 79], all fermion 5D masses are $O(1)$ parameters with the biggest one, among the SM quarks, being that of the top quark. To specify the model even further, the top quark is localized near the TeV brane; and the right-handed isospin is gauged [80]. We consider t_R being on the TeV brane (see discussion of the other possibilities in [69], for example). At the end of the day, we are left with three parameters to be measured experimentally. We define them as $c \equiv k/M_{Pl}$ the ratio of the Anti de Sitter (AdS) curvature k to the Planck mass; $\mu \equiv ke^{-\pi kR}$ which monitors gauge KK masses with the first few being (2.45, 5.57, 8.7...)$\times\mu$; and finally, parameter $\nu \equiv m/k$, which defines where the lightest fermion with bulk mass m is localized. For the t_R on the TeV brane, $\nu_{t_R} \approx 0.5$; and parameters c and μ will remain free in our analysis.

5.2.1 Low energy constraints on model parameters

As experimental measurements have placed restrictions on the RS model parameters values, different specific models have been proposed in the literature in order to soften them. The RS version with small KK masses, down to 1 TeV, which are consistent with all current experimental constraints on the fermion structure was constructed in [81]. An interesting variant of the warped extra dimension based on 5D minimal flavor violation was presented in [82]. The model allows to eliminate current RS flavor and CP problem with a KK scale as low as 2 TeV.

Now, we review constraints placed on the warped extra-dimension model with custodial isospin symmetry [80], which we adopt here. Implications of the observed BB mixings were discussed in [83]. In the model of [80], B-mixing is mainly accommodated by tree level exchange of KK gluons. In [83], the CP-violating effects on the B_d system were shown to provide

$M^{(1)}_{gluon}$ >3.7 TeV constraint with 1σ uncertainty. Phenomenological constraints from lepton-flavor-violations were discussed in [84]. After extensive analysis of $B \to K^* l^+ l'^-$ modes, only the $B \to K^* ee$ decay was found to have sizable new physics effects. With negligible SM contributions, current experimental bounds were translated into the lepton bulk mass parameters. For the first KK gauge boson mass of 2-4 TeV, 10-20% deviation from the SM results were found which can be probed in the near future. Other B-factory signals were studied in [85]. Finally, regions of parameter space that successfully reproduce the fit to electroweak precision observables with KK excitations as light as ~ 3 TeV were studied in [86].

While current theoretical constructions suggest that lightest KK gauge bosons have masses $\gtrsim 3$ TeV and therefore $m_G \gtrsim 4$ TeV, we believe that these models are still being developed; and therefore, for now, it is best to search for experimental signatures with the widest latitude. This point, in particular, was also emphasized in [87].

5.2.2 Couplings of KK gravitons

After these brief remarks we can write the couplings relevant to our discussions here. Since the graviton couples to the energy-momentum tensor, all couplings have generic form $C_{00n} h_{\mu\nu} T^{\mu\nu}$ ("00n" signifies that we are considering only coupling of the nth KK graviton to the SM fields which are zero-modes of the 5D fields). Magnitude of the coupling constants depend on the overlap of the particle wavefunctions in the extra-dimension (effects of the running gravitational coupling due to existence of non-Gaussian fixed point were analyzed in [88, 89]). We present coefficients C_{00n} in Table 5.1 along with partial decay widths for dominant decay channels for the lightest KK (n=1) graviton which will be the focus of our analysis; see also [69]. $W_L W_L, Z_L Z_L$ and hh decay channels illustrate equivalence theorem once again (which is valid up to $(M_{W,Z}/m_G)^2$ where m_G is the graviton mass).

The suppression in coupling of the graviton to the gluons follows because gauge boson has a flat wavefunction and thus its couplings to the graviton is suppressed by the volume of the bulk $\pi kR \approx 35$. For the same reason, decay of gravitons to transverse W and Z bosons as well as photons are suppressed by this volume factor. The masses of the KK gravitons are given

Table 5.1 Couplings of the nth level KK graviton to the SM fields. t_R assumed to be localized on the TeV brane. Parameter m_1^G is the mass of n=1 graviton and $x_1^G = 3.83$ is the first root of the first order Bessel function. $N_c = 3$ is number of QCD colors.

SM fields	C_{00n}	Partial decay widths for n=1 graviton
gg(gluons)	$\frac{c}{2\pi kR\mu}$	negligible
W_LW_L	$2c/\mu$	$(cx_1^G)^2 m_1^G/480\pi$
Z_LZ_L	$2c/\mu$	$(cx_1^G)^2 m_1^G/960\pi$
$t_R\bar{t}_R$	c/μ	$N_c(cx_1^G)^2 m_1^G/320\pi$
h h	$2c/\mu$	$(cx_1^G)^2 m_1^G/960\pi$

by $m_n = x_n\mu$ where x_n is n'th zero of the first order Bessel function. Notice that we do not need $q\bar{q}$G coupling as it is Yukawa-suppressed and graviton production is dominated by gluon fusion.

In this model the total width of the graviton is found to be $\Gamma_G = \frac{13(cx_1^G)^2 m_1^G}{960\pi}$ which is split between 4 dominant decay modes to $W_LW_L, Z_LZ_L, t_R\bar{t}_R$ and hh in the ratio 2:1:9:1. Taking $c \sim 1$, the total graviton width is $\sim 6\%$ of its mass and is very close to the corresponding width for RS KK Z′ in the same model [75].

5.3 Production and decay of KK gravitons

We are now in position to calculate the matrix element for the gg$\rightarrow G_n \rightarrow W_LW_L$. The details can be found elsewhere [90, 69]:

$$M(g^a g^b \rightarrow W_LW_L) = \frac{c^2}{\pi kR\mu^2} \cdot \frac{2A_{+-00}\delta_{ab}}{s - (m_n^G)^2 + i\Gamma_n^G m_n^G} \tag{5.1}$$

where, $A_{+-00} = A_{-+00} = \frac{1}{2}(\hat{\beta}^2 - 2)\hat{s}^2\sin^2\hat{\theta}$ is the only independent helicity amplitude for the decay to longitudinal W bosons. W boson velocity $\hat{\beta}^2 = 1 - 4M_W^2/\hat{s}$ and all hatted variables refer to the parton center of mass frame. We see that the amplitude has $\sin^2\hat{\theta}$ behavior characteristic of the W_L pair in the final state. This implies that our signal events will be concentrated in the central rapidity region, and we will exploit this fact later to separate our signal from SM background.

This amplitude gives the parton level cross-section [69]:

$$\frac{d\hat{\sigma}(gg \to W_L W_L)}{dcos\hat{\theta}} = \frac{|M|^2 \hat{\beta}}{512\pi\hat{s}}, \tag{5.2}$$

and the proton level cross-section is obtained by convolving the parton level cross-section with gluon PDF's:

$$\sigma(pp \to WW) = \int dx_1 dx_2 f_g(x_1, Q^2) f_g(x_2, Q^2) \hat{\sigma}(x_1 x_2 s). \tag{5.3}$$

Note that the total cross-sections for the EW boson final states are related by $\sigma(pp \to G \to W_L W_L) = 2 \times \sigma(pp \to G \to Z_L Z_L)$. Numerical results for our 2→2 process can be found in [69] (where the Z_L final state was used) which agrees with our current calculation.

5.4 Battling SM background

We now discuss the relevant decay modes of the W bosons.

If both W's decay hadronically, we face huge QCD background and, therefore, this mode is unlikely to be useful. Thus, in the rest of this chapter, we concentrate on pure leptonic and semileptonic decay modes of the W pair and consider the former first.

5.4.1 Pure leptonic mode: $e^{\pm}\mu^{\mp}$ final state

Due to the significant boost of the W's, neutrino's p_T in this mode will be almost back to back, and, therefore, missing energy information will be lost. We require the W's to decay to different lepton flavors since in SM there is no basic $2 \to 2$ partonic process giving two different high transverse momentum lepton flavors in the final state. After this, leading irreducible SM backgrounds for our $l^+ l'^- \not{E}_T$ final state are $W^+W^- \to l^+ l'^- \not{E}_T$ and $Z/\gamma^* \to \tau^+\tau^- \to l^+ l'^- \not{E}_T$ (where $l \neq l'$).

With two neutrino's in the final state, we might not reconstruct the resonant W boson mass. However, we will show that even looking only at the leptons (at this point by leptons we mean primarily e and μ; see, however, further discussion on τ's later) may provide enough

data to discover the RS graviton, given a suitable set of cuts. We will show that such cuts give S/B $\gtrsim 1$ for mass of the first KK graviton mode $m_1^G \lesssim 3$ TeV.

5.4.2 Semileptonic mode

For semileptonic channel we have highly collimated decay products for both W's. For the hadronic side, it implies that 2 jets from the W decay are likely to appear as one "fat" W-jet. This leads us to consider W + 1 jet which will be the leading background for this decay mode compared to irreducible SM WW production and W + 2 jets (which will be suppressed due to the 3 body phase-space). On the leptonic side, due to small angular separation between missing neutrino and charged lepton, we may estimate longitudinal (L) component of the $\nu's$ momentum as

$$p_\nu^L \approx \frac{\not{E}_T p_l^L}{p_{T_l}}, \tag{5.4}$$

which means that lepton's and neutrino's pseudorapidities are the same; and they are separated only in the transverse plane. Beyond this approximation, accuracy of the reconstructed leptonic W mass $M_W^2 = (p_l + p_\nu)^2$ will depend on the accuracy of the $\not{E}_T$ measurement which, in turn, depends on the ability to resolve substructure in the "fat" hadronic W-jet. Now, WW mass reconstruction $M_{WW}^2 = (p_{l\nu} + p_{jj})^2$ will depend on how effectively hadronic W side can be reconstructed. We will elaborate on this later.

5.5 Acceptance cuts and results

We now present our results as well as specify selection criteria for signal events. We estimated SM background with the aid of the COMPHEP package [23]. For our graviton signal, we used Mathematica program and partially cross-checked them with COMPHEP. For an additional check, we confirmed results of Ref.[69] for $\sigma(pp \to G \to Z_L Z_L)$, as was mentioned before. The CTEQ5M PDF's were used throughout (in their Mathematica distribution package [91] as well as intrinsically called by COMPHEP).

5.5.1 Pure leptonic mode: $e^{\pm}\mu^{\mp}$ final state

As a starting point, before imposing any cuts, we reproduced results of Ref.[92] which finds $\sigma(pp \to e^+\nu_e\mu^-\bar{\nu}_\mu) \approx 610$ fb and is dominated by WW production. We cross-checked our WW production results with Ref.[75] as well.

We impose basic acceptance cuts as

$$|\eta_l| < 3, \quad p_{T_l} > 50GeV, \quad \not{E}_T > 50GeV, \tag{5.5}$$

where η_l is the pseudorapidity of the charged lepton.

In Fig.5.1a,b we show the total cross-section for $pp \to l\nu_l l'\bar{\nu}_{l'}$ (where $l \neq l'$) and expected number of events per 300 fb^{-1} as a function of m_G for our signal. The corresponding SM background is ≈ 24 fb and is dominated by the WW production with contribution from $Z/\gamma^* \to \tau^+\tau^- \to l^+l'^-\not{E}_T$ process being about an order of magnitude smaller, which also is in good agreement with corresponding results of Ref.[75].

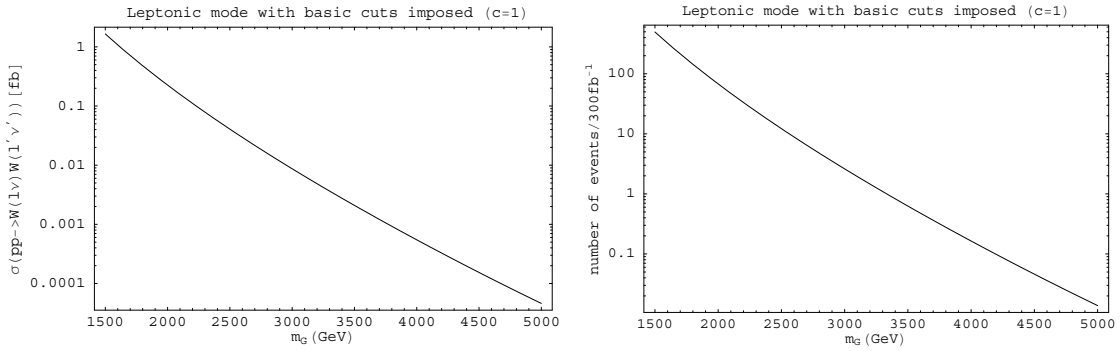

Figure 5.1 (a) Total signal cross-section for $pp \to l\nu l'\bar{\nu}_{l'}$, and (b) corresponding number of events for 300 fb^{-1}. Basic cuts from Eq.5.5 are applied and c=1. Corresponding SM background is ≈ 24 fb and is independent of the graviton mass.

We see that as the SM background dominates, we need to look for additional cuts to improve signal observability. Invariant dilepton mass may provide additional information to enhance our S/B ratio. In Fig.5.2 we show dilepton invariant mass distributions for signal and corresponding background where m_G =2 TeV and 3 TeV values were chosen.

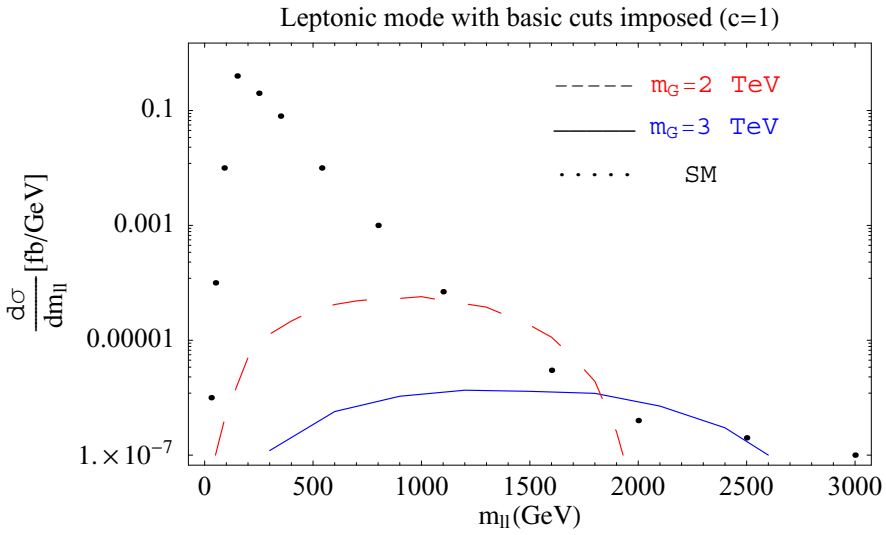

Figure 5.2 (Color online) Dilepton invariant mass distributions for graviton masses of 2 TeV (dashed red) and 3 TeV (solid blue). Dotted curve corresponds to the SM background.

We observe that the SM background distributions tend to peak at low dilepton invariant mass while signal events concentrate in the middle mass region dictated by the decay of the very massive object. This allows us to define cuts on dilepton mass. For the masses shown on Fig.5.2, for example, we have chosen them as

$$\begin{aligned} m_G = 2\ TeV: \quad & m_{ll'} > 1\ TeV \\ m_G = 3\ TeV: \quad & m_{ll'} > 1.5\ TeV \end{aligned} \tag{5.6}$$

to improve the statistical significance of the signal further. Table.5.2 shows the statistical results after all the cuts defined above were applied. We notice that the SM background was reduced significantly while the signal was roughly reduced by half. Throughout the chapter Poisson statistics CL to observe at least one signal event will be appropriate description if the number of background events < 10. When needed, these CL are given in brackets next to the corresponding statistical significances in Gaussian statistics.

In the model we are working, there will also be a contribution to the signal from the KK Z'. If we use the mass ratio of this model $m_1^G \approx 1.5 m_1^{Z'}$, we observe, for example, that a 3 TeV graviton should appear along with a 2 TeV Z′. Interestingly, we find that the total production

Table 5.2 Purely leptonic mode cross-sections [in fb] and S/B ratios after basic and dilepton mass cuts in Eq.5.5 and Eq.5.6 were imposed. Poisson statistics CL is appropriate description if the number of background events < 10.

2 TeV	Basic cuts	Dilepton mass cut	# of events/300 fb^{-1}	S/B	S/$\sqrt{B}$
Signal	0.22	0.1	30	2.5	8.7
Background	24	0.04	12		
3 TeV	Basic cuts	Dilepton mass cut	# of events/300 fb^{-1}	S/B	S/$\sqrt{B}$ (CL)
Signal	0.0087	0.004	1.2	0.6	0.8 (64%)
Background	24	0.007	2.1		

cross-section for 2 TeV graviton and Z' are very similar in magnitude (it is about 16 fb for Z' [75] compared to 10 fb for graviton) and shape. Thus, 2 TeV graviton contribution in Fig.5.2 may be numerically viewed as the one coming from Z$'$. After this observation, Fig.5.2 represents signal cross-section for 3 TeV graviton along with SM background and 2 TeV RS Z'. Similarly for 2 TeV graviton, 1.33 TeV Z' needs to be considered and so on. As two contributions are mixed up in this channel, it might be easier to "reserve" this channel for Z', since corresponding graviton contribution will be negligible. Stated differently, if enhancement in dilepton mass due to these states will be observed experimentally, most probably Z$'$ will have a dominant effect. Then, Fig.5.2 may be used to define a proper cut on dilepton mass variable to remove this Z' background (for example, for 3 TeV graviton $m_{ll} > 2$ TeV will work). Of course it might happen, that the lightest KK Z' and graviton masses are actually in different ratio and we need other measurement(s) to interpret enhancement in dilepton mass. In the next section we will show that semileptonic mode may provide this additional handle.

5.5.2 Semileptonic decay

As discussed above, leptonic W mass for this mode can be reconstructed; and W + 1 jet is a leading background. As in the case of the leptonic mode, we define basic selection cuts as

$$|\eta_{l,j}| < 1, \quad p_{T_l} > 50GeV, \quad \not{E}_T > 50GeV, \quad p_{T_j} > 100GeV, \tag{5.7}$$

and in Fig.5.3 we show the expected number of signal and background events, both integrated over one half of the graviton width. Assuming again that $m_G \approx 1.5 m_{Z'}$, the Z′ contribution is negligible in this WW invariant mass window because Z′ and graviton total widths are $\sim 5\%$ of their mass, while, the mass difference between Z′ and graviton is $\sim 50\%$ of Z′ mass; this also assumes that the Z' mass is established by the pure leptonic mode.

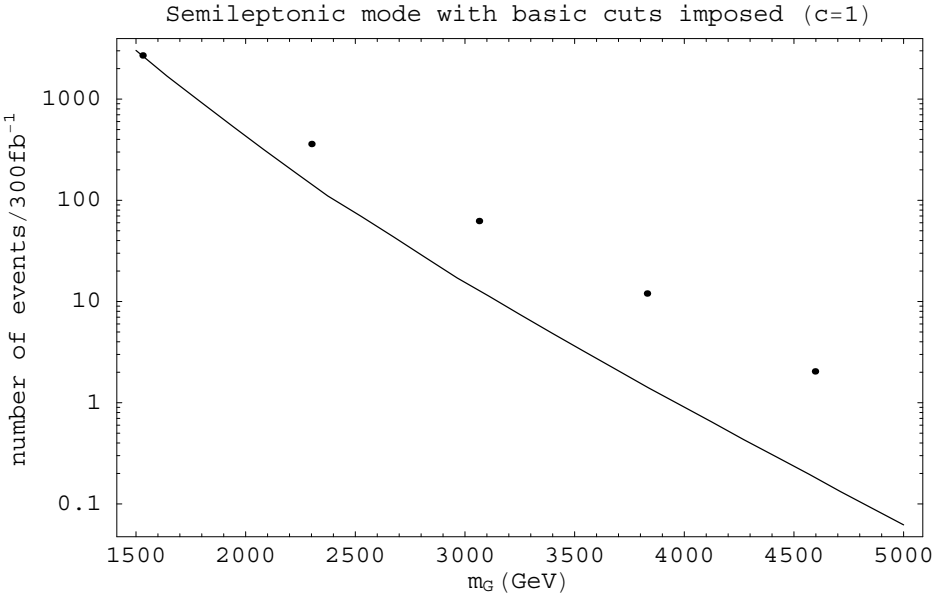

Figure 5.3 The total signal (solid) and SM background W + 1 jet (dotted) cross-section (integrated in $m_G \pm \Gamma_G/2$ window) after cuts specified in Eq.5.7 were applied.

We see that the background is severe; and, therefore, its reduction is a serious and challenging issue. One quantity that may help to resolve the problem is a jet-mass, which is the combined mass of the vector sum of 4-momenta of all hadrons making up the jet. For the signal, we expect jet-mass to peak at M_W. Along these lines, as it was shown in Ref.[75], the cut on the jet-mass $75 < M_{jet} < 125$ GeV gives a substantial rejection of the background events ($\approx 70\%$) while accepting most of the signal. Also, EM calorimeter, due to its finer segmentation, may allow to improve jet-mass resolution, since signal W events are expected to have two separated EM cores. For further discussion on this issue, we refer to Ref.[75, 93, 94, 95].

In an attempt to specify the selection cuts further, in Fig.5.4 (note that the scale is linear) we show the lepton energy distribution for graviton masses $m_G = 2$ TeV and m_G=3.5 TeV

for the same conditions as in Fig.5.3. We observe that by defining appropriate cuts on lepton energy signal observability can be improved. We define them as

$$\begin{aligned} m_G = 2\ TeV: &\qquad 0.2\ TeV < E_{lepton} < 1\ TeV \\ m_G = 3.5\ TeV: &\qquad 0.5\ TeV < E_{lepton} < 1.4\ TeV \end{aligned} \tag{5.8}$$

and show resulting statistics in Table.5.3. We observe that with 300fb^{-1}, it is possible to reach 1σ effect for 3.5 TeV graviton.

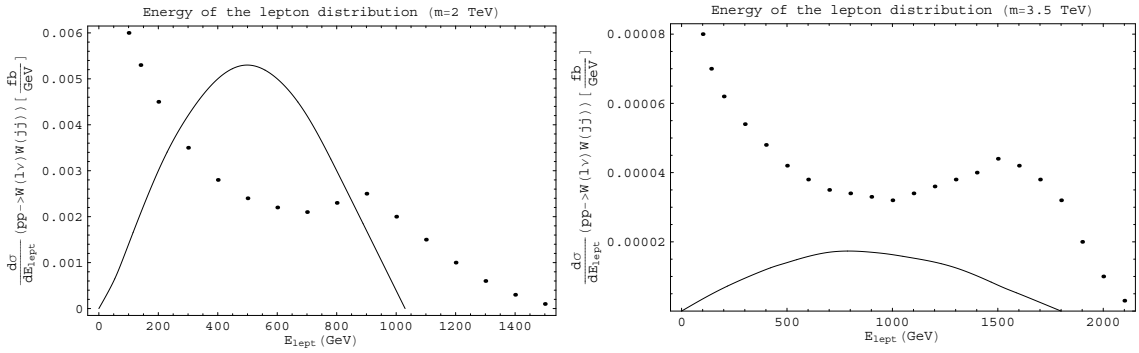

Figure 5.4 Differential lepton energy distribution for the signal (solid) and SM W + 1 jet background (dotted) (integrated in $m_G \pm \Gamma_G/2$ window) after cuts specified in Eq.5.7 were applied for (a) m_G=2 TeV and (b) m_G=3.5 TeV.

With efficient hadronic W mass reconstruction, we have another case when most of the hadronic QCD background can be separated; and we are left with WW as the only irreducible background. Fig.5.5 shows results for this situation with $c \equiv k/M_{Pl}$ =1 and 2 (see Ref.[69] for the discussion of the range of c). Notice that for Fig.5.5, we integrated over $(m_G \pm \Gamma_G)$ WW invariant mass window compared with $(m_G \pm \Gamma_G/2)$ window for Fig.5.3.

We see that in the c=1(2) case, the gravitons up to 3.5 TeV (4 TeV) mass might have enough events to be observed with good statistical significance; see Table 5.3. The dependence of the SM WW background on the c value follows from the fact that $m_G \pm \Gamma_G$ integration region is not constant since $\Gamma_G \sim c^2$.

In parallel with leptonic mode, we need to remember that we have a neutral gauge bosons

Table 5.3 Semileptonic mode signal cross-sections [in fb] and S/B ratios along with W + 1 jet and WW SM backgrounds. Signal 1 and the corresponding W + 1 jet background results were obtained after cuts in Eqs.5.7,5.8 were imposed and $m_G \pm \Gamma_G/2$ integration region was chosen. Signal 2 and corresponding WW background results were obtained after $|\eta_W|$ <1 cut and integrated in $m_G \pm \Gamma_G$ window.

2 TeV	Cuts	# of events/300 fb^{-1}	S/B	S/$\sqrt{B}$
Signal 1 [c=1]	1.7	510	1.04	23
W + 1 jet background [c=1]	1.64	492		
Signal 2 [c=1]	2.0	600	13.3	90
WW background [c=1]	0.15	45		
Signal 2 [c=2]	7.8	2340	7.8	135
WW background [c=2]	1.0	300		
3.5 TeV	Cuts	# of events/300 fb^{-1}	S/B	S/$\sqrt{B}$ (CL)
Signal 1 [c=1]	0.01	3	0.33	1 (54%)
W + 1 jet background [c=1]	0.03	9		
Signal 2 [c=1]	0.02	6	2.9	4.1 (99%)
WW background [c=1]	0.007	2.1		
Signal 2 [c=2]	0.07	21	1.4	5.4
WW background [c=2]	0.05	15		

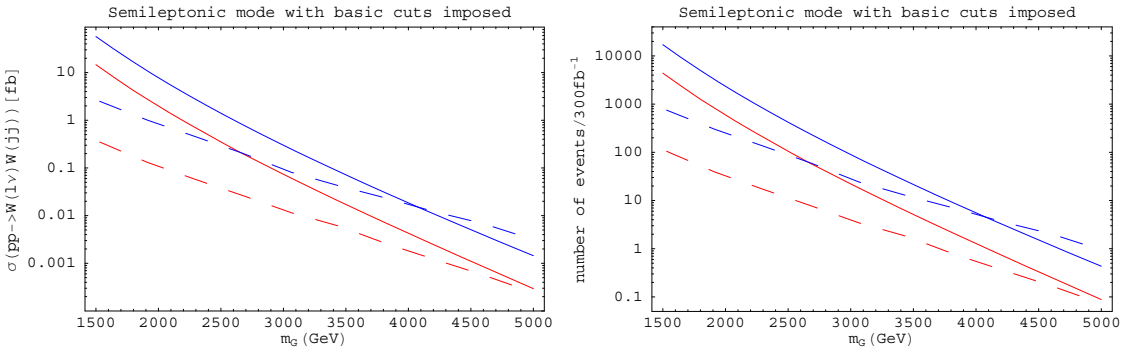

Figure 5.5 (Color online) (a) The total signal (solid) and SM background (dashed) cross-section (integrated in $m_G \pm \Gamma_G$ window) for $pp \to W(l\nu)W(jj)$ after $|\eta_W| < 1$ cuts were applied for c=1 (red) and c=2 (blue) values, (b) Corresponding number of events for 300 fb^{-1}.

Z′ produced (through $q\bar{q}$ annihilation or vector boson fusion processes) which might consequently decay to W_L pair [75]. Using $m_1^G \approx 1.5 m_1^{Z'}$ in Fig.5.6 we show that for 2 TeV Z' and corresponding $\sim$ 3 TeV graviton signals are well separated as a function of reconstructed WW invariant mass. Thus, by putting a $M_{WW} > 3$ TeV cut, the Z′ signal will become negligible and enhancement in total cross-section is due to graviton only (we obtain graviton cross-section to be 0.04 fb after $M_{WW} > 3$ TeV cut). Now, 2 TeV Z' can be discovered with 5σ statistical significance for an integrated luminosity of 100 fb^{-1} in purely leptonic channel as was shown in [75] and there the 3 TeV RS graviton contribution will be negligible. Thus, assuming that W + 1 jet background will be manageable (for example by means discussed above) and Z′ mass is estimated from some other mode (from purely leptonic one we considered above, for example) we may expect to confirm existence of RS graviton in semileptonic channel. Clearly, even if the above relation between masses of these lightest KK modes will not turn out to be true or some other resonance(s) will appear in this channel, WW mass spectrum measurement should still provide an important additional information.

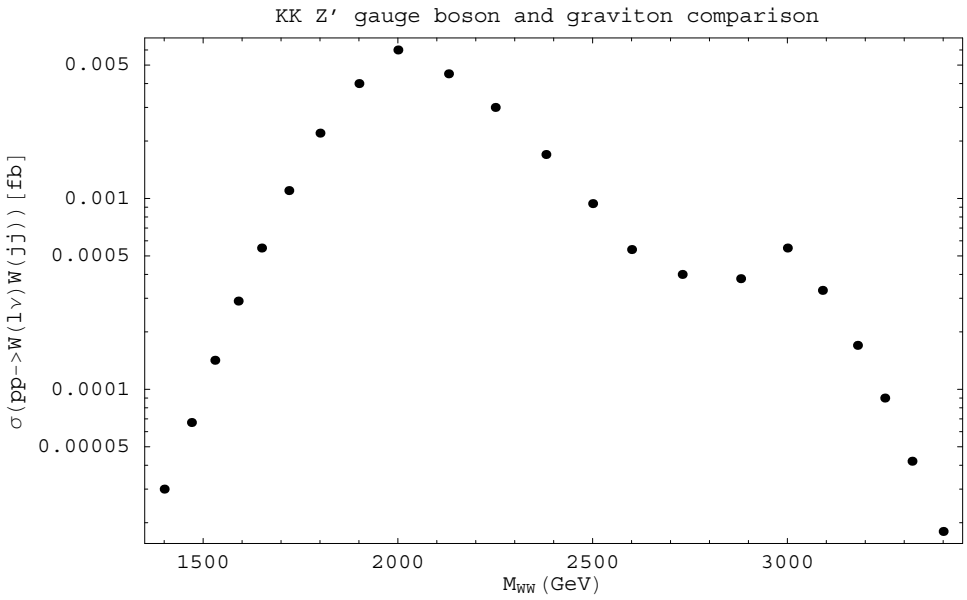

Figure 5.6 Contributions of the 2 TeV gauge boson and 3 TeV graviton to the $pp \to W(l\nu)W(jj)$ process. Cuts specified in Eq.5.7 were applied and c=1.

5.6 Discussion

We saw in previous sections that (semi) leptonic modes from W_L pair decay have a potential to discover RS graviton up to about (3.5 TeV) 3 TeV of mass. To increase statistics, we might expect to use τ leptons which will give us combinatorial factor of 3 and 3/2 for leptonic and semileptonic modes respectively from additional decay channels; therefore, the inclusion of the τ's can help appreciably. The reason for optimism on the issue of the detection of the τ's is that $\sim$500 GeV energy τ's have a decay length of $l = \gamma\tau c \approx 20$ mm and, thus, might leave visible tracks in the detector [96]. For $m_G \gtrsim 3.5$ TeV, higher luminosities are required which will scale our results accordingly [97]. Similarly, upgrades of the center of mass energy at LHC [98] can extend the reach in KK mass.

So far, the study of the RS gravitons was based either on the total cross-section or reconstructed graviton mass measurements. We might try to exploit unique spin-2 nature of the graviton which might be challenging in our channels. For example, one might be tempted to use lepton pseudorapidity which, due to the high boost of the decaying W's, will be $\sim\sin^2\theta$

behavior of the basic 2→2 underlying scattering process. But high-energy $W_L^+W_L^-$ production in the SM and RS Z′ decaying to two W_L also have this behavior and, thus, will be indistinguishable in shape from our signal.

Also, we might use information on lepton energy to establish that W's from our graviton decay are longitudinally polarized. This analysis is most promising in semileptonic mode because, as discussed in section IV B, in this mode WW mass can be reconstructed. Leptons from W_L decay will be preferentially emitted in the direction of the spin axis which is perpendicular to the direction of W motion. Thus, lepton and neutrino will tend to have the same energy in the lab frame, compared to decay of transversely polarized W's where they are emitted in the direction of the W motion and, thus, one of the W decay products will carry most of the energy. Now, suppose we have a negatively charged W decay. To confirm that W's from our graviton decay are longitudinally polarized we calculated the average lepton energy in the lab frame from the decay of polarized W bosons and summarized our results in Table 5.4. We notice that the average for the longitudinally and transversely polarized W's (which is the average of left-handed and right-handed polarizations) is the same and equal to $\sqrt{s}/4$. To distinguish between longitudinal and transverse polarizations, we divide signal events into two groups: events in the first group will have charged lepton energy bigger than the neutrino's energy; and in the second group, the neutrino's energy will be bigger. The fact that lepton's energy is bigger (smaller) implies that lepton's 3-momentum in the W rest frame is parallel (antiparallel) to W's 3-momentum in the lab frame. We calculated the average lepton energy in the lab frame from the decay of polarized W bosons for the events in each group and presented our results in Table 5.4 as well. We see that this analysis could be used to confirm that W's from our graviton decay are longitudinally polarized as, presumably, average lepton energies will match the $(8+3\beta)\sqrt{s}/32$ and $(8-3\beta)\sqrt{s}/32$ values for the signal events in the first and second group respectively. For a positively charged W decay, the results for the left-handed and right-handed rows in Table 5.4 need to be switched.

Table 5.4 Average lepton energies in the lab frame from the decay of polarized W^- bosons. For a W^+ decay, the results for the left-handed and right-handed rows need to be switched.

W polarization	Average	Average for group 1	Average for group 2
Longitudinal	$\sqrt{s}/4$	$(8+3\beta)\sqrt{s}/32$	$(8-3\beta)\sqrt{s}/32$
Left-handed	$(2+\beta)\sqrt{s}/8$	$(28+17\beta)\sqrt{s}/112$	$(28-17\beta)\sqrt{s}/112$
Right-handed	$(2-\beta)\sqrt{s}/8$	$(28+17\beta)\sqrt{s}/112$	$(28-17\beta)\sqrt{s}/112$

5.7 Conclusion

In this chapter, we have considered resonant production of the first RS KK graviton mode via gluon-fusion process followed by its subsequent decay to W_LW_L pair. We focused on leptonic and semileptonic final states and found that with $300 fb^{-1}$ of data, LHC may discover first RS KK graviton with masses below ~ 3 TeV and 3.5 TeV in these modes respectively. We also incorporated potential KK Z' signal in both modes and analyzed its combined effect with RS graviton. Taking the RS prediction for the lightest KK masses, $m_1^G \approx 1.5 m_1^{Z'}$, we showed that these signals are well separated in reconstructed WW invariant mass in the semileptonic mode. For the purely leptonic $e\mu$ mode, where resonance mass reconstruction is problematic, the above mass relationship hints to the domination of the Z' events as corresponding graviton mass will be higher. Nevertheless, we demonstrated that even in that mode appropriate choice of cuts in dilepton invariant mass may be able to distinguish these contributions as well. Finally, it is worth mentioning that the discovery of first RS graviton mode will shed the light on the scale of the physical processes on the TeV brane Λ_π as $m_1^G = x_1 c\Lambda_\pi$.

BIBLIOGRAPHY

[1] O. Antipin, J. Tandean and G. Valencia, Phys. Rev. D **76**, 094024 (2007) [arXiv:0705.3279 [hep-ph]].

[2] D.N. Goswami and J. Schechter, Phys. Rev. D **1**, 290 (1970) [Erratum-ibid. D **4**, 3526 (1971)].

[3] J. Finjord and M.K. Gaillard, Phys. Rev. D **22**, 778 (1980).

[4] W.M. Yao *et al.* [Particle Data Group], J. Phys. G **33**, 1 (2006).

[5] M. Bourquin *et al.*, Nucl. Phys. B **241**, 1 (1984).

[6] N. Solomey, Nucl. Phys. Proc. Suppl. **115**, 54 (2003) [arXiv:hep-ex/0208026]; O. Kamaev [HyperCP Collaboration], AIP Conf. Proc. **842**, 452 (2006); Talk given at the Joint Meeting of Pacific Region Particle Physics Communities, 29 October – 3 November 2006, Honolulu, Hawaii; O. Kamaev, FERMILAB-THESIS-2007-40.

[7] J. Gasser and H. Leutwyler, Annals Phys. **158**, 142 (1984).

[8] J. Bijnens, H. Sonoda, and M.B. Wise, Nucl. Phys. B **261**, 185 (1985).

[9] E. Jenkins and A.V. Manohar, Phys. Lett. B **255**, 558 (1991); *ibid.* **259**, 353 (1991); E. Jenkins, Nucl. Phys. **B368**, 190 (1992); in *Effective Field Theories of the Standard Model*, edited by U.-G. Meissner (World Scientific, Singapore, 1992).

[10] E. Jenkins, Nucl. Phys. B **375**, 561 (1992).

[11] J. A. Cronin, Phys. Rev. **161**, 1483 (1967).

[12] R.S. Chivukula and A.V. Manohar, Phys. Lett. B **207**, 86 (1988) [Erratum-ibid. B **217**, 568 (1989)]; J.F. Gunion, H.E. Haber, G.L. Kane, and S. Dawson, *The Higgs Hunter's Guide* (The Perseus Books Group, New York, 2000).

[13] M.N. Butler, M.J. Savage, and R.P. Springer, Nucl. Phys. B **399**, 69 (1993) [arXiv:hep-ph/9211247].

[14] D.A. Egolf, I.V. Melnikov, and R.P. Springer, Phys. Lett. B **451**, 267 (1999) [arXiv:hep-ph/9809228]; R.P. Springer, *ibid.* **461**, 167 (1999); A. Abd El-Hady and J. Tandean, Phys. Rev. D **61**, 114014 (2000) [arXiv:hep-ph/9908498].

[15] O. Antipin and G. Valencia, Phys. Lett. B **647**, 164 (2007) [arXiv:hep-ph/0611085].

[16] O. Antipin and G. Valencia, Phys. Rev. D **74**, 054015 (2006) [arXiv:hep-ph/0606065].

[17] E. Barberio *et al.* [The Heavy Flavor Averaging Group], arXiv:hep-ex/0603003.

[18] J. (. Hewett *et al.*, arXiv:hep-ph/0503261.

[19] L. Reina, G. Ricciardi and A. Soni, Phys. Rev. D **56**, 5805 (1997) [arXiv:hep-ph/9706253].

[20] L. Reina, G. Ricciardi and A. Soni, Phys. Lett. B **396**, 231 (1997) [arXiv:hep-ph/9612387].

[21] B. Grinstein and R. F. Lebed, Phys. Rev. D **60**, 031302 (1999) [arXiv:hep-ph/9902369].

[22] H. Y. Cheng, C. Y. Cheung, G. L. Lin, Y. C. Lin, T. M. Yan and H. L. Yu, Phys. Rev. D **51**, 1199 (1995) [arXiv:hep-ph/9407303].

[23] A. Pukhov *et al.*, arXiv:hep-ph/9908288, E. Boos *et al.* [CompHEP Collaboration], Nucl. Instrum. Meth. A **534**, 250 (2004) [arXiv:hep-ph/0403113].

[24] P. Koppenburg *et al.* [Belle Collaboration], Phys. Rev. Lett. **93**, 061803 (2004) [arXiv:hep-ex/0403004].

[25] S. Eidelman *et al.* [Particle Data Group], Phys. Lett. B **592**, 1 (2004).

[26] T. Okabe *et al.*, Phys. Lett. B **614**, 27 (2005) [arXiv:hep-ex/0411066].

[27] M. B. Wise, Phys. Rev. D **45**, 2188 (1992).

[28] G. Burdman and J. F. Donoghue, Phys. Lett. B **280**, 287 (1992).

[29] Aneesh V. Manohar and Mark B. Wise, "Heavy quark physics" (2000). Cambridge Monographs on Particle Physics, Nuclear Physics, and Cosmology.

[30] P. L. Cho and H. Georgi, Phys. Lett. B **296**, 408 (1992) [Erratum-ibid. B **300**, 410 (1993)] [arXiv:hep-ph/9209239].

[31] J. F. Amundson *et al.*, Phys. Lett. B **296**, 415 (1992) [arXiv:hep-ph/9209241].

[32] R. Casalbuoni, A. Deandrea, N. Di Bartolomeo, R. Gatto, F. Feruglio and G. Nardulli, Phys. Rept. **281**, 145 (1997) [arXiv:hep-ph/9605342].

[33] N. Isgur and M. B. Wise, Phys. Lett. B **237**, 527 (1990).

[34] N. Isgur and M. B. Wise, Phys. Lett. B **232**, 113 (1989).

[35] P. Colangelo, F. De Fazio and G. Nardulli, Phys. Lett. B **316**, 555 (1993) [arXiv:hep-ph/9307330].

[36] P. Colangelo, F. De Fazio and G. Nardulli, Phys. Lett. B **334**, 175 (1994) [arXiv:hep-ph/9406320].

[37] A. F. Falk, Nucl. Phys. B **378**, 79 (1992).

[38] U. Kilian, J. G. Korner and D. Pirjol, Phys. Lett. B **288**, 360 (1992).

[39] J. G. Korner, D. Pirjol and K. Schilcher, Phys. Rev. D **47**, 3955 (1993) [arXiv:hep-ph/9212220].

[40] N. Isgur and M. B. Wise, Phys. Rev. D **43**, 819 (1991).

[41] P. Colangelo, F. De Fazio and G. Nardulli, Phys. Lett. B **372**, 331 (1996) [arXiv:hep-ph/9506332].

[42] P. Colangelo, G. Nardulli and N. Paver, Phys. Lett. B **293**, 207 (1992).

[43] B. Grinstein, E. Jenkins, A. V. Manohar, M. J. Savage and M. B. Wise, Nucl. Phys. B **380**, 369 (1992) [arXiv:hep-ph/9204207].

[44] J. Charles *et al.* [CKMfitter Group], Eur. Phys. J. C **41**, 1 (2005) [arXiv:hep-ph/0406184]. Updated results used in this paper are from http://ckmfitter.in2p3.fr/ "Results as of FPCP 2006, Vancouver, Canada.

[45] J. N. Simone *et al.* [The Fermilab Lattice, MILC and HPQCD Collaborations], Nucl. Phys. Proc. Suppl. **140**, 443 (2005) [arXiv:hep-lat/0410030].

[46] M. Artuso *et al.* [CLEO Collaboration], Phys. Rev. Lett. **95**, 251801 (2005) [arXiv:hep-ex/0508057].

[47] R. Casalbuoni, A. Deandrea, N. Di Bartolomeo, R. Gatto, F. Feruglio and G. Nardulli, Phys. Lett. B **299**, 139 (1993) [arXiv:hep-ph/9211248].

[48] H. Y. Cheng, C. Y. Cheung, G. L. Lin, Y. C. Lin, T. M. Yan and H. L. Yu, Phys. Rev. D **47**, 1030 (1993) [arXiv:hep-ph/9209262].

[49] B. Aubert *et al.* [BABAR Collaboration], Phys. Rev. D **72**, 051106 (2005) [arXiv:hep-ex/0506070].

[50] J. A. Macdonald Sorensen and J. O. Eeg, arXiv:hep-ph/0605078.

[51] Y. Li, C. D. Lu and C. F. Qiao, Phys. Rev. D **73**, 094006 (2006) [arXiv:hep-ph/0512347].

[52] G. Eilam, M. Ladisa and Y. D. Yang, Phys. Rev. D **65**, 037504 (2002) [arXiv:hep-ph/0107043].

[53] G. Ecker, A. Pich and E. de Rafael, Nucl. Phys. B **303**, 665 (1988).

[54] G. Hiller and A. S. Safir, JHEP **0502**, 011 (2005) [arXiv:hep-ph/0411344].

[55] In the context of effective Lagrangians this can be found, for example, in H. W. Fearing and S. Scherer, Phys. Rev. D **53**, 315 (1996) [arXiv:hep-ph/9408346].

[56] "Study of B decays to open charm final state with the BaBar experiment" by Giovanni Calderini from the BaBar Collaboration, ICHEP 06,Moscow. http://ichep06.jinr.ru/session.asp?sid=8; B. Aubert *et al.* [BABAR Collaboration], arXiv:0707.1043 [hep-ex].

[57] K. Abe *et al.* [Belle Collaboration], Phys. Rev. D **69**, 112002 (2004) [arXiv:hep-ex/0307021].

[58] T. M. Yan, H. Y. Cheng, C. Y. Cheung, G. L. Lin, Y. C. Lin and H. L. Yu, Phys. Rev. D **46**, 1148 (1992) [Erratum-ibid. D **55**, 5851 (1997)].

[59] A. F. Falk and M. E. Luke, Phys. Lett. B **292**, 119 (1992) [arXiv:hep-ph/9206241].

[60] F. Jugeau, A. Le Yaouanc, L. Oliver and J. C. Raynal, Phys. Rev. D **72**, 094010 (2005) [arXiv:hep-ph/0504206].

[61] H. Georgi, "Weak Interactions and Modern Particle Theory," Benjamin/Cummings Pub. Co., Menlo Park, Calif. 1984.

[62] S. Veseli and I. Dunietz, Phys. Rev. D **54**, 6803 (1996) [arXiv:hep-ph/9607293].

[63] M. Neubert, Phys. Lett. B **418**, 173 (1998) [arXiv:hep-ph/9709327].

[64] A. Le Yaouanc, L. Oliver, O. Pene and J. C. Raynal, Phys. Lett. B **387**, 582 (1996) [arXiv:hep-ph/9607300].

[65] H. Y. Cheng, C. K. Chua and C. W. Hwang, Phys. Rev. D **69**, 074025 (2004) [arXiv:hep-ph/0310359].

[66] H. Y. Cheng and C. K. Chua, Phys. Rev. D **74**, 034020 (2006) [arXiv:hep-ph/0605073].

[67] L. Randall and R. Sundrum, Phys. Rev. Lett. **83**, 3370 (1999) [arXiv:hep-ph/9905221].

[68] A. L. Fitzpatrick, J. Kaplan, L. Randall and L. T. Wang, arXiv:hep-ph/0701150.

[69] K. Agashe, H. Davoudiasl, G. Perez and A. Soni, Phys. Rev. D **76**, 036006 (2007) [arXiv:hep-ph/0701186].

[70] O. Antipin, D. Atwood and A. Soni, arXiv:0711.3175 [hep-ph].

[71] We emphasize here that while Ref. [69] concentrated on the purely leptonic modes of the Z's, they did note the importance of the semi-leptonic mode but left it for future study. Addition of the semi-leptonic mode with one of the Z→jets would of course also appreciably enhance the reach of the ZZ mode over the ≈ 2 TeV that Ref. [69] explicitly stated with the pure leptonic decay channels.

[72] H. Davoudiasl, J. L. Hewett and T. G. Rizzo, Phys. Rev. D **63**, 075004 (2001) [arXiv:hep-ph/0006041].

[73] K. Agashe, A. Belyaev, T. Krupovnickas, G. Perez and J. Virzi, arXiv:hep-ph/0612015.

[74] B. Lillie, L. Randall and L. T. Wang, JHEP **0709**, 074 (2007) [arXiv:hep-ph/0701166].

[75] K. Agashe *et al.*, arXiv:0709.0007 [hep-ph].

[76] In all the numerical estimates presented in this paper, we will only include $W \to e\nu_e$ and $W \to \mu\nu_\mu$. However, towards the end in Section VI we will emphasize that the detection of the τ's from these decays may indeed be feasible.

[77] Y. Grossman and M. Neubert, Phys. Lett. B **474**, 361 (2000) [arXiv:hep-ph/9912408].

[78] S. J. Huber and Q. Shafi, Phys. Lett. B **498**, 256 (2001) [arXiv:hep-ph/0010195].

[79] T. Gherghetta and A. Pomarol, Nucl. Phys. B **586**, 141 (2000) [arXiv:hep-ph/0003129].

[80] K. Agashe, A. Delgado, M. J. May and R. Sundrum, JHEP **0308**, 050 (2003) [arXiv:hep-ph/0308036].

[81]

[81] G. Moreau and J. I. Silva-Marcos, JHEP **0603**, 090 (2006) [arXiv:hep-ph/0602155].

[82] A. L. Fitzpatrick, G. Perez and L. Randall, arXiv:0710.1869 [hep-ph].

[83] S. Chang, C. S. Kim and J. Song, JHEP **0702**, 087 (2007) [arXiv:hep-ph/0607313].

[84] S. Chang, C. S. Kim and J. Song, arXiv:0712.0207 [hep-ph].

[85] K. Agashe, G. Perez and A. Soni, Phys. Rev. Lett. **93**, 201804 (2004) [arXiv:hep-ph/0406101].

[86] M. S. Carena, E. Ponton, J. Santiago and C. E. M. Wagner, Nucl. Phys. B **759**, 202 (2006) [arXiv:hep-ph/0607106].

[87] See R. Sundrum talk at the "Brookhaven Forum 2007: New Horizons at Colliders", May 2007.

[88] J. Hewett and T. Rizzo, arXiv:0707.3182 [hep-ph].

[89] D. F. Litim and T. Plehn, arXiv:0707.3983 [hep-ph].

[90] S. C. Park, H. S. Song and J. H. Song, Phys. Rev. D **65**, 075008 (2002) [arXiv:hep-ph/0103308].

[91] J. Pumplin, D. R. Stump, J. Huston, H. L. Lai, P. Nadolsky and W. K. Tung, JHEP **0207**, 012 (2002) [arXiv:hep-ph/0201195].

[92] E. Accomando, arXiv:0709.1364 [hep-ph].

[93] J. Colas *et al.* [ATLAS Liquid Argon Calorimeter Collaboration], Nucl. Instrum. Meth. A **550**, 96 (2005) [arXiv:physics/0505127].

[94] D. Benchekroun, C. Driouichi and A. Hoummada, Eur. Phys. J. direct C **3**, N3 (2001).

[95] W. Skiba and D. Tucker-Smith, Phys. Rev. D **75**, 115010 (2007) [arXiv:hep-ph/0701247].

[96] See also H. U. Bengtsson, W. S. Hou, A. Soni and D. H. Stork, Phys. Rev. Lett. **55**, 2762 (1985).

[97] H. Davoudiasl, T. G. Rizzo and A. Soni, arXiv:0710.2078 [hep-ph].

[98] O. Bruning *et al.*, CERN-LHC-PROJECT-REPORT-626.